UNIVERSITÀ DEGLI STUDI DI CATANIA
FACOLTÀ DI SCIENZE MM. FF. NN.
DIPARTIMENTO DI SCIENZE CHIMICHE

Dottorato Internazionale di Ricerca in Scienze Chimiche
XXIV Ciclo

Titanium Dioxide Nanoparticles in the Field of Conservation of Cultural Heritage

---

Coordinatore: Prof. Corrado Tringali

Tutor: Prof. Enrico Ciliberto

Dottorando: Dr. Pietro Gemmellaro

A.A. 2008-2011

Ph.D. Thesis

Dedicated to my beloved mother

Table of Contents

Acknowledgements

I would like to express my sincere gratitude and appreciation to my research supervisor, Prof. Enrico Ciliberto, for guidance, support and patience towards the completion of this work, with a lot of passion, and also for our many scientific and not scientific discussions.

My sincere appreciations also extend to Prof. Geoffrey Allen, Interface Analysis Centre (University of Bristol, UK), and his Ph.D. student, James MacFarlane, who have provided assistance especially for gas photocatalytic experiments.

Grateful acknowledgements are to polish group of Prof. Danuta Kaczmarek (Politechnika Wrocławska, Wrocław): Dr. Jaroslaw Domaradzki, PhD students Michał Mazur, Damian Wojcieszak and Karolina Sieradzka for their collaboration, advice and valuable suggestions particularly in the method of conducting a research. I also wish to thank Mr. Eugeniusz Prociów, group technician who have provided assistance at instruments technology. I have to say thanks to this great foreign experience, without which I wouldn't know very special people, such as Marco Messina, Claudio Siracusano, Gabriele La Rosa, Luca Matarese and many others. This was probably one of the most beautiful periods of my life, and not only for pints (małe piwo) or discotheques for which I'll always have a special place in my thoughts and heart.

Special thanks to Dr. Ezio Viscuso for the help with SEM images and the EDX sample characterizations. Many thanks to all

the people who helped me to handle experiments and gave me access to their equipment as well as support and discussion of obtained results: Prof. Graziella Malandrino and Dr. Rita Catalano for XRD measurements, Prof. Salvatore Giuffrida for DLS techniques, Dr. Alessandro Motta for XPS equipments, and Prof. Raffaele Bonomo for UV-Vis spectrophotometry.

A sincere thanks also goes to the Erasmus student Magdalena Zalesakova, who helped me in reading and correcting this Ph.D. thesis as well as Dr. Cosimo Fortuna. I would like to thanks to Giuseppe Trusso for his great help for the graphic layout in this thesis.

Thanks to Ph.D. coordinator Prof. Corrado Tringali and Ph.D. officer Sabrina Tosto, for the very nice working atmosphere and great help in the bureaucracy, as well as all my Ph.D. colleagues.

Lastly, I would like to acknowledge my family and Cinzia Catanzaro for their love, understanding and support throughout my work.

And last but certainly not least finally I would like to extend endless thanks to my friends and family for helping me get through the past three years. I am also grateful to all people helping me during the PhD period and which are not mentioned by name.

An acknowledgement in my thesis is just a small gesture and doesn’t truly represent how much I appreciate the influence that many people have had on my life.

Keywords

TiO_2, doped, titania, titanium dioxide, metal oxide, nanostructure, nanoparticles, sol-gel, spin coating, anatase, photocatalysis, catalytic oxidation, surface, OH groups.

List of Abbreviations

•OH	Hydroxyl radical
1D	One dimensional model
2D	Two dimensional model
3D	Three dimensional model
AOPs	Advanced oxidation processes
CB	Conduction band
CVD	Chemical vapour deposition
DLS	Dynamic light scattering
DSC	Differential scanning calorimetry
EDS	Energy dispersive X-Ray spectroscopy
EDX	Energy dispersive X–ray
JCPDS	Joint Committee on Powder Diffraction Standards
PVD	Physical vapour deposition
SC	Semiconductor
SEM	Scanning electron microscopy
TG	Thermogravimetric analysis
TGA	thermal gravimetric analysis
UV	ultraviolet spectra
UV-Vis	Ultraviolet-visible spectra
VB	valence band
VOCs	Volatile organic compounds
XPS	X-ray photoelectron spectroscopy
XRD	X-ray diffraction

Conservation Problems and Nanotechnology Solutions

The artwork of modern civilisation has had a powerful impact on society from a political, sociological, and anthropological point of view, so the conservation of Cultural Heritage is essential for imparting culture, traditions, and ways of thinking and behaving to future generations.

Over the last few decades, the United Nations has developed an extensive system of international documentation to oblige member countries to comprehensively protect global cultural heritage against pollution and devastation. The 1972 UNESCO World Heritage Convention imposed all countries to safeguard national cultural heritage. However, conservation can have different meanings in different fields. For example, art conservation versus book and manuscript conservation, versus managing the physical environment (ecology), and so on. Every intervention of restoration and safeguarding of works of art is commonly considered a conservation treatment. Conservation can involve the cleaning procedures set up by chemists, or the photo documentation for the preservation of historical heritage. For the appropriate conservation of works of art, even the lighting systems in a museum or checking visitor numbers at a site should be monitored.

During the last decades, the scientific contribution to conservation work related to cultural heritage has grown rapidly. On the other hand, the expertise in conserving a work of art is not limited to historical and artistic analysis. Nowadays, conservation

requires a deep knowledge of materials science given that all natural aging of works of art cannot be prevented.

Thus, chemists and physicists contribute greatly to the 'controlled death' of works of art because they can provide useful and reliable predictions of their degradation. Recently, scientists started using nanotechnologies in the field of cultural heritage. Nanotechnology is an exciting modern research field encompassing traditionally specialist disciplines such as chemistry, physics, engineering and medicine. Many areas of applications like optics and catalysis will continue to benefit from recent improvements in the control of materials morphology at the nano-scale.

Nanoparticles are less than 100 nm [1] across which means they possess different properties to their corresponding bulk material [2]. Their miniscule size is responsible for their large surface area, and this in turn produces a considerably increased surface to volume ratio affecting their physico-chemical properties [3]. In particular, they have distinctive optical, electronic, electrical, magnetic, chemical and mechanical properties [4].

Nanoscience and nanotechnology are revolutionizing materials science in a pervasive way, in a manner similar to polymer chemistry's revolution of materials science over the past century. The continuous development of novel nanoparticle-based materials and the study of physicochemical phenomena at the nanoscale are creating new approaches to conservation science, leading to new methodologies that can 'revert' the degradation processes of works of art, in most cases 'restoring' them to their original magnificent appearance. Until recently, serendipity and empirical attempts have

been the most frequent design principles of the formulations for cleaning and consolidating works of art.

Consequently, there have been a number of actively detrimental treatments, such as the application of acrylic and vinyl resins to wall paintings, which can irreversibly jeopardize the appearance (or even the continued existence) of irreplaceable works of art. Conservation Science is still in its infancy.

Chemical degradation, which induces flaking in paintings and deterioration due to rain, wind, dust, and other environmental effects, is mainly responsible for weakening the porous structure and surface layers of the materials used in works of cultural heritage. In these situations, restoring these works of art is essential. Most interventions reinforce the porous structure and consolidate the surface layer. After cleaning and consolidation, protective treatments, extend the life of the works of art. Restoration combats surface bloom by minimizing the light scattering effects, and surface protection strongly reduces degradation from pollutants and water condensation. Having mentioned these benefits, on the other hand, every restoration treatment must be considered as invasive and in certain cases disruptive.

A few simple principles for obtaining the best restoration results should be followed:

• the treatment should be reversible so that one can go back to the original status of the work of art at any time;

• all the applied chemicals must ensure maximum durability and chemical inertness;

• the applied chemicals must invert the degradation processes without altering the chemical composition of the works of art and their physico-chemical and mechanical properties.

It should be noted that each conservation treatment of an artefact needs to be individually assessed [5]. The choice of conservation treatment depends greatly on the materials used in the piece of art and the period it was produced in.

Cultural and heritage works of art can be restored with the latest nanoparticle technology after degradation over time as well as damage due to unnatural causes, such as floods and fires. The use of nanotechnology in art conservation is a relatively new concept. It wasn't until 2001 [6] that the first use of nanomaterials in this field was published.

This initial report received significant praise for applying nanotechnology to a practical purpose (as distinct from a future application) which immensely improved on the current technologies. Since then nanotechnology has been applied to a variety of different cultural heritage conservation projects [7-14].

The main purpose of this thesis is to investigate how nanoparticles and nanotechnology have impacted cultural restoration, and more specifically how they have partially halted degradation processes, despite not being able to halt them completely.

Increases in volatile organic compounds (VOCs) and other pollutants such as NO_x and SO_2 in the air and water has become a very serious problem causing different kinds of degradation (as well as being hazardous to public health). To date, air pollutants in

particular have traditionally been removed by absorption, transferring them from the gaseous to solid or liquid phases, but this ultimately causes disposal problems.

Titanium dioxide (TiO_2) in anatase form possesses desirable properties for application as photocatalyst. Among these properties are excellent photochemical stability, low-cost, and non-toxicity. In tandem with ultraviolet (UV) light, TiO_2 has proven to be highly effective in converting organic pollutants, both in aqueous and gaseous media, into mineral acids, carbon dioxide, and water [15-18]. With visible light, however, TiO_2 has very poor photocatalytic activity due to its high-band gap energy which can only be activated by UV radiation to generate electron-hole pairs (e^-/h^+) of high redox potentials. Therefore, the first step in this research into innovative processes will be to develop modified TiO_2 materials by transition metal co-doping which can be used as photocatalysts and be activated by visible light as well as UV.

The second step will involve investigating methods of applying the new oxide materials as stable coatings on suitable substrates for their potential use in the destruction of atmospheric pathogens and other pollutants, and the removal of contaminants from those environments where works of art are exposed such as museums, churches, galleries, etc.

The work presented in this thesis focuses on applying a bottom-up approach through the sol-gel technique to produce thin inorganic layers containing undoped and doped TiO_2 nanoparticles capable of destroying the air and water pollutants normally present in the environments described above.

References

[1] X. Feng, "Encyclopaedia of Nanoscience and Nanotechnology"; H. S. Nalwa, ed., American Scientific Publishers: California, 2004; pp. 687-726.

[2] G. Schmid, ed. "Nanoparticles", Wiley-VCH Verlag, Germany, 2004.

[3] P. Baglioni, R. Giorgi, Soft Matter, 2006, 2, pp. 293-303.

[4] S. Utamapanya, K.J. Klabunde, J.R. Schlup, Chem. Mat., 1991, 3, pp. 175-181.

[5] L. Dei, B. Salvadori, J. Cultural Heritage 2006, 7, pp. 110-115.

[6] M. Ambrosi, L. Dei, R. Giorgi, C. Neto, P. Baglioni, Langmuir, 2001, 17, pp. 4251-4255.

[7] M. Bonini, S. Lenz, R. Giorgi, P. Baglioni, Langmuir, 2007, 23, pp. 8681-8685.

[8] S. Grassi, E. Carretti, P. Pecorelli, F. Iacopini, P. Baglioni, L. Dei, J. Cultural Heritage, 2007, 8, pp. 119-125.

[9] R. Giorgi, C. Bozzi, L.G. Dei, C. Gabbiani, B.W. Ninham, P. Baglioni, Langmuir, 2005, 21, pp. 8495-8501.

[10] R. Giorgi, D. Chelazzi, P. Baglioni, Langmuir, 2005, 21, pp. 10743-10748.

[11] R. Giorgi, L. Dei, M. Ceccato, C. Schettino, P. Baglioni, Langmuir 2002, 18, pp. 8198-8203.

[12] L. Dei, B. Salvadori, J. Cultural Heritage 2006, 7, pp. 110-115.

[13] C. Rodriguez-Navarro, E. Ruiz-Agudo, M. Ortega-Huertas, E. Hansen, Langmuir, 2005, 21, pp. 10948-10957.

[14] a) Ciliberto, E.; Condorelli, G. G.; La Delfa, S.; Viscuso, E., Applied Physics A, 2008, 92, 137-141.

b) Altavilla, C., Ciliberto, E., Editors, "Inorganic Nanoparticles: Synthesis, Applications, And Perspectives". 2011, CRC Press.

[15] T.E. Doll, F.H. Frimmel, Catal. Today, 101, 2005, 195.

[16] H.S. Son, S.J. Le, I.H. Cho, K.D. Zoh, Chemosphere, 57, 2004, 309.

[17] D. Chen, A.K. Ray, Appl. Catal. B-Environ., 23, 1999, 143.

[18] R. Bauer, G. Waldner, H. Fallman, S. hager, M. Klare, T. Krutzler, S. Malato, P. Maletzky, Catal. Today, 53, 1999, 131.

Nanotechnology

Introduction

In the recent years a new branch of research has arisen, broadly referred to as "nanoscale science and technology" [1, 2]. In general, nanotechnology can be understood as a technology of design, fabrication and applications of nanostructures and nanomaterials, as well as a fundamental understanding of physical properties and phenomena of nanomaterials and nanostructures. Nanomaterials, compared to bulk materials, have the scales ranging from individual atoms or molecules to submicron dimensions at least in one dimension. Nanomaterials and nanotechnology have found significant applications in physical, chemical and biological systems. The importance of nanotechnology was pointed out by Feynman at the annual meeting of the American Physical Society in 1959, in the classic science lecture entitled "There is plenty of room at the bottom". Since the 1980s, many inventions and discoveries in the fabrication of nano-objects have been developed. The discovery of novel materials, processes, and phenomena at the nanoscale, as well as the development of new experimental and theoretical techniques for research provide plenty of new opportunities for the development of innovative nanostructured materials. Nanostructured materials can be made up with unique nanostructures and properties.

The ability of scientists to manipulate matter virtually atom by atom has been supported by the development of new instruments and approaches that allow the investigation of material properties

with a resolution close to the atomic level. Such new tools have allowed the extensive understanding of the unusual physical and chemical properties characterizing matter at the nanometer scale opening up the way to the use of nanomaterials in a wide variety of applications involving material science, engineering, physics, chemistry and biology.

Nanoscale semiconductor materials typically show behaviour which is intermediate between that of a macroscopic solid and that of an atomic or molecular system. Consider, for instance, the case of an inorganic crystal composed of very few atoms. By simple intuitive reasoning, it can be perceived that its properties will not be the same as those of a single atom, while also being different from those of a bulk solid.

In order to rationalize (and predict) the physical properties of nanoscale materials, such as their electrical and thermal conductivities, or their absorption and emission spectra, their energy level structure needs first to be determined. Many properties specific to nanosized materials are related to the type of motion the charge carriers (electrons and holes) are allowed to execute when they are forced to dwell in confined structures. The unusual characteristics of these systems can only be explained by the laws of quantum mechanics [3], the behaviour of the particles inside them being obtainable by solving the related Schrödinger equation. For low-dimensional systems, the calculation of the energy structure is traditionally carried out using two main approaches.

An approach, which is more elaborate but also more powerful to derive a detailed description of the electronic band

structure in a low-dimensional solid, represents the general physics of a solid when its dimensions shrink one by one down to a few nanometres. The behaviour of carriers in a bulk solid can be described satisfactorily by the model of the "free-electron gas" [4, 5]. The electrons are considered to be delocalized in the solid and thus not bound to individual atoms. Another assumption is made, that the interactions between the electrons and the crystal potential can be neglected at a first approximation. Whenever the size of the solid becomes comparable to the De Broglie wavelength associated with the particles that interact with it, a free carrier confined in this structure will behave as a particle in a potential box. The solutions of the Schrödinger equation are standing waves confined in the potential well, and the energies associated with two distinct wave functions are, in general, different and discontinuous. The particle energies cannot take on any arbitrary value and the system exhibits a discrete energy level spectrum.

Classification of nanomaterials

Regarding the forms of materials, nanomaterials are classified as zero-, one-, and two-dimensional nanostructures. 1) Zero-dimensional nanostructures, also named as nanoparticles, include single crystal, polycrystalline and amorphous particles with all possible morphologies, such as spheres, cubes and platelets. In general, the characteristic dimension of the particles is one hundred nanometres or less. They can be named as zero-dimensional nanostructures. If the nanoparticles are single crystallite, they are often referred to as nanocrystals. When the characteristic dimension

of the nanoparticles is small enough and quantum effects are observed, quantum dots are the common term used to describe such nanoparticles. 2) One-dimensional (1D) nanostructures include whiskers, fibres or fibrils, nanowires and nanorods. In many cases, nanotubules and nanocables are also considered one-dimensional structures. Although whiskers and nanorods are in general considered to have smaller length to thickness ratio (aspect ratio) than fibres and nanowires, the definition is a little arbitrary. Therefore, for clarity, nanostructures with large aspect ratio are addressed as "nanofibres", albeit they have been termed whisker, rod, fibre, or wire elsewhere. 3) Thin films are two-dimensional nanostructures, which have been a subject of intensive study for almost a century, and for which many methods have been developed and improved.

Properties of nanomaterials

Dramatic changes are introduced in the electronic structure of the solids, depending on how many dimensions collapse. As shown in Figure 1.1, in a bulk three dimensional (3D) material, the density of states $N_{3D}(E)$ varies with the $E^{1/2}$ and the possible states in which an electron can be found are quasi-continuous [6]. For a two dimensional electron gas system (2D, quantum well), $N_{2D}(E)$ is still quasi-continuous, but the density of states is a step-function (i.e. it does not depend on the energy E), and fewer levels are now present [6, 7]. For a one-dimensional system (1D, quantum wires), $N_{1D}(E)$ is proportional to $E^{-1/2}$ and thus exhibits singularities near the band

edges [6]. Finally, in the limiting case when all dimensions shrink, i.e. for a zero-dimensional solid (0D, quantum dot), $N_{0D}(E)$ contains delta peaks, meaning that the bands converge to atom-like energy states, with the oscillator strength compressed into a few transitions [4-7].

A different approach for calculation of the energy structure, which is that generally followed by chemists, considers atomic nuclei and electrons as the basic building blocks of matter. The electronic structure of solids can be described in terms of a combination of atomic orbitals, as it is done with molecules [8, 9]. Atoms are combined to form molecules by starting from discrete energy levels of atomic orbitals and still obtaining discrete levels for the molecular orbitals. When the size of polyatomic systems become progressively larger, the calculation of its electronic structure by this method it's not longer feasible [10-12]. However, tremendous simplification arises if the system under study is a periodic, infinite crystal. The electronic structure of crystalline solids can be, in fact, described in terms of periodic combinations of atomic orbitals (Bloch functions) [4, 5].

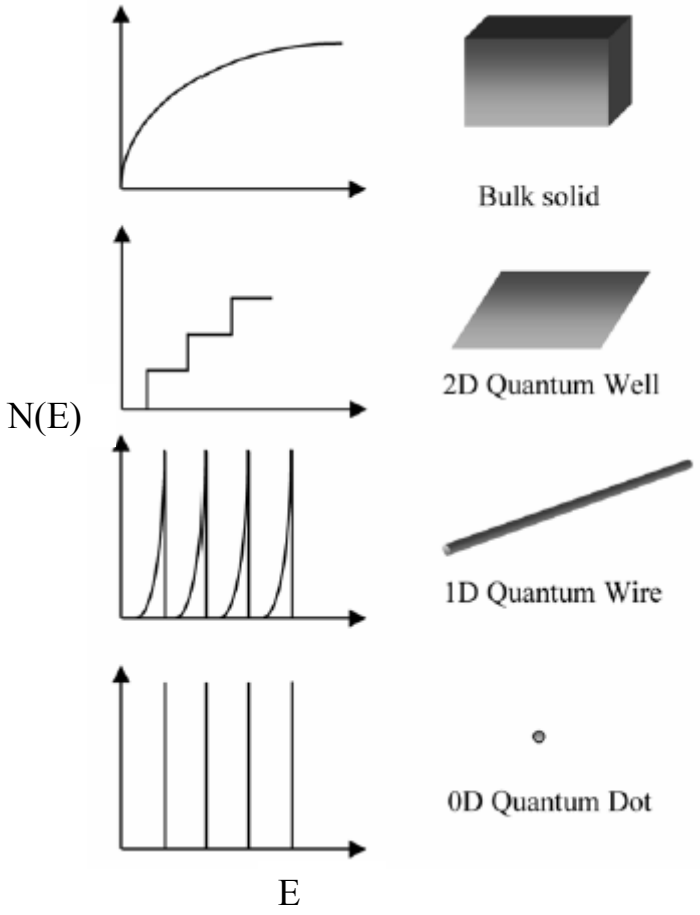

Figure 1.1 Idealized densities of states for one band of a solid of 3, 2, 1 and "0" dimensions [34]

In this model, the conservation of perfect translational symmetry of the crystal structure is assumed and contributions from the surface of the crystal are neglected by supposing an infinite solid (periodic boundary conditions).

Electrons are described as superimpositions of plane waves extended throughout the solid. As opposed to the case of atoms and molecules, the energy structure of a solid no longer consists of

discrete energy levels, but of broad energy bands. Every band can be filled only with a limited amount of charge carriers. Nevertheless, nanometer sized crystals cannot be described by the same way as in the case of bulk materials, as the two underlying assumptions for the validity of the model fail. We can indeed imagine that the electronic structure of a nanocrystal should be something intermediate between the discrete levels of an atomic system and the band structure of a bulk solid. The concept of energy bands and band gap can still be used [13-15]. Highest occupied atomic levels of the atomic (or ionic) species interact with each other to form the valence band of the nanoparticles. Similarly, lowest unoccupied levels combine to form the conduction band of the particles. The energy gap between the valence and the conduction bands results in the band-gap of the nanoparticles. In any material there will be a critical size below which there is a substantial change of fundamental electrical and optical properties with size: these variations will be seen when the energy spacing δ of successive quantum levels ($\delta = 4E_F/3n$, where E_F is the Fermi level of the bulk material and n is the total number of valence electrons in the nanocrystal), exceeds the thermal energy (~25 meV at room temperature). For a given temperature, this occurs at very large value in semiconductors, as compared to metals, insulators, or molecular crystals.

The bands of a solid are centred about atomic energy levels, with the width of the band related to the strength of the nearest-neighbour interactions. The changes in the density of electronic states are more dramatic for semiconductors than for metals (Figure 1.2). Thus, in simple metals, where the Fermi level lies in the centre

of a band, the relevant energy level spacing is still very small, and at a temperature above a few Kelvin, the electrical and the optical properties more resemble those of a continuum, even in relatively small sizes (tens or hundreds of atoms). Accordingly, the band-gap of metallic quantum dots (i.e. a non-metallic behaviour) is observable only at very low temperatures. In semiconductors, however, the Fermi level lies between two bands, so that the edges of the bands dominate the low-energy optical and electrical behaviour. The band-gap of a semiconductor nanocrystal is larger and its effects can be observed at room temperature, even for crystallites as large as 10.000 atoms.

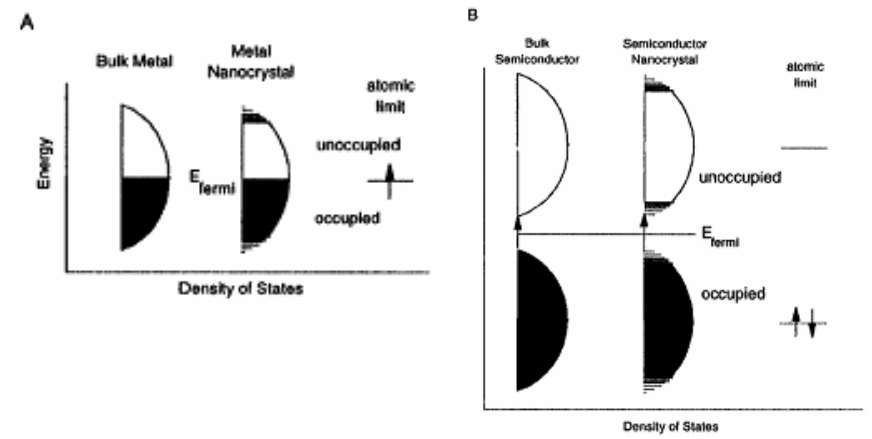

Figure 1.2 Density of states in a metal (A) and semiconductor (B) nanocrystal [34]

Size-dependent properties of nanocrystals

The properties of crystalline solids are ordinarily catalogued without reference to their size. It is only in the regime below 10 nm where this variable comes into play. In the past decade, tailoring of materials characteristics by size control has been demonstrated in many inorganic solids belonging to one of the most technologically important classes of materials: semiconductors.

The main apparent difference between bulk material and nanomaterial lays in the size difference. With decreasing particle size, distinctly different properties of nanomaterial emerge compared to its bulk structure. This makes the nanomaterials a class of novel materials with tremendous new applications. The terminal, size effects, is used to describe the properties change accompanied with particle size change. The effects determined by size pertain to the evolution of structural, thermodynamic electronic, spectroscopic, electromagnetic and chemical features of these finite systems with increasing size.

There are two major effects which are responsible for these size variations in nanocrystal properties. First, in nanocrystals the number of surface atoms is a large fraction of the total. Second, the intrinsic properties of the interior of nanocrystals are governed by "quantum size effects".

In any material, surface atoms make a distinct contribution to the free energy, and the large changes in thermodynamic properties of nanocrystals (melting temperature depression, solid-solid phase transition elevation) can ultimately be traced to this. The surfaces of nanocrystals have until recently been thought of as largely

disordered, yielding spherical or ellipsoidal shapes [16]. More recent work shows that nanocrystals assume regular shapes, with the same well-defined facets as are present in extended crystals [17, 18]. This opens up the possibility of manipulating the surface energy of nanocrystals in a controlled manner. The ability to manipulate the energy of nanocrystal surfaces will have practical consequences.

Independent of the large number of surface atoms, semiconductor nanocrystals with the same interior bonding geometry as a known bulk phase, often exhibit strong variations in their optical and electrical properties with size [19, 20]. These changes arise through systematic transformations in the density of electronic energy levels as a function of the size of the interior, known as "quantum size effects". For example, metal particles of 1–2 nm in diameter exhibit unexpected catalytic activity, as exemplified in catalysis by gold nanoparticles, while gold is chemically inert as a bulk metal. Herewith, we report a brief description of the most striking size-dependent properties of semiconductors and metal nanocrystals.

Melting temperature depression. In a wide variety of materials ranging from metals to semiconductors to insulators, a decrease in solid to liquid transition temperature has been observed with decreasing nanocrystal size [21-25]. An understanding of this depression can be obtained by considering the factors that contribute to the total energy of a nanocrystal: in a system containing only a few hundred atoms, a large fraction of these atoms will be located on the surface. As surface atoms tend to be coordinatively unsaturated, there is a large energy associated with this surface. The key to

understanding this melting point depression is the fact that the surface energy is always lower in the liquid phase compared to the solid phase. In the dynamic fluid phase, surface atoms move to minimize surface area and unfavourable surface interactions. In the solid phase, rigid bonding geometries cause stepped surfaces with high-energy edge and corner atoms. By melting, the total surface energy is thus reduced. The smaller the nanocrystal, the larger the contribution made by the surface energy to the overall energy of the system and thus the more dramatic the melting temperature depression. As melting is believed to start on the surface of a nanocrystal, this surface stabilization is an intrinsic and immediate part of the melting process [26, 27] (Figure 1.3A).

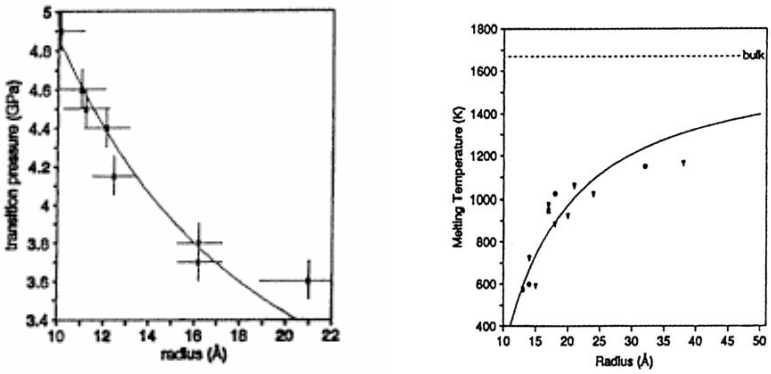

Figure 1.3 (A) Size dependence pressure-induced structural transformation (B) Melting temperature versus size for nanocrystals [34]

Solid-solid phase transition pressure elevation. As the nanocrystals decrease in size, the pressure required to induce transformation to more dense phases increases (Figure 1.3B) [28, 29]. Experimental results have suggested that there must be well-defined pathways by

which nanocrystals convert from one structure to another. Structural transformations are catalyzed by crystal defects, which act as low-energy nucleation sites for solid-solid phase transitions, and then propagate along the solid. As in a nanocrystal, the probability of occurrence of defects is low and the phase transition pressure tends to increase as compared to the bulk solid. Moreover, well-formed nanocrystals are often faceted with a defined shape which reflects the lowest energy arrangement of the atoms. In a nanocrystal, a great fraction of unstable surface sites must be created for a transformation to occur. The importance of surface energy in determining the stability of one structure over another in the nanocrystal regime is illustrated by the possibility of trapping nanocrystals in dense phases which are unstable in the bulk [30].

Size/shape dependence of optical transitions. In semiconductor nanoparticles, the most striking effect of quantum confinement is the systematic variation of the density of electronic states as a function of size [31]. A widening of the energy gap (E_g) between the highest occupied electronic states (the top of the original valence band) and the lowest unoccupied states (the bottom of the original conduction band) is accompanied by the development of well-defined energy levels at the band edges (Figure 1.4). The minimum energy needed to create an electron-hole pair in a quantum dot (an "exciton") is dictated by E_g. These facts can be clearly observed in their optical absorption spectra: the threshold energy for absorption is shifted to shorter wavelengths with decreasing particle size and discrete spectral features develop in the spectrum, which correspond to the allowed optical transitions. Furthermore, as the energy from exciton

annihilation is too large to be dissipated by vibrational modes, it can be easily released in form of emitted photons, i.e. of fluorescence. The positions of the lowest energy absorption peak (which is usually the most defined) as well as that of the luminescence peak are strictly correlated to the average quantum dot size, while their widths are correlated to the remaining size distribution. In anisotropic nanocrystals, such as nanorods, the shift behaviour of the exciton peak is characteristically dependent on the shortest confined dimension. The size dependent evolutions of the absorption spectrum of semiconductor nanocrystals can thus be a powerful tool for real time-monitoring of their growth in colloidal solutions.

Size dependence of surface plasmon absorption. In colloidal noble metal nanoparticles, the decrease in size below the electron mean free path (the distance the electron travels between scattering collisions with the lattice centres) gives rise to intense absorption in the visible-near UV region. The optical absorption spectra exhibit an absorption peak that looks similar to that of semiconductor particles; however, it does not derive from quantum confinement effects. Such absorption results from the collective oscillations of the itinerant free electron gas on the particle surface that is induced by the incident electromagnetic wave, and it is called the surface plasmon (SP) absorption [32]. The resonances are seen when the wavelength of incident light far exceeds the particle diameter. In the “intrinsic size” region (< 5 nm), noble metal nanoparticles do not show any plasmon absorption, while the absorption of particles larger than 50 - 60 nm (“extrinsic size” region) is broad and covers most of the visible region. The spectrum is thus strongly dependent on the size regime

of the particles and it becomes further modified for anisotropic particles.

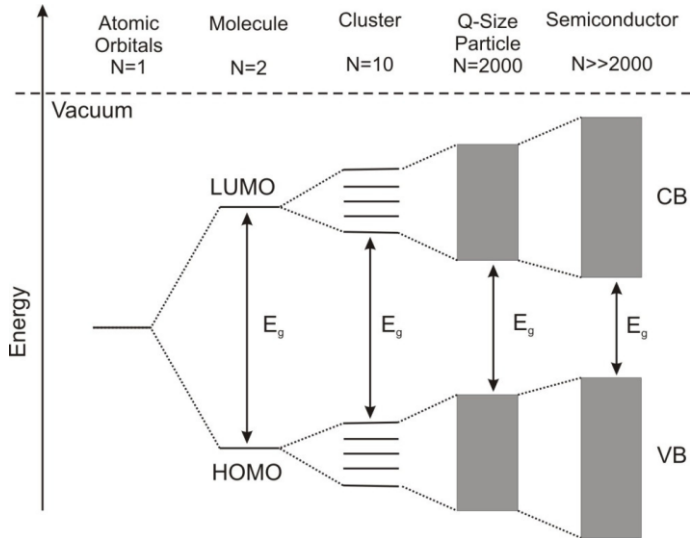

Figure 1.4 Band edge discretization in nanocrystalline semiconductor

Charging energy. In an extended solid, the addition of one extra charge, i.e. an electron, does not alter the electronic structure significantly. The energy required to add successive charges also does not vary. As opposed, the capacity of a nanostructure may become so small that the energy required to charge the structure with one additional charge carrier exceeds the thermal energy available [30]. In this case, charge transport through the structure is blocked. Thus, in metals or semiconductors, the current-voltage curves of individual crystallites resemble a staircase, due to this "Coulomb blockade". Steps in the staircase due to individual charging events are spaced proportional to 1/r, where r is the radius of the confined structure.

Superparamagnetism. In nanoparticles of transition metals, the magnetic moment per atom shows marked variations with size. Nanosized ferromagnetic materials behave as "single magnetic domains" and the kinetics of magnetic phase transitions is relatively simple. At temperatures sufficiently below the Curie temperature, all the spins in the nanocrystals are aligned, and the resulting "super" spin follows the applied field with no hysteresis, up to the saturation magnetization (fully aligned). An ensemble of nanomagnets behaves as a single, giant paramagnetic atom and the direction of magnetization is easily influenced by thermal fluctuations of the local environment. This phenomenon is called "superparamagnetism" [30, 33].

Synthesis approaches and techniques

In order to explore novel physical properties and phenomena and realise potential applications of nanostructures and nanomaterials, the ability to fabricate and process nanomaterials and nanostructures is the first corner stone in nanotechnology. There are two approaches (Figure 1.5) to the synthesis of nanomaterials and the fabrication of nanostructures: top-down and bottom-up. The top-down approach refers to slicing or successive cutting of a bulk material to get nanosized particles. The bottom-up approach refers to the build-up of a material from the bottom: atom-by-atom, molecule-by-molecule, or cluster-by-cluster. For example, milling is a typical top-down method in making nanoparticles, whereas the colloidal dispersion is a good example of the bottom-up approach in the

synthesis of nanoparticles. Both approaches play very important roles in nanotechnology.

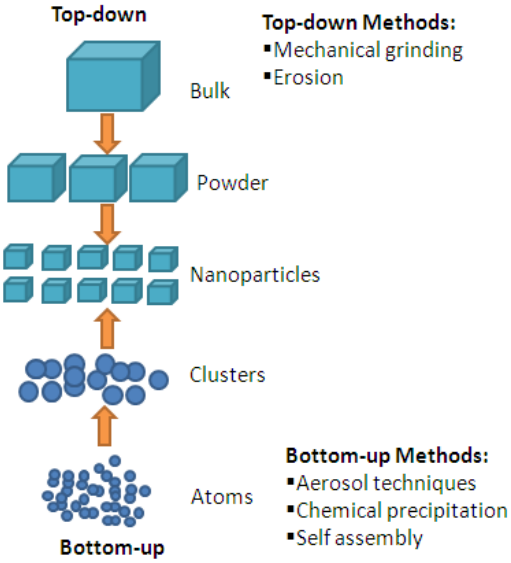

Fig. 1.5 Schematic representation of the 'bottom-up' and 'top-down' approaches

References

[1] Lane, N. Journal of Nanoparticle Research, 3 (2001) 95.

[2] Service R. F., Science, 290 (2000) 1526.

[3] Cohen-Tannoudji, C., Diu, B., Laloe, F., Quantum Mechanics, John Wiley & Sons: New York (2006).

[4] Kittel, C., Introduction to Solid State Physics, 8th edn., R. Oldenbourg Verlag: John Wiley & Sons: New York (2004).

[5] Ashcroft, N. W.; Mermin, N. D., Solid State Physics, Saunders College: Philadelphia (1976).

[6] Davies, J. H.; The Physics of Low-Dimensional Semiconductors; Cambridge University Press: Cambridge (1998).

[7] Moriarty, P., Reports on Progress in Physics (2001), 64, 297.

[8] Atkins, P. W., Physical Chemistry; 5th Edn.; Oxford University Press: Oxford (1991).

[9] Karplus, M.; Porter, R. N. Atoms and Molecules, 1st edn. ; W. A. Benjamin, Inc.: New York (1970).

[10] Harrison, W. A., Electronic Structure and the Properties of Solids: The Physics of the Chemical Bond; Dover Publication: Dover (1989).

[11] Kobayashi, A.; Sankey, O. F.; Volz, S. M.; Dow, J. D., Phys. Rev. B, 28 (1983) 935.

[12] Burdett, J. K.; Progress in Solid State Chemistry 15 (1984) 173.

[13] Ekimov, A. I.; Onushchenko, A. A. Fiz., Sov. Phys.- Semicond. 16 (1982) 775.

[14] Rossetti, R.; Nakahara, S.; Brus, L. E. J., Chem. Phys. 79 (1983) 1086.

[15] (a) Cohen, M. L.; Chou, M. Y.; Knight, W. D.; de Heer, W. A. J. Phys. Chem. 91 (1987) 3141. (b) Wang, C. R. C.; Pollak, S.; Dahlseid, T. A.; Koretsky, G. M.; Kappes, M. J. Phys. Chem. 96 (1992) 7931. (c) Ellert, C.; Schmidt, M.; Schmitt, C.; Reiners, T.; Haberland, H. Phys. Rev. Lett. 75 (1995) 1731.

[16] Murray, C. B.; Norris, D. B.; Bawendi, M. G., J. Am. Chem. Soc. 115 (1993) 8706.

[17] Alivisatos, A. P., Mater. Res. Soc. Bull. 20 (1995) 23.

[18] Shiang, J. J.; Kadavanich, A.; Grubbs, R. K.; Alivisatos, A. P., J. Phys. Chem., (1995), 99 (48).

[19] Ekimov, A. I.; Onushchenko, A. A. Fiz. Tekh. PoluproVodn. 16 (1982) 1215.

[20] Rossetti, R.; Nakahara, S.; Brus, L. E. J. Chem. Phys. 79 (1983) 1086.

[21] Coombes, C. J. J. Phys. 2 (1972) 441.

[22] Buffat, P.; Borel, J.-P. Phys. Rev. A 13 (1976) 2287.

[23] Castro, T.; Reifenberger, R.; Choi, E.; Andres, R. P. Phys. ReV. B:Condens. Matter 42 (1990), 8548.

[24] Beck, R. D.; St. John, P.; Homer, M. L.; Whetten, R. L. Science 253 (1991) 879.

[25] Martin, T. P.; Naher, U.; Schaber, H.; Zimmermann, U. J. Chem.Phys. 100 (1994) 2322.

[26] Couchman, P. R.; Jesser, W. A., Nature, 269 (1977) 481

[27] Ercolessi, F.; Andreoni, W.; Tosatti, E., Phys. Rev. Lett., 66 (1991) 911.

[28] Besson, J. M.; Itie, J. P.; Polian, A.; Weill, G.; Mansot, J. L.; Gonzalez, J. Phys. Rev. B - Condensed Matter 44 (1991) 4214.

[29] (a) Chen, C. C.; Herhold, A. B.; Johnson, C. S.; Alivisatos, A. P. Science 276 (1997) 398. (b) Herhold, A. B.; Chen, C. C.; Johnson, C. S.; Tolbert, S. H.; Alivisatos, A. P. Appl. Phys. Lett. 68 (1996) 2574.

[30] (a) Alivisatos, A. P., Phys. Chem. Chem. Phys. 101 (1997) 1573. (b) Alivisatos, A. P., J. Phys. Chem. 100 (1996) 13226.

[31] Gaponenko, S. V. "Optical Properties of Semiconductor Nanocrystals", Cambridge University Press, 1998.

[32] a) Hodak, J. H.; Henglein, A.; Hartland, G. V. Pure Appl. Chem. 72 (2000) 189. (b) Mulvaney, P. Langmuir 12 (1996) 788. (c) Kamat, P. V. J. Phys. Chem. B 106 (2002) 7729.

[33] (a) Shi, J.; Gider, S.; Babcock, K.; Awschalom, D. D. Science 271 (1996) 937. (b) Billas, I. M; L.; Chatelain, A.; deHeer, W. A. Surf. Rev. Lett. 271 (1996) 937.

[34] Comparelli R., PhD thesis, Bari (Italy), 2005.

Catalysis

Introduction

Metal oxides have wide industrial applications in the field of catalysis by serving as active compositions or as supports. There are a lot of opportunities in modifying nanostructures to improve substantially the catalytic activity and selectivity of existing catalysts. Catalysts are species that are capable of directing and accelerating thermodynamically feasible reactions while remaining unaltered at the end of the reaction. They cannot change the thermodynamic equilibrium of reactions [1, 2]. The performance of a catalyst is largely measured in terms of its effects on the reaction kinetics. The catalytic activity is a way of indicating the effect the catalyst has on the reaction rate and can be expressed in terms of the rate of the catalytic reaction, the relative rate of a chemical reaction (i.e. in comparison to the rate of the uncatalysed reaction) or via another parameter, such as the temperature required to achieve a certain conversion after a particular time period under specified conditions. Catalysts may also be evaluated in terms of their effect on the selectivity of a reaction, specifically on their ability to give one particular reaction product. In some cases, catalysts may be used primarily to give high reaction selectivity rather than high conversion rate. Stability is another important catalyst property since catalysts are expected to lose activity and selectivity with prolonged use. This then opens the way to regenerability which is a measure of

the catalyst's ability to have its activity and/or selectivity restored through some regeneration process. Catalytic processes are the application of catalysts in chemical reactions. In the manufacture of chemicals, catalysis is used to make an enormous range of products, for examples heavy chemicals, commodity chemicals and fine chemicals. Catalytic processes are used throughout fuels processing, in petroleum refining, in synthesis gas conversion, and in coal conversion. More recently, the demand for clean technology or environment protection has driven most of the new developments in catalysis.

Catalysis is described as homogeneous when the catalyst is soluble in the reaction medium and heterogeneous when the catalyst exists in a phase distinctly different from the reaction phase of the reaction medium [3]. Many homogeneous catalytic processes are liquid phase and operate at moderate temperatures (< 150 °C) and pressures (< 20 atm).

Photocatalysis

In 1839 Becquerel [4] reported that a voltage and an electric current were produced when a silver chloride electrode, immersed in an electrolyte solution and connected to a counter electrode, was illuminated with sunlight. It is not usually recognized that many examples of semiconductor photocatalysis had already been reported in the literature by the beginning of the last century. Most notably, the semiconductor ZnO had attracted a great deal of attention at the

turn of this century as a photosensitizer for the decomposition of organic compounds [5]. In 1929, it was known that the pigment "titanium white", namely TiO_2, was responsible for fading in paints [6], and several major studies into sensitized action of TiO_2 followed [7]. During the 1960s, much of the theory of semiconductor photoelectrochemistry was developed, most notably through the contribution of Gerischer [8] and Pleskov and co-workers [9-11].

In 1972, Fujishima and Honda discovered the photocatalytic splitting of water on TiO_2 electrodes [12]. This event marked the beginning of a new era in heterogeneous photocatalysis. Since then, research efforts in understanding the fundamental processes and in enhancing the photocatalytic efficiency of TiO_2 have come from extensive research performed by chemists, physicists, and chemical engineers. In recent years, applications pertaining to environmental cleanup have been one of the most active areas in heterogeneous photocatalysis. This has been inspired by the potential application of semiconductors-based photocatalysts for the total destruction of organic compounds in polluted air and wastewater [13, 14].

In a heterogeneous photocatalytic system, photoinduced molecular transformations or reactions take place at the surface of a catalyst. Depending on where the initial excitation occurs, photocatalysis can be generally divided into two classes of processes. When the initial photoexcitation occurs in an adsorbate molecule which then interacts with the ground state catalyst substrate, the process is referred to as a catalyzed photoreaction. When the initial photoexcitation takes place in the catalyst substrate and the photoexcited catalyst then transfers an electron or energy

into a ground state molecule, the process is referred to as a sensitized photoreaction.

Mechanism of photocatalysis

Materials can be divided into 3 different groups, depending of their band gap energies (Fig. 2.1):

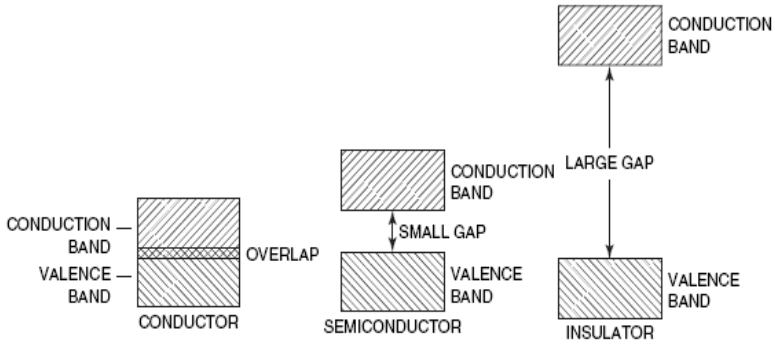

Fig. 2.1 Classification of materials depending of their band gap energies

Materials used in photocatalysis are usually metal oxide semiconductors and activation can be done using photons of right energy: the power of semiconductor based photocatalysts, such as TiO_2, is due to charge separation ability (Fig. 2.2). When a nano-semiconductor is illuminated under a light with energy larger than the band gap, an excitation of an electron from the valence band to the conduction band is observed, leaving a hole at the valence band. The separated hole has a strong oxidation power to obtain an electron from the absorbed species. The separated charge and hole can also recombine to release energy in the form of heat.

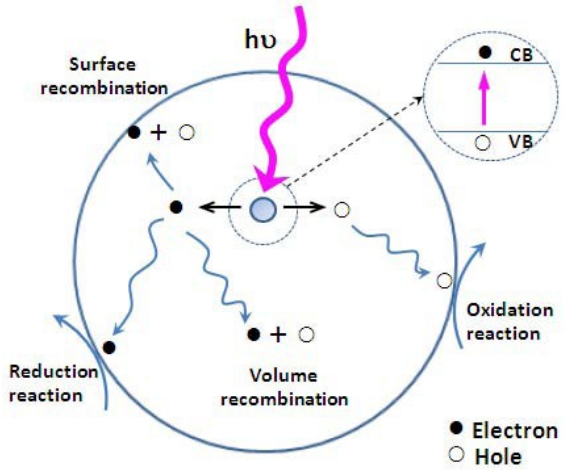

Fig .2.2 Schematic illustration of the charge separation theory of semiconductor upon a photoexcitation (adapted from ref. [15]).

To enhance the photocatalysis, electron-hole pair recombination must be suppressed. This can be achieved by trapping either the photogenerated electrons or the photogenerated holes at trapping sites in the structure. The band gap of a semiconductor determines its working wavelength. The semiconductors with either too large or too narrow band gaps are not suitable for practical use. The reason is that larger band gap will not cause any reaction while narrow band gap materials will have to face the problem of light erosion. The band gaps of different semiconductors are shown in Figure 2.3. Until now, TiO_2 (anatase, band gap ~ 3.2 eV) is the most extensively studied material for photocatalysts because of its strong oxidizing power, low toxicity, and long-term photostability.

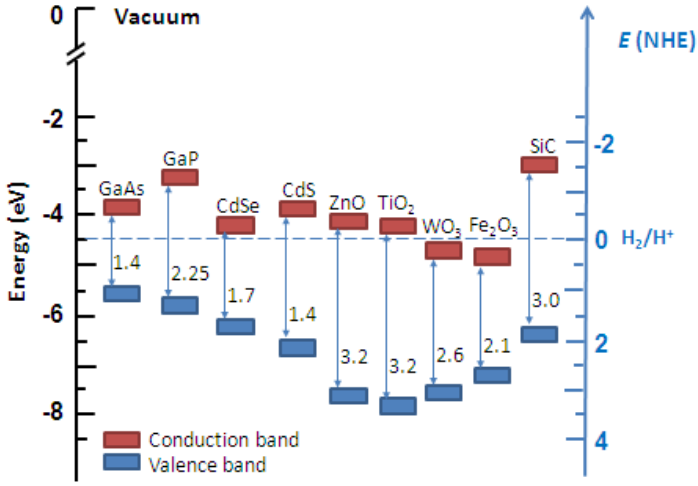

Fig. 2.3 Energy diagrams for various semiconductors in aqueous electrolytes at pH = 1 (adapted from ref. [15]).

The energy that the Earth receives from the Sun is gigantic: 3×10^{24} joules a year, which is about 10,000 times more the energy that the global population currently consumes [16]. In other words, if we could only exploit 0.01 % of this incoming solar energy for the profit of humankind, we could solve the problem of energy shortage. Any improvement in the utilization of sun rays will make a profound positive effect on modern science and technology.

A great deal of effort has been devoted to photoeletrochemical process such as splitting of water [17, 18] and reduction of carbon dioxide for the conversion of solar energy into chemical energy [19, 20]. In addition to applying photocatalysts for energy renewal and energy storage, applications of photocatalysts to environmental cleanup have been one of the most active areas in heterogeneous photocatalysis [21-23].

Radical pathways

Once the photogenerated electron-hole pair reaches the catalyst surface in water media (as shown in Figure 2.2), it gives rise to a series of reactions ultimately leading to the formation of hydroxyl radicals. In detail, it is broadly accepted that photogenerated holes (h^+) could oxidize H_2O or -OH groups present on the catalyst surface giving rise to hydroxyl radicals ($^{\bullet}OH$) [23]:

$$\text{Semiconductor (SC)} + h\nu \rightarrow \text{SC}\,(e^- + h^+) \quad (1)$$

$$h^+ + OH^- \rightarrow {}^{\bullet}OH \quad (2)$$

$$h^+ + H_2O \rightarrow {}^{\bullet}OH + H^+ \quad (3)$$

Under ambient atmosphere, molecular oxygen acts as a photogenerated electron (e^-) scavenger initiating a series of reactions taking place in aqueous media ultimately yielding $^{\bullet}OH$ group:

$$O_2 + e^- \rightarrow O_2^{\bullet-} \quad (4)$$

$$O_2^{\bullet-} + H^+ \rightarrow HO_2^{\bullet} \quad (5)$$

$$HO_2^{\bullet} + HO_2^{\bullet} \rightarrow H_2O_2 + O_2 \quad (6)$$

$$O_2^{\bullet-} + HO_2^{\bullet} \rightarrow O_2 + HO_2^- \quad (7)$$

$$HO_2^- + H^+ \rightarrow H_2O_2 \quad (8)$$

$$H_2O_2 + h\nu \rightarrow 2\ {}^{\bullet}OH \quad (9)$$

$$H_2O_2 + O_2^{\bullet-} \rightarrow HO^{\bullet} + OH^- + O_2 \quad (10)$$

$$H_2O_2 + e^- \rightarrow HO^{\bullet} + OH^- \quad (11)$$

General applications of photocatalysis

Recent developments in the domain of chemical water treatment have led to an improvement in oxidative degradation procedures for organic compounds dissolved or dispersed in aqueous media, by applying catalytic and photochemical methods. They are generally referred to as Advanced Oxidation Processes (AOP). This domain is particularly oriented towards applications and has already had a strong impact on design and construction of new light sources, photochemical reactors, and the preparation of new photocatalysts and their support. AOP methods exploit the high reactivity of hydroxyl radicals in driving oxidation processes, ultimately resulting in the mineralization of a variety of environmental contaminants. In this field of research, UV-induced photocatalytic degradation assisted by semiconductors represents a very appealing tool to implement low cost purification of waste waters on large scale.

Nanoparticles catalysis

Nanoparticles have attracted a great interest as a subject for scientific research and industrial application under the internationally big research boom of nanoscience and nanotechnology starting from the Clinton's statement in 2000 [24], because nanoparticles are easily prepared even in single-nanometer size and their applications to catalysis successfully give the productive results as a fundamental research. However, nanoparticles already had a long history as nanometer-scale materials before the Clinton's statement. Soluble gold NPs appeared

about two thousand years ago and were used as pigments for aesthetic and curative purposes. On the materials side, their use to make ruby glass and for colouring ceramics was known in these ancient times, as exemplified by the famous Lycurgus cup (dated 4th century B.C., British Museum) [25].

In the history of colloid chemistry, metal nanoparticles, which are called colloidal metal or metal fine particles, have been recognized as a research subject by scientists more than 150 years ago. For example, Michael Faraday reported the preparation of gold sols (colloidal dispersion of gold nanoparticles in water) in 1857 [26], although he could not measure at that time the size of gold nanoparticles. However, the gold nanoparticles he prepared were reproduced by his successor at Royal Institution in London, J. M. Thomas, who demonstrated that the particle size is 3–30 nm in diameter [27].

Nevertheless, nanoparticles in catalysts have a long history too. Human beings had used some materials as a special additive to accelerate practical reactions in history. However, J. J. Berzelius recognized the catalysis as a special phenomenon in 1835 and W. Ostwald gave the definition of catalysis in 1901, when the chemistry of catalysis started practically. Ostwald also defined “colloid” as a dispersion state of materials. Thus, both concepts of “colloid” and “catalysis” had a strong relationship even from the beginning.

One reason of the great reactivity of nanoparticle catalyst can be found in the percentage of “active” atoms, namely those located on the external faces, edges or corners.

Figure 2.4 shows the relationship between the diameter (d/nm) of

nanoparticles and the percentage (r/%) of surface atoms in total atoms constructing a nanoparticle. The percentage of surface atoms rapidly increases with decreasing the particle size, especially less than 5 nm. If the diameter is less than 2.5 nm, more than half of the atoms are located at the outermost surface layer of the particle [28].

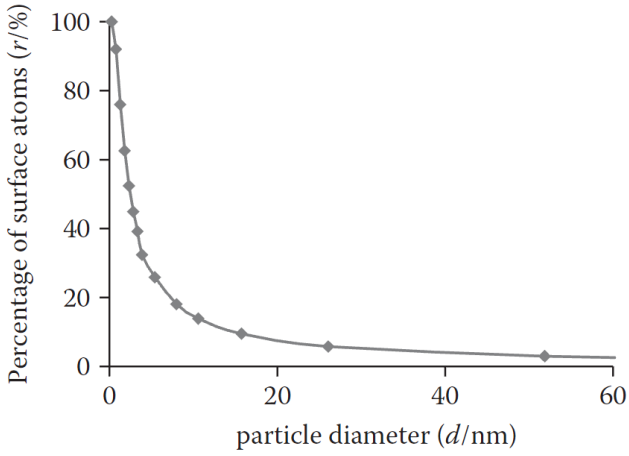

Figure 2.4 relationship between particle diameter (d/nm) and percentage of surface atoms in total atoms (r/%).

The corner atoms commonly have the highest number of vacant coordination position among surface atoms. If the activity of the surface atom increases with increasing the number of vacant coordination position, then the catalytic activity of the surface atoms increases in the following order: face < edge < corner. Thus, the increase of the corner atom with decreasing the size could provide the very effective catalyst for such reactions, which we call structure-sensitive reactions.

A new concept of nanoparticle catalysts is becoming very popular in science and technology and is going to provide a new frontier in science of material conversion: inorganic catalysts in nanometer scale receive an attention, which gives a new concept of catalysis [28].

References

[1] G. Ertl, H. Knozinger, J. Weitkamp, Handbook of Heterogeneous Catalysis, Wiley-VHC, Weinheim (1997).

[2] C. L. Thomas, Catalytic Processes and Proven Catalysts, Academic Press, New York, (1970).

[3] J. M. Thomas, W. J. Thomas, Principles and Practice of Heterogeneous Catalysis, VCH, NY (1996).

[4] Becquerel, E. C.R., Acad. Sci., 9 (1839) 561.

[5] Perret, A. J.Chim. Phys., 23 (1926) 97.

[6] Keidel, E. Furben Zeitung, 34 (1929) 1242.

[7] Goodeve C.F., Kitchnere, J.A. Trans. Faraday Soc., 34 (1938) 570.

[8] Gerischer, H. Eyring, H., Henderson D., Jost, W. (Eds.) Physical Chemistry – An Advanced Treatise, Academic Press, New York (1970).

[9] Myamlin, V.A. Pleskov, Y. Electrochemistry of Semiconductors, Plenum, New York (1967).

[10] Pleskov, Y.V. Gurevich, Y.Y. Semiconductor Photoelectrochemistry, Plenum, New York (1986).

[11] Pleskov, Y.V. Solar Energy Conversion, Springer-Verlag, Berlin (1990).

[12] Fujishima, A.; Honda, K., Nature, 37 (1972) 238.

[13] Schiavello, M., Ed. Photocatalysis and Environment; Kluwer Academic Publishers: Dordrecht (1988).

[14] Ollis, D. F., Al-Ekabi, H., Eds. Photocatalytic Purification and Treatment of Water and Air, Elsevier: Amsterdam (1993).

[15] A. L. Linsebigler, G. Q. Lu, J. T. Yates, Chem. Rev., 95 (1995), 735-758.

[16] M. Grätzel, Nature, 414 (2001) 338-344.

[17] M. Ni, M. K. H. Leung, D. Y. C. Leung, K. Sumathy, Renew. Sust. Energy Rev. 11 (2007) 401-425.

[18] Z. G. Zou, J. H. Ye, K. Sayama, H. Arakawa, Nature, 414 (2001) 625-627.

[19] K. Koci, L. Obalova, L. Matejova, D. Placha, Z. Lacny, J. Jirkovsky, O. Solcova, Appl. Catal. B, 89 (2009) 494-502.

[20] H. Yamashita, H. Nishiguchi, N. Kamada, M. Anpo, Y. Teraoka, H. Hatano, S. Ehara, K. Kikui, L. Palmisano, A. Sclafani, M. Schiavello, M. A. Fox, Res. Chem. Intermed., 20 (1994) 815-823.

[21] M. R. Hoffmann, S. T. Martin, W. Y. Choi, D. W. Bahnemann, Chem. Rev., 95 (1995) 69-96.

[22] M. I. Litter, Appl. Catal. B, 23 (1999) 89-114.

[23] M. A. Fox, M. T. Dulay, Chem. Rev., 93 (1993) 341-357.

[24] http://en.wikipedia.org/wiki/National_Nanotechnology_Initiative http://marcomm.caltech.edu/events/presidential_speech/pspeechtxt.html

[25] M. C. Daniel, D. Astruc, Chem. Rev., 104, (2004), 293.

[26] M. Faraday, Phil. Trans. Roy. Soc., 147, (1857), 145–181.

[27] J. M. Thomas, Pure Appl. Chem., 60, (1988), 1517–1527.

[28] N. Toshima, “Inorganic Nanoparticles for Catalysis” in

"Inorganic Nanoparticles: Synthesis, Applications, and Perspectives" edited by C. Altavilla and E. Ciliberto, Taylor and Francis Group, 2011.

Titanium Dioxide

Introduction

Titanium is the world's fourth most abundant metal and ninth most abundant element. It was discovered in 1791 in England by Reverend William Gregor, who recognised the presence of a new element in ilmenite. It was then rediscovered in rutile ore several years later by a German chemist, Heinrich Klaporth who named it after Titans, mythological sons of goddess "Gaia" (earth in Greek mythology). Titanium is not found in its elemental state, it occurs mainly in minerals like rutile, ilmenite, leucoxene, anatase, brookite, and perovskite. It is also found in titanates and many iron ores.

Figure 3.1 shows the 3 main natural phases of TiO_2: anatase (tetragonal), rutile (tetragonal), and brookite (orthorhombic):

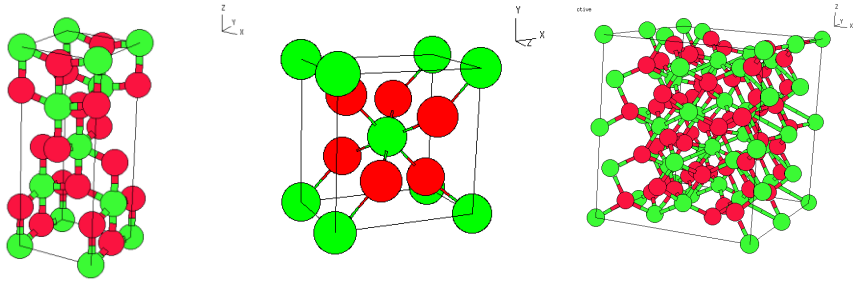

Anatase (A) Rutile (B) Brookite (C)

Fig. 3.1 Elemental unit cells of anatase (A), rutile (B) and brookite (C)

At lower temperatures the anatase and brookite phases are more stable, but both will revert to the rutile phase when subjected to high

temperatures. Although rutile is the most abundant of the three phases, many quarries and mines containing only the anatase or brookite form exist. The optical properties of each phase are also similar, however there is a slight difference among them. For photocatalytic processes, anatase is the preferred structure, although all three forms have shown to be active.

Anatase and brookite are metastable phases and they transform to rutile in the range of 973K – 1173K (Figure 3.2). The anatase to rutile transformation (ART) temperature depends on purity, type of impurities, particle shape/size, atmosphere and reaction conditions. Reidy et al. [1] discussed the role of the critical particle size i.e. about 45 nm as a main parameter of ART irrespective of the purity and the type of impurity in the anatase. The size dependence of the ATR is related to the surface free energy, which is lower for anatase than that of rutile, which is the reverse of the bulk situation [1, 2]. Rutile, due to its thermodynamical stability is the most extensively studied among all TiO_2 forms. In the anatase and rutile structures, each titanium ion is in the centre of an oxygen octahedron, but in rutile the oxygen ions form a slightly distorted hexagonal compact lattice and in anatase form a cfc lattice (Fig. 3.1). In both structures, each oxygen ion is coplanar near neighbour titanium cations. The three Ti-O-Ti angles are roughly equal to 120° in rutile. On the other hand, in anatase one Ti-O-Ti angle is about 180° while the other two are close to 90°. The various Ti-O-Ti angle values result in a significant widening of the d bands with an accompanying decrease in effective mass and an increase in

mobility. Basic crystallographic properties [3, 4] of titanium dioxide are listed below:

Table 3.1 Titanium dioxide properties

Property	Anatase	Rutile	Brookite
Melting point (°C)	~ 1825	~ 1825	~ 1825
Boiling Point (°C)	2500 ~ 3000	2500 ~ 3000	2500 ~ 3000
Crystallographic structure	Tetragonal	Tetragonal	Orthorhombic
Space group	I41/amd	P42/mmm	Pcab
Lattice parameters (nm)	a = 0.3784 b = 0.9515	a = 0.4594 c = 0.2959	a = 0.5442 b = 0.9168
Unit cell volume [10^{-3} nm^3]	34.172	31.216	32.567
Density at 298 K (g/cm^3)	4.230	4.250	4.133
Band gap energy (eV)	3.20	3.03	2.99

Other information can be obtained from phase diagrams of polymorphic forms [5, 6]:

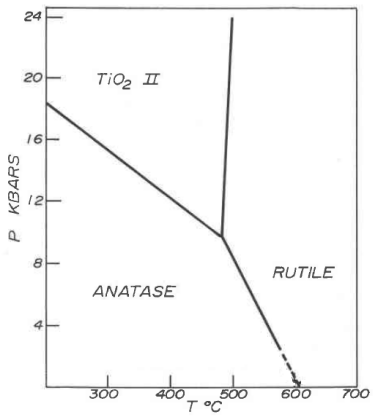

Fig. 3.2 TiO_2 phase diagram (pressure versus temperature)

TiO_2 in Anatase metastable phase

The anatase polymorph of TiO_2 is one of its two metastable phases together with brookite phase. For calcination processes above 700 °C all anatase structure becomes rutile. Some authors also found that 500 °C would be enough for phase transition from anatase to rutile when thermal treatment takes place. Anatase structure is tetragonal, with two TiO_2 formula units (six atoms) per primitive cell. Lattice parameters are: a = b = 3.7710 Å and c = 9.430 Å with c/a ratio of 2.5134.

TiO_2 in Rutile stable phase

TiO_2 owing to its chemical and mechanical stabilities, titanium dioxide (TiO_2), which is a wide energy gap n-type semiconductor, has been mainly used to develop gas sensors based in thick film polycrystalline material or small particles. Its unit cell contains Ti atoms occupy the centre of a surrounding core composed of six oxygen atoms placed approximately at the corners of a quasi-regular octahedron. The lattice parameters correspond now to a = b = 4.5933 Å and c = 2.9592 Å with c/a ratio of 0.6442.

TiO_2 in Brookite phase

Brookite was first discovered in 1849 in Magnet Cove, a site of large deposits of the mineral. It was originally dubbed “arkansite” for the state it was discovered in Arkansas. The brookite structure is more complicated and has a larger cell volume than the other two forms. It is also the least dense of the three forms. The unit cell is

composed of eight formula units of TiO_2 and is formed by edge sharing TiO_2 octahedra, similar to rutile and anatase. Brookite belongs to the orthorhombic crystal system and its space group is Pbca. By definition, the brookite structure is of lower symmetry than its TiO_2 counter morphs, the dimensions of the unit cell are unequal. Also the Ti-O bond lengths vary more in the rutile or anatase phases, like the O-Ti-O bond angles do.

Depending of the stoichiometry, pressure and temperature, other possible forms can exist [6], as shown in Fig. 3.3:

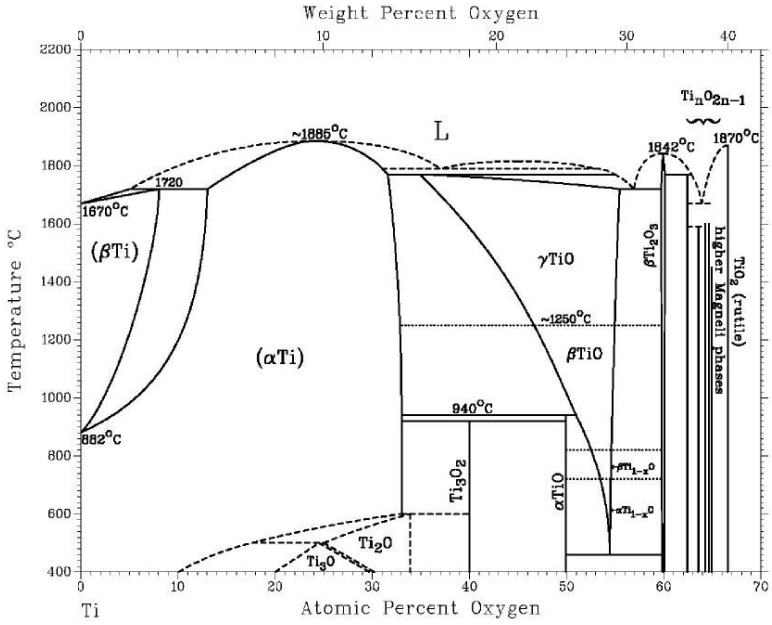

Fig. 3.3 TiO_2 phase diagram (temperature versus composition)

For example, two new high pressure forms, a monoclinic baddeleyite-like form and an orthorhombic α-PbO_2-like form, both found recently at the Ries crater in Bavaria [7, 8].

TiO_2 as nano-photocatalyst

Among all the oxide semiconductors that have been examined, titanium dioxide (TiO_2) is the most studied due to its excellent photocatalytic properties and availability.

It is utilized in a range of fields such as: solar cells, photoelectrochemistry, photocatalyst for environmental applications, semiconductor (i.e. gas application), self clean-up surfaces (for its hydrophilic and hydrophobic properties in the absence or in the presence of UV-Vis light), with many applications in everyday life: white pigments, cements, papers, beauty creams, food additives, etc, and recently also as killing bacteria agent [9]:

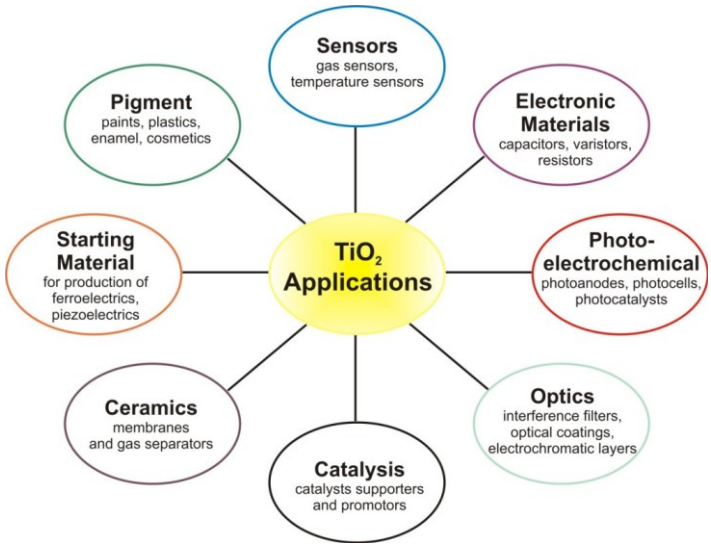

Fig. 3.4 Applications of TiO_2

Many good reviews [10-12] and books [13, 14] have been written on this photocatalyst; TiO_2, in its anatase form, possesses

desirable properties for applications in homogenous and heterogeneous catalysis such as:

- high surface area;
- limited toxicity;
- high availability & low cost;
- excellent thermal and photochemical stability;
- water insolubility & photocatalyst recyclability;
- no expensive and dangerous oxidizing chemicals such as O_3 or H_2O_2 (dissolved oxygen or air is sufficient) are used;
- free light source (solar light).

In its rutile form, the TiO_2 photocatalytic ability is greatly reduced [15-17].

Photocatalytic reactions on TiO_2 surfaces are very important for environmental removal of both air pollutants and water purification, such as the oxidation of organic and inorganic pollutants (HCHO, NO_x, etc) and the reduction of heavy metals; moreover complete mineralization of a wide variety of organic compounds to CO_2 and H_2O has been reported [18-21].

Electron – hole pairs are formed when TiO_2 is irradiated with photons of greater energy than its band gap (3.2 eV for pure anatase):

$$TiO_2 + h\nu \rightarrow (TiO_2)e^-_{(cb)} + (TiO_2)h^+_{(vb)}$$

Electrons are promoted from the valence band to the conduction band: thus the conduction band acts as a reduction zone and conversely the valence band as an oxidation zone.

Due to its possible applications, many studies have been carried out on the anatase TiO_2 nanoparticles (the phase showing the best photocatalytic performance) to understand better its electronic structure, as well as chemical and physical properties [22].

The properties of nano-sized semiconductor particles have been known to be very sensitively related to the particle size: nano-scaling of materials has opened up a new dimension exhibiting unique physical and chemical properties which correspond neither to those of atoms and molecules nor to the bulk materials, with identical chemical composition [23].

Chemical, electrical and structural properties of nano-crystalline materials are of great interest today, as it is important to obtain materials with high specific area and quantum size effects especially in the field of catalysis. With a decrease in particle size of TiO_2 to the nanometer scale, the catalytic activity is enhanced as the optical band gap is widened resulting from the quantum size effect, combined with the increased surface area [24]. Precise control of the size of semi-conducting oxide materials at the nanometric scale is of absolute importance for fine-tuning their photocatalytic properties. Unfortunately nanoparticles show a tendency to aggregate, due to their high surface area-to-volume ratio, which may impede their application [25].

Many methods have been established for the synthesis of nanoparticles of titania; among them, the sol-gel technique is one of the most frequently used methods. Usually the sol-gel derived precipitates are amorphous, and require further annealing treatment to induce the transition from amorphous to the anatase phase, generally performed at an annealing temperature higher than 300 °C [26].

Key limitations of the use of TiO_2 as a photocatalyst are the absorption of light with wavelengths lower than 400 nm (5-10 % of the total solar radiation on earth surface) and the high charge recombination rates as shown in the Figure below:

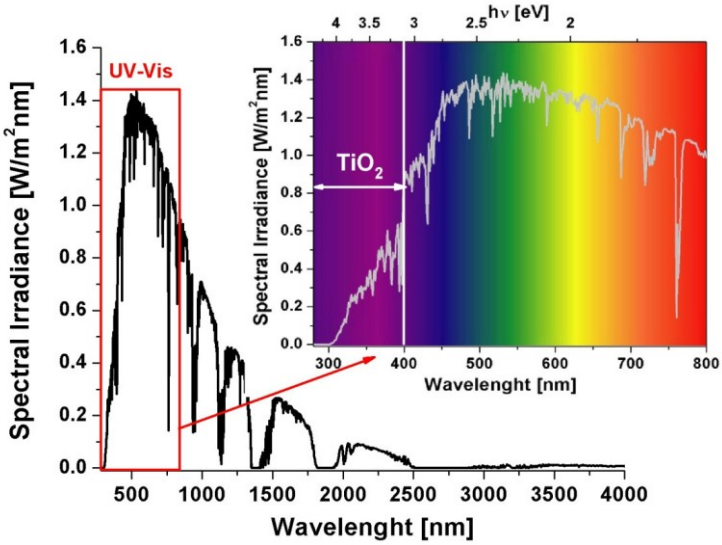

Fig. 3.5 Solar irradiance and UV-Vis range of solar spectrum with absorption range of (pure) TiO_2

A significant fraction of the solar radiation is therefore unavailable for reactions, and electron-hole recombination (e^-/h^+)

can occur before red-ox reactions take place. The advantage is that TiO_2 is practically white or colourless, enabling it to be applied as a coating without changing the appearance of the underlying materials.

In order to extend the range of photoabsorption into the visible light portion of the electro-magnetic spectrum (bathochromic shift of the band gap), doping with metals (especially transition metals ions) or non metals, into the TiO_2 crystal lattice, or loading them on the TiO_2 surface (sensitization by metal nanoparticles or organic dye sensitization) has been shown to be successful in several studies [3]. Using metal ions, doping has two main advantages: (i) reduces the band gap energy and (ii) increases the time before the electron/hole recombines. This is achieved by temporary trapping of the photogenerated charge carriers by the dopant and the inhibition of their recombination during migration from inside the material to the surface or the enhanced association of the functionalized organic pollutants with the doping ion surface sites.

The presence of these dopants in the crystalline matrix significantly influence its physical and chemical properties. The effect of metal ion doping is strongly dependent on many factors, such as the dopant concentration, the particle size of the nanocrystalline, the distribution of the dopants and the d-electronic configuration of doping ions. A decrease in the photocatalytic ability is observed when the phase transition from anatase to rutile occurs. This can be enhanced by the addition of metal ions, thus the preparation technique of the dopant is an important factor. It has

been demonstrated that the transformation rate is dependent on the conditions of doping [27]. Indeed, the way that the dopant is incorporated, and also its oxidation state, chemical environment, and distribution, could have an effect on the phase transformation. Therefore, it is important to understand the effect of the distribution and content of the dopant ions and thermal treatments on the structural properties and texture of TiO_2-based materials in order to optimize materials for a specific application.

The purpose of the present work is to synthesize TiO_2-based nanoparticles with enhanced photocatalytic activity by increasing charge separation, reducing the band gap and inhibiting the electron-hole recombination and to enhance their visible light absorption, using a sol-gel process.

Furthermore, the aim is to elaborate scientific understanding and correlations between the sol-gel process parameters, the resulting particle characteristics, and the functional properties of these particles. This dissertation is composed of theoretical and experimental sections.

The theoretical section covers a description of the basic properties of TiO_2 and its role in the photocatalytic phenomenon in the context of the application of the photocatalytic pollutants decomposition in the air and in the aqueous systems.

In the experimental section, the nanoparticles synthesis of undoped and metal ion doped TiO_2 is presented. Followed by the characterization of the basic properties such as: particle size, shape and morphology (SEM and XRD), the chemical composition and surface state (XPS, DSC-TGA), and optical properties (UV-Vis).

In the end, the verification of the photocatalytic properties is discussed (decomposition of NO_2 and Methyl Orange, MO).

Modification of TiO_2 properties

The need for the modification of the TiO_2 properties with respect to photocatalytic applications have been highlighted previously. There are large varieties in the modification methods [28]. Generally, we can distinguish bulk or surface modification. To have a better overview, the titanium dioxide based photocatalysts can be categorized in three groups:

- the first generation photocatalyst – undoped TiO_2
- the second generation photocatalyst – metal-doped TiO_2
- the third generation photocatalyst – non-metal-doped TiO_2 [3].

This is a very general and valid classification since the Fujishima and Honda's work was published in 1972 [29]. The primary purpose of any type of modification of TiO_2 is to shift the light absorption into the visible light range and to increase electrical conductivity. In addition, other features like surface acidity, crystallinity, and crystallite size have to be considered and improved in the TiO_2 based photocatalyst.

The first generation is represented by undoped TiO_2, which can be prepared with different methods, as it will be described in the next chapter.

The second generation is represented by metal doping, and can be done by:

• solid solution formation of two (or more) compounds with different band gaps which results in the decrease of E_g and shifts the light absorption towards the visible light e.g. $Ti_{1-x}V_xO_2$ [30];

• metal doping by foreign atoms can be divided into donor and acceptor types. This type of doping acts as electron/hole traps and alters the photoexcited charges recombination rate. The levels which are positioned under the CB can act as an electron trap and the one above VB can act as a hole trap. Theoretically, with increasing concentration of dopant, the concentration of extrinsic defects is increasing. It can result in the appearance of impurity levels and an increase in their density. This may lead to the transition to impurity band and can cause the narrowing of forbidden band. The introduced impurity levels can also improve light absorption in the visible range by acting as an indirect transition pathway for excited charges.

The third generation consists of the modification of the anionic sub-lattice by such elements as N [31], S [32] or C [33] which gives promising results in the improvement of the light absorption in the visible range. Nevertheless, the mechanism of the electronic structure modification is still under debate.

References

[1] D. J. Reidy, J. D. Holmes, M. A. Morris, J. Eur. Cer. Soc., 26, 2006, 1527-1534.

[2] U. Diebold, Surface Science Reports, 48, 2003, 53-229.

[3] X. Chen, S.S. Mao, Chem. Rev., 107, 2007, 2891-2959.

[4] M. Schiavello, "Heterogeneous Photocatalysis", John Wiley & Sons, vol. 3 (1997).

[5] F. Dachielle, P. Y. Simons, R. Roy, Amer. Miner., 53, 1968.

[6] J. L. Murray, H. A. Wriedt, Bulletin of Alloy Phase Diagrams, 8, 1987, 148-165.

[7] El, Goresy; Chen, M; Dubrovinsky, L; Gillet, P; Graup, G., Science, 293, 1467–70, 2001

[8] El Goresy, Ahmed; Chen, Ming; Gillet, Philippe; Dubrovinsky, Leonid; Graup, Günther; Ahuja, Rajeev, Earth and Planetary Science Letters 192, 485, 2001.

[9] J.W. MacFarlane, H.F. Jenkinson, T.B. Scott, Applied Catalysis B, 106, 2011, 181-185.

[10] M.A. Fox, M.T. Dulay, Chem. Rev., 83, 1995, 341-357.

[11] T.L. Thompson, J.T. Yates, Chem. Rev., 106, 2006, 4428-4453.

[12] A. Fujishima, X. Zhang, C. R. Chimie, 9, 2006, 750-760.

[13] N. Serpone, E. Pelizetti, "Photocatalysis: Fundamentals and Application", Wiley (1989).

[14] M. Schiavello, "Photocatalysis and Environment Trends and Applications", Kluwer Academic Publishers (1988).

[15] Gopal M., Moberly Chan WJ., De Jonghe LC. J. Mater. Sci., 32, 1997.

[16] Anpo M., Bull. Chem. Soc. Jpn., 77, 2004.

[17] Yu J.C., Yu J., Zhang L., Ho W., J. Photochem. Photobiol. A., 148, 2002.

[18] H. Alekabi, N. Serpone, J. Phys. Chem., 92, 1988.

[19] M.R. Prairie, L.R. Evans, B.M. Stange, S. L. Martinez, Environ. Sci. Technol., 27, 1993.

[20] M. Sadeghi, W. Liu, T.G. Zhang, P. Stavropoulos, B.J. Levy, Phys. Chem. 100, 1996, 19466-19474.

[21] Y. Ohko, D.A. Tryk, K. Hachimoto, A. Fujishima, T.N. Obee, J. Phys. Chem. B, 102, 1998, 2699–2704.

[22] M. Fernández-García, A. Martínez-Arias, J. C. Hanson, and J. A. Rodriguez, Chem. Rev., 2004, 104, 4063–4104.

[23] C. Altavilla, E. Ciliberto "Inorganic Nanoparticles: Synthesis, Applications, and Perspectives", CRC Press - Taylor Francis, 2010.

[24] Chung-Sik K., Il-Min K., Byung Kee M., Jung Hyun J., Byung-Chun C., Jung Hwan K., Haeyoung C., Soung Soo Y., Dae-Hwang Y., Kyong-Soo H., Jong-Ho P., Ho Sueb L., Materials Science and Engineering C, 27, 2007, 1343–1346.

[25] Xuedong W., Dapu W., Shengrong Y., Journal of Colloid and Interface Science 222, 2000, 37-40.

[26] Haimei L., Wensheng Y., Ying M., Yaan C., Jiannian Y., Jing Z., Tiandou H., Langmuir, 2003, 19.

[27] P. Baltazar, V. H. Lara, G. Cordoba, R. Arroyo, J. Sol-Gel Sci. Techn., 37, 2006.

[28] K. A. Michałów, Ph.D. Thesis, Kraków (Poland), 2009.

[29] A. Fujishima, K. Honda, Nature, 238, 1972, 37-38.

[30] G. Zhao, H. Kozuka, H. Lin, T. Yoko, Thin Solid Films, 339, 1999, 123-128.

[31] R. Asahi, T. Morikawa, T. Ohwaki, K. Aoki, Y. Taga, Science, 293, 2001, 269-271.

[32] H. Wang, J. P. Lewis, J. Phys. :Condens. Matter., 18, 2006, 421-434

[33] S. U. M. Khan, M. Al-Shahry, W. B. I. Jr., Science, 297, 2002, 2243-2245.

Nanostructure Synthetic Methods

Introduction

TiO_2 can be prepared in the form of powder, crystals or thin films. Both powders and films can be formed from crystallites ranging from a few nanometres to several micrometers. It should be noted that nanosized crystallites tend to agglomerate; a good discussion on the aggregation and agglomeration can be found in literature [1].

It is important to mention that the physical and chemical properties of TiO_2 are strongly dependent on the preparation synthesis [1]. There are several methods used to synthesize TiO_2 nanoparticles and basically, they can be divided into two different routes of preparation: gas–phase methods and solution methods.

Among gas–phase methods, the main techniques are:

- chemical vapour deposition (CVD)
- physical vapour deposition (PVD)
- spray pyrolysis deposition (SPD)

The solution methods include:

- solvothermal and hydrothermal method
- precipitation method
- microemulsion method
- combustion synthesis
- electrochemical synthesis

- sol–gel method
- micelle and inverse micelle methods
- sonochemical method
- microwave method

The sol-gel method is probably the most used one, for several advantages explained below.

Sol-gel method

The terms “sol” and “gel” are being defined as:

- a “sol” is a stable suspension of colloidal solid particles or polymers in a liquid. The particles can be amorphous or crystalline;
- a “gel” consists of a porous, three–dimensional continuous solid network surrounding and supporting a continuous liquid phase (“wet gel”). In “colloidal” (“particulate”) gels, the network is made of agglomeration of dense colloidal particles, whereas, in “polymeric” gels the particles have a polymeric sub–structure containing aggregation of sub–colloidal chemical units.

The sol-gel method is a versatile process used in the production of various ceramic materials [2-6]. In a typical sol-gel process, a colloidal suspension, or a sol, is formed from the hydrolysis and polymerization reactions of the precursors, which are usually inorganic metal salts or metal organic compounds such as metal alkoxides. Complete polymerization and loss of solvent leads

to the transition from a liquid sol into a solid gel phase. Thin films can be produced on a piece of substrate by spin-coating or dip-coating (details can be found in the next chapter). A wet gel will be formed when the sol is cast into a mould, and the wet gel is converted into a dense ceramic materials with further drying and heat treatment. Fig. 4.1 is a schematic representation of the different process routes leading from the sol to a variety of materials:

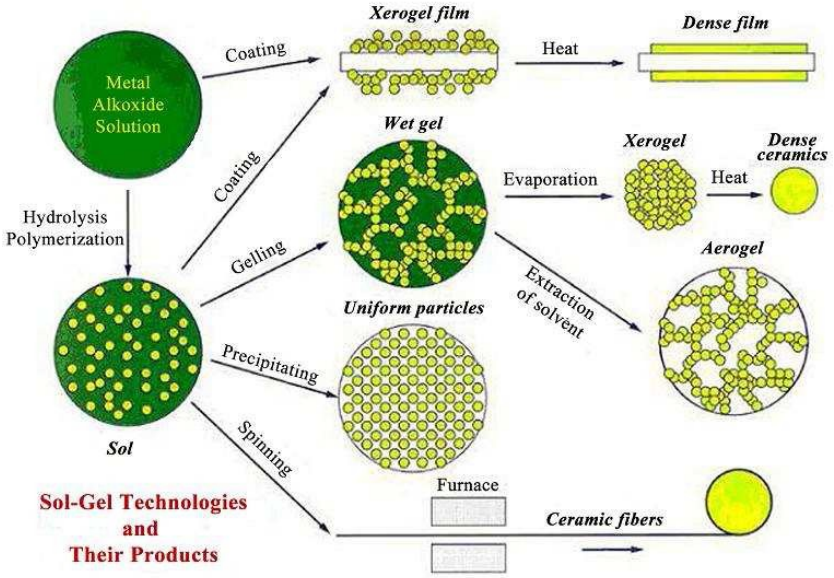

Fig. 4.1. Scheme of the sol–gel processing options [1]

A highly porous and extremely low-density material called an aerogel is obtained if the solvent in a wet gel is removed under a supercritical condition (Fig. 4.1). Ceramic fibres can be drawn from the sol when the viscosity of a sol is adjusted into an appropriate viscosity range. Ultrafine and uniform ceramic powders are formed by precipitation, spray pyrolysis or emulsion techniques. Under

certain conditions, nanomaterials can be obtained as discussed in Brinker & Scherer's book [1].

The sol-gel transformation normally proceeds via an acid-catalyzed hydrolysis step of titanium(IV) alkoxide followed by condensation [7].

The development of Ti-O-Ti chains is favoured by a low content of water, low hydrolysis rates and excess titanium alkoxide in the reaction mixture. Three dimensional polymeric skeletons with close packing result from the development of Ti-O-Ti chains. The formation of $Ti(OH)_4$ is favoured by high hydrolysis rates with a medium amount of water. The presence of a large quantity of Ti-OH and insufficient development of three-dimensional polymeric skeletons leads to loosely packed first-order particles. Polymeric Ti-O-Ti chains are developed in the presence of a large excess of water.

From the study of the growth kinetics of TiO_2 nanoparticles in aqueous solution using titanium tetraisopropoxide (TTIP) as precursor, it was found that the rate constant for coarsening increases with temperature due to the temperature dependence of the viscosity of the solution and the equilibrium solubility of TiO_2 [8]. Secondary particles are formed by epitaxial self-assembly of primary particles at longer times and higher temperatures, and the number of primary particles per secondary particle increases with time.

Highly crystalline anatase TiO_2 nanoparticles with different sizes and shapes can be obtained with the polycondensation of titanium alkoxide in the presence of tetramethylammonium

hydroxide [9, 10]. In a typical procedure, titanium alkoxide is added to the base at 2 °C in alcoholic solvents and heated at 50 - 60 °C for 13 days or at 90 - 100 °C for 6 hours. A secondary treatment involving autoclave heating at 175 °C and 200 °C is performed to improve the crystallinity of the TiO_2 nanoparticles. A series of thorough studies have been conducted by Sugimoto et al. using the sol-gel method on the formation of TiO_2 nanoparticles of different sizes and shapes by tuning the reaction parameters [11-15].

A prolonged heating time below 100 °C for the as-prepared gel can be used to avoid the agglomeration of the TiO_2 nanoparticles during the crystallization process [16, 17]. By heating amorphous TiO_2 in air, large quantities of single-phase anatase TiO_2 nanoparticles with average particle sizes between 7 and 50 nm can be obtained, as reported by Zhang and Banfield [18-22]. Much effort has been exerted to achieve highly crystallized and narrowly dispersed TiO_2 nanoparticles using the sol-gel method using other modifications.

Chemistry of sol-gel methods

Sol-gel comprises of many chemical methods, starting from a liquid solution of molecular precursors, among which the most widely adopted is certainly the alkoxides method. As this is the only method that has been used in this work, it will be the subject of this brief overview of the sol-gel chemistry. Alkoxides are molecules with general formula $M(OR)_n$, where R represents an alkyl or aryl group and M the metal whose oxide will form the matrix of

inorganic structure. Typically a starting alcoholic solution of the alkoxide is prepared, using the alkoxide corresponding alcohol as solvent. In other words if R is an ethyl or a methyl group ethanol or methanol will be used, respectively. This is the so called solution stage, and it is followed by the gelation stage, which is initiated by the addition of a certain amount of water. At this stage the precursors undergo hydrolysis and condensation reactions according to the general scheme:

Hydrolysis

$$M(OR)_n + H_2O = M(OR)_{n-1}(OH) + ROH$$

Condensation

$$M(OR)_n + M(OR)_{n-1}(OH) = (RO)_{n-1}M\text{-}O\text{-}M(OR)_{n-1} + ROH$$

$$M(OR)_{n-1}(OH) + M(OR)_{n-1}(OH) = (RO)_{n-1}M\text{-}O\text{-}M(OR)_{n-1} + H_2O$$

In our synthesis, M is titanium and R is isopropyl group.

These reactions are simultaneous and the relative kinetics of these key processes will determine the matrix structure. As the reaction proceeds, the number of -M-O-M- bonds increases (here n = 4 has been assumed), leading to a progressive decrease in network exibility and a related increase in solution viscosity.

The sol-to-gel transition has been extensively simulated and studied [1]. Full densification of the porous gels can usually be achieved by annealing, which removes residual solvent and eventually leads to sintering / crystallization.

Advantages of sol-gel methods

A number of reasons to choose the sol–gel route for the synthesis of materials are [1]:

(i) the chemical conditions are mild. Hydrolysis and condensation are catalyzed by acids and bases, but extreme pH conditions can be easily avoided, especially by the use of a two step method in which acid catalyzed hydrolysis is followed by rapid neutralization or buffering. In this way, pH sensitive organic species (e.g. dyes) and even biological species including enzymes and whole cells may be entrapped and still retain their functions.

(ii) Highly porous materials and nanocrystalline materials may be prepared in this way.

(iii) By controlling ageing and drying conditions, further pore size and mechanical strength control may be achieved. Two processing routes of the sol–gel method are known: the non–alkoxide (inorganic) and the alkoxide (organic) route. The non–alkoxide route uses inorganic salts (such as nitrates, chlorides, acetates, carbonates, acetylacetonates, etc.) and requires an additional removal of the inorganic anion, while the alkoxide route (the most usually employed) uses metal alkoxides as starting material.

All the proposed synthetic methodologies in preparing sol-gel can be traced back to three fundamental stages [1]:

- preparation of liquid solutions of suitable precursors;
- sol transformation and gel formation;
- thermal treatment of the gel.

This general and highly versatile method presents some fundamental advantages compared to the traditional glass makings including:

- most of the synthetic steps can be carried out at room conditions;
- materials composition can be easily and precisely controlled;
- homogeneous coatings on suitable substrates can be made;
- the purity of the material can be very high.

References

[1] a) Brinker C. J., Scherer G.W. Sol–gel science, Academic Press, Inc. 1990;

b) Xuedong W., Dapu W., Shengrong Y., Journal of Colloid and Interface Science 222, 2000, 37-40.

[2] Pierre, A. C.; Pajonk, G. M. Chem. Rev. 2002, 102, 4243.

[3] Lu, Z. L.; Lindner, E.; Mayer, H. A. Chem. ReV. 2002, 102, 3543.

[4] Wight, A. P.; Davis, M. E. Chem. ReV. 2002, 102, 3589.

[5] Schwarz, J. A.; Contescu, C.; Contescu, A. Chem. ReV. 1995, 95, 477.

[6] Hench, L. L.; West, J. K. Chem. ReV. 1990, 90, 33.

[7] Bessekhouad, Y.; Robert, D.; Weber, J. V. J. Photochem. Photobiol., A 2003, 157, 47.

[8] Oskam, G.; Nellore, A.; Penn, R. L.; Searson, P. C. J. Phys. Chem. B 2003, 107, 1734.

[9] Chemseddine, A.; Moritz, T. Eur. J. Inorg. Chem. 1999, 235.

[10] Moritz, T.; Reiss, J.; Diesner, K.; Su, D.; Chemseddine, A. J. Phys. Chem. B 1997, 101, 8052.

[11] Sugimoto, T.; Okada, K.; Itoh, H. J. Colloid Interface Sci. 1997, 193, 140.

[12] Sugimoto, T.; Zhou, X. J. Colloid Interface Sci. 2002, 252, 347.

[13] Sugimoto, T.; Zhou, X.; Muramatsu, A. J. Colloid Interface Sci. 2002, 252, 339.

[14] Sugimoto, T.; Zhou, X.; Muramatsu, A. J. Colloid Interface Sci. 2003, 259, 53.

[15] Sugimoto, T.; Zhou, X.; Muramatsu, A. J. Colloid Interface Sci. 2003, 259, 43.

[16] Li, Y.; White, T. J.; Lim, S. H. J. Solid State Chem. 2004, 177, 1372.

[17] Uekawa, N.; Kajiwara, J.; Kakegawa, K.; Sasaki, Y. J. Colloid Interface Sci. 2002, 250, 285.

[18] Zhang, H.; Banfield, J. F. J. Mater. Chem. 1998, 8, 2073.

[19] Zhang, H.; Banfield, J. F. J. Phys. Chem. B 2000, 104, 3481.

[20] Zhang, H.; Finnegan, M.; Banfield, J. F. Nano Lett. 2001, 1, 81.

[21] Zhang, H.; Banfield, J. F. Chem. Mater. 2002, 14, 4145.

[22] Zhang, H.; Banfield, J. F. Chem. Mater. 2005, 17, 3421.

Thin Film Deposition Methods

Introduction

Titanium dioxide can be deposited by many different techniques [1-18] such as:

- dip coating
- spin-coating
- evaporation
- sputtering
- laser ablation
- plasma anodisation
- reactive ion plating
- ion assisted deposition
- hydrolysis and pyrolysis
- metal organic chemical vapour deposition (MOCVD)
- low pressure chemical vapour deposition (LPCVD)
- plasma enhanced chemical vapour deposition (PECVD)
- atmospheric pressure chemical vapour deposition (APCVD)
- ultra-high vacuum chemical vapour deposition (UHV-CVD)

A primary consideration is that the growth morphology, crystalline structure and stoichiometry of TiO_2 thin films are very sensitive to the deposition conditions; details can be found in [19-22].

Among all these methods, the spin coating shows same advantages:

- low equipment cost;
- fast process time (only a few seconds per coating);
- high thickness homogeneity and uniformity over the surface;
- low volume operations;
- repeatability.

A disadvantage can be the lack of materials during the spin process.

Spin coating method

Once the final TiO_2 colloidal system is ready, it is possible to proceed with the subsequent deposition of the gel onto a substrate.

Spin-coating deposition is the most adopted method at both laboratory and industrial scale, providing a homogeneous coating of large surfaces with low sol-gel solution consumption. The technique itself leads to the formation, through fast rotation, of the substrate on top of which some of the sol-gel precursors solution was previously poured, and can be described as a four stage process.

The first stage is the deposition of the coating fluid onto the substrate surface. This can be achieved using a nozzle that pours the coating solution out. Usually, this dispensing stage provides a substantial excess of coating solution compared to the amount that will ultimately be required in the coating thickness. It is advisable at this stage to cover the whole substrate surface with the solution to avoid an incomplete coverage.

The second stage comprises the substrate acceleration up to its final, desired, rotation speed. This stage is usually characterized

by aggressive fluid expulsion from the substrate surface by the rotational motion. Due to the initial depth of fluid on the glass or wafer surface, spiral vortices may be briefly present during this stage, which form as a result of the twisting motion caused by the inertia that the top of the fluid layer exerts while the glass or wafer accelerates. Eventually, the fluid is thin enough to be completely co-rotating with the substrate and any evidence of fluid thickness differences is not detectable. Ultimately, the substrate reaches its desired speed and the liquid is thin enough that the viscous shear drag exactly balances the rotational accelerations. Figure 5.1 represents these initial stages.

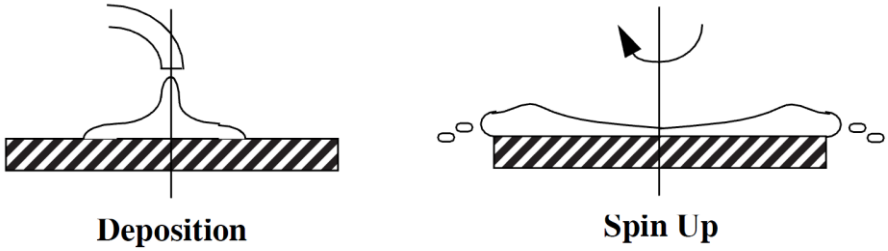

Fig 5.1 Left: stage 1 of the spin-coating process (deposition of the sol-gel solution) Right: stage 2, acceleration of the substrate with initial fast expulsion of the excess solution from the surface [23].

During the third stage, the substrate is spinning at a constant rate and the fluid viscous forces dominate fluid thinning behaviour. This stage is characterized by gradual fluid thinning. Edge effects are often seen because the fluid flows uniformly outward, and forms droplets at the edge which are then flung off. Thus, depending on the surface tension, viscosity and rotation rate, there may be a small

bead of coating thickness difference around the rim of the final substrate. Mathematical treatment of the flow behaviour shows that if the liquid exhibits Newtonian viscosity (i.e. is linear) and if the fluid thickness is initially uniform across the wafer (albeit rather thick), then the fluid thickness profile at any future point in time will also be uniform, leading to a uniform final coating (under ideal circumstances) [24].

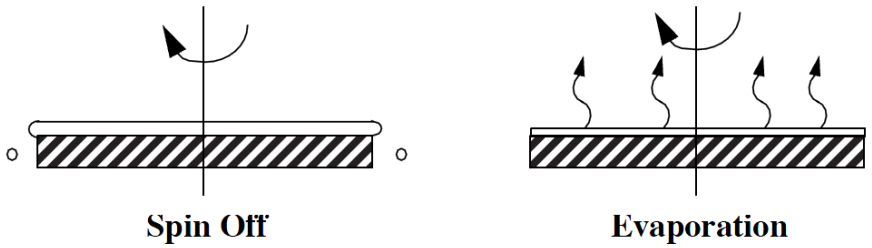

Fig 5.2 Left: stage 3 of the spin-coating process.
Right: stage 4 of the spin-coating process [23].

The fourth stage is characterized by substrate spinning at a constant rate where solvent evaporation dominates the coating thinning behaviour, as shown in Figure 5.2.

As the prior stage advances, the fluid thickness reaches a point where the viscosity effects yield only rather minor net fluid flow. At this point, the evaporation of any volatile solvent species will become the dominant process occurring in the coating. In fact, at this point the coating effectively gels because the viscosity of the

remaining solution will likely rise, eventually freezing the coating in place.

Clearly, stages 3 and 4, describe two processes that must be occurring always simultaneously (viscous flow and evaporation). However, the viscous flow effects dominate early on, while the evaporation processes dominate later.

Exceeding the viscosity or low spinning rates, may lead to less homogeneity of the resulting film, it is therefore necessary to find the optimum compromise between these parameters. Multi-layers deposition is possible, but the covered layer must be densified enough to avoid dissolution into the upper layers.

Chemical and physical interactions on the interphase between titanium dioxide and glass surface can be found in the literature [25].

References

[1] W. Badawy, F. Decker, and K. Doblhofer, Solar Energy Materials, vol. 8, pp. 363–369, 1983.

[2] Y. Takahashi, K. Tsuda, K. Sugiyama, H. Minoura, D. Makino, and M. Tsuiki, Journal of the Chemical Society: Faraday Transactions 1, vol. 77, pp. 1051–1057, 1981.

[3] S. Zhang, Y.F. Zhu, and D.E. Brodie, Thin Solid Films, vol. 213, pp. 265–270, 1992.

[4] R.W. Phillips and J.W. Dodds, Applied Optics, vol. 20, no. 1, pp. 40–47, 1981.

[5] G. Gusmano, G. Montesperelli, P. Nunziante, E. Traversa, A. Montenero, M. Braghini,

G. Mattogno, and A. Bearzotti, Journal of the Ceramic Society of Japan, vol. 101, pp. 1066–1070, 1993.

[6] W.G. Lee, S.I. Woo, J.C. Kim, S.H. Choi, and K.H. Oh, Thin Solid Films, vol. 237, pp. 105–111, 1994.

[7] C. Martinet, V. Paillard, A. Gagnaire, and J. Joseph, Journal of Non-Crystalline Solids, vol. 216, pp. 77–82, 1997.

[8] S.R. Kurtz and R.G. Gordon, Thin Solid Films, vol. 147, pp. 167–176, 1997.

[9] J-P. Lu and R. Raj, Journal of Materials Research, vol. 6, no. 9, pp. 1913–1918, 1991.

[10] T-K. Won, S-G. Yoon, and H-G. Kim, Journal of the Electrochemical Society, vol. 139, no. 11, pp. 3284–3288, 1992.

[11] J-P. Lu, J. Wang, and R. Raj, Thin Solid Films, vol. 204, pp. L13–17, 1991.

[12] W.D. Brown and W.W. Grannemann, Solid-State Electronics, vol. 21, pp. 837–846, 1978.

[13] M. Murozono, S. Kitamura, T. Ohmura, K. Kusao, and Y. Umeo, Japanese Journal of Applied Physics, vol. 21, no. Supplement 21-2, pp. 137–141, 1982.

[14] P. Lobl, M. Huppertz, and D. Mergel, Thin Solid Films, vol. 251, pp. 72–79, 1994.

[15] H. Tang, H. Berger, P.E. Schmid, and F. Levy, Solid State Communications, vol. 92, no. 3, pp. 267–271, 1994.

[16] C.R. Ottermann and K. Bange, Thin Solid Films, vol. 286, pp. 32–34, 1996.

[17] H.K. Ardakani, Thin Solid Films, vol. 248, pp. 234–239, 1994.

[18] C.R. Ottermann, K. Bange, W. Wagner, M. Laube, and F. Rauch, Surface and Interface Analysis, vol. 19, pp. 435–438, 1992.

[19] H.K. Pulker, G. Paesold, and E. Ritter, Applied Optics, vol. 15, no. 12, pp. 2986–2991, 1976.

[20] J.-S. Chen, S. Chao, J.-S. Kao, G.-R. Lai, and W.-H. Wang, Applied Optics, vol. 36, no. 19, pp. 4403–4408, 1997.

[21] M. Laube, F. Rauch, C. Ottermann, O. Anderson, and K. Bange, Nuclear Instruments and Methods in Physics Research B, vol. 113, pp. 288–292, 1996.

[22] J.M. Bennett, E. Pelletier, G. Albrand, J.P. Borgogno, B. Lazarides, C.K. Carniglia, R.A. Schmell, T.H. Allen, T. Tuttle-Hart, K.H. Guenther, and A. Saxer, Applied Optics, vol. 28, no. 15, pp. 3303–3317, 1989.

[23] Buso D., Ph.D. Thesis, Padova (Italy), 2008.

[24] D. Meyerhofer, J. App. Physics, 49, 1978, pp. 3993-3997.

[25] Ya. I. Belyi, N. A. Minakova, and A. V. Zaichuk, Glass Physics and Chemistry, 2008, Vol. 34, No. 3, pp. 282–291.

Experimental

Undoped and metal ion doped TiO_2 nanoparticles were prepared from controlled hydrolysis of titanium tetraisopropoxide. Part of the colloidal suspension was used for thin film preparation by spin coating.

After annealing, samples were characterized by an array of different experimental techniques. Measurements were recorded at room temperature except where different indications are reported.

Chemicals and materials

Chemical reagents and solvents were all of analytical grade and used without further purifications. Distilled water was used in all preparations.

As the reference photocatalyst Degussa P-25 titanium dioxide (Fluka, anatase ~ 75 % and rutile ~ 25 % with a BET surface area of 50 m^2/g corresponding to a mean particle size of ca. 25-30 nm) was used.

Corning glasses (30 x 20 x 1 mm^3) were used as substrates for TiO_2 thin film deposition.

Synthesis of nanoparticles

In a typical synthesis, 100 mL of distilled water (adjusted at pH = 2 with nitric acid, Baker, 65 %, d = 1,40 g/mL) was added dropwise to 2 mL of titanium tetraisopropoxide $Ti(iPr)_4$ (Sigma

Aldrich, ≥ 98 %, d = 0,96 g/mL) dissolved in 20 mL of 2-propanol (Lab-Scan, ≥ 99,7 %, d = 0,78 g/mL), and the reaction was kept under vigorous magnetic stirring and heating at 80 °C for 6 hours (Fig. 6.1):

Fig. 6.1 Synthesis reactor

Hydrolysis of the titanium precursor occurred immediately, as indicated by the appearance of white turbidity, and the results is a transparent translucent /milky-white colloidal system with a TiO_2 concentration of about 5 g • L^{-1} (stable for several days at room temperature, without coagulation), as shown in Fig. 6.2:

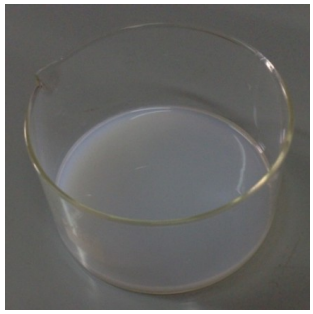

Fig. 6.2 Undoped TiO_2 colloidal system

The total chemical reaction can be described as:

$$Ti[OCH(CH_3)_2]_4 + 2H_2O \rightarrow TiO_2 + 4(CH_3)_2CHOH$$

The colloidal solution was then dried using a rotary evaporator (Figure 6.3).

Fig. 6.3 Rotary evaporator

This led to the formation of a white powder (Fig. 6.4). Finally samples were annealed at 300 °C, 550 °C and 800 °C for 3 hours (in N_2 atmosphere) for further characterizations.

Fig. 6.4 TiO_2 annealed undoped sample

Metal ion doped TiO_2 nanoparticles were prepared using a

modified version procedure described above. An appropriate amount of pure metal salts ($FeCl_3$, $FeSO_4 \cdot 7H_2O$, $Cu(NO_3)_2 \cdot 3H_2O$, $CoCl_2 \cdot 6H_2O$), was added to the acidic distilled water in order to obtain a doping level of 1,0 at. % (nominal atomic concentration, based upon the assumption of a quantitative incorporation of the dopants).

Doped TiO_2 colloidal solutions and powders showed the following different colours (Fig. 6.5), depending on the dopant metal ions:

- $FeCl_3$: dark yellowish;
- $FeCl_3 + FeSO_4 \cdot 7H_2O$: pale yellowish;
- $Cu(NO_3)_2 \cdot 3H_2O$: pale green;
- $CoCl_2 \cdot 6H_2O$: between dark pink and brown.

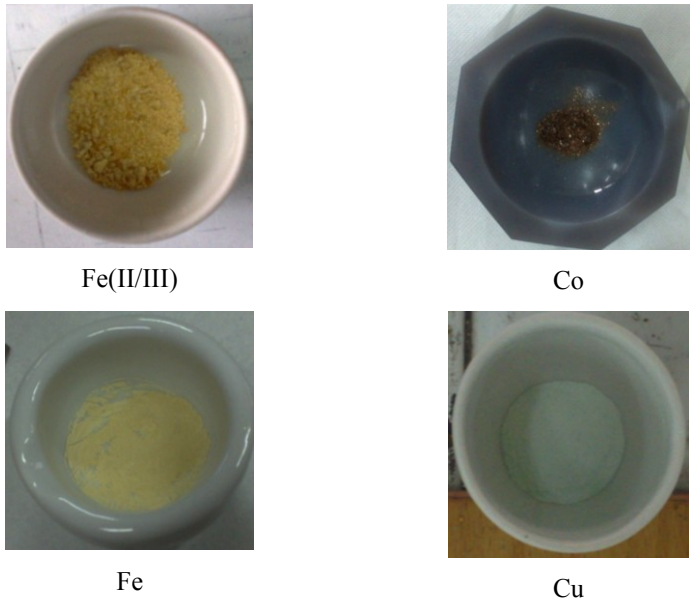

Fig. 6.5 TiO_2 annealed doped samples

Some comparisons between our samples and Degussa P25 TiO_2 have been carried out.

For convenience, samples are indicated as shown in Table 6.1:

Table 6.1 Sample abbreviation list

Metal Ion	Nominal Atomic Concentration	Annealing Temperature	Abbreviation
-	-	-	Degussa P25
-	-	550 °C	TiO_2 550
Fe^{3+}	1,0	550 °C	Fe TiO_2 550
Fe^{2+} / Fe^{3+}	1,0 (0,5 both)	550 °C	Fe(II/III) TiO_2 550
Cu^{2+}	1,0	550 °C	Cu TiO_2 550
Co^{2+}	1,0	550 °C	Co TiO_2 550
Fe^{3+}	1,0	800 °C	Fe TiO_2 800

Thermal analysis

The temperature dependent properties of the materials were investigated by thermal analyses in order to identify decomposition and crystallization temperatures, thermal stability, and phase transformations of the starting dry gels. Thermogravimetric (TG) and differential scanning calorimetry (DSC) of non-annealed sample (powder from rotary evaporator) were simultaneously performed on a LabSys Setaram thermobalance (Fig. 6.6) operating in the range of 20 – 1000 °C, with a heating scanning rate of 10 °C • min^{-1} and a N_2 flow rate of 100 mL • min^{-1}. Experiments were carried out in an alumina crucible.

Fig. 6.6 LabSys Setaram thermobalance

XRD

XRD analyses was used to characterize crystal phase structure and particle size.

X-ray powder diffraction patterns of annealed samples from thermal analysis were collected at room temperature using a Bruker-AXS D5005 diffractometer (Fig. 6.7), in the 2θ range between 20 and 70°, with Bragg-Brentano parafocusing geometry equipped with a Ni-filtered Cu Kα radiation (1.542 Å), using a 2θ scan rate of 1.5°/min. The average crystallite size, D, of the prepared powders was calculated from the Scherrer's equation, assuming spherical the shape of the particles and no crystal distortion in the lattice.

Fig. 6.7 Bruker-AXS D5005 diffractometer

SEM

Scanning electron microscopy (SEM) was used to investigate the shape, the dimensions, and the chemical composition of nanoparticles.

SEM images were recorded directly on annealed samples and energy dispersive spectroscopy (EDX) was performed to obtain quantitative information on the amount and distribution of the metal species in the samples (Supra 55 VP, combined with the improved Gemini column, Carl Zeiss and equipped with an Oxford Instruments EDX analyzer; Fig. 6.8). High resolution images were obtained using a FEI Helios Dualbeam 600i system equipped with a Elstar in-lens SE detector (TLD-SE).

Fig. 6.8 Scanning electron microscope

DLS

Dynamic Light Scattering (DLS) was used to determine the sizes and their distribution profile of TiO_2 nanoparticles in an aqueous suspension, under the same conditions used in aqueous photocatalytic tests.

Measurements were carried out using a LB-550 Horiba Size Analyzer equipped with a laser diode at 650 nm (Fig. 6.9), with an angle of 90°.

Fig. 6.9 Horiba Size Analyzer

XPS

Chemical composition and oxidation states of the surface elements in undoped and doped TiO_2 samples on the surface were evaluated by X-ray photoelectron spectroscopy (XPS), using a PHI 5600 instrument (Physical Electronics, Inc.), equipped with a monochromatic Al Kα (1486.6 eV) X-ray source (Fig. 6.10). The final pressure of 10^{-10} Torr was always attained during XPS recording. Photoelectrons were collected at 45° take-off-angle and analyzed by a concentric hemispherical analyzer. All the spectra were calibrated with respect to the binding energy of adventitious C 1s peak at 285.00 eV.

Fig. 6.10 PHI 5600 spectrometer

UV-Vis spectrophotometry

Ultraviolet-visible spectrophotometry (UV-Vis) refers to reflectance spectroscopy in the ultraviolet-visible spectral region. The reflectance in the visible range directly affects the perceived colour of the chemicals involved. Optical absorption spectra

(reflectance spectra) of the powders in the UV-Vis region (spectral range of 300-800 nm) were recorded at room temperature using a Varian Cary 500 UV-Vis-NIR spectrophotometer (Fig. 6.11) with an integration sphere.

Fig. 6.11 Varian Cary 500 spectrophotometer

Raman spectroscopy

Complementary studies of nanopowder crystallinity were evaluated by the Raman technique. Raman analysis was performed on a Renishaw System 2000 spectrometer imaging Raman microscope (Fig. 6.12), fitted with a 20 mW He-Ne laser excitation source with an excitation line at 632.8 nm at the resolution of 2 cm^{-1}.

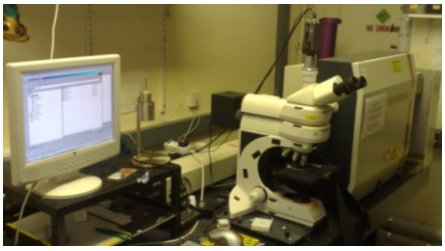

Fig. 6.12 Renishaw System 2000 spectrometer

Deposition of TiO_2 nanoparticles on corning glasses

Before deposition by spin coating, 30 x 20 x 1 mm^3 corning glasses (Fig. 6.13) were cleaned and degreased ultrasonically by immerging them into pure 2-propanol for 15 minutes at 50 °C, then washed with acetone and dried in the air at 120° C for 10 minutes.

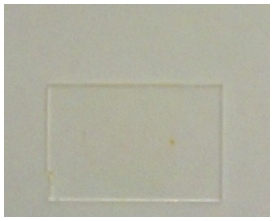

Fig. 6.13 30 x 20 x 1 mm^3 single corning glass

The concentration of TiO_2 suspensions required for the coating solution was adjusted to 0.5 g of TiO_2 / 30 mL by evaporating the solvent, as shown in Fig. 6.14.

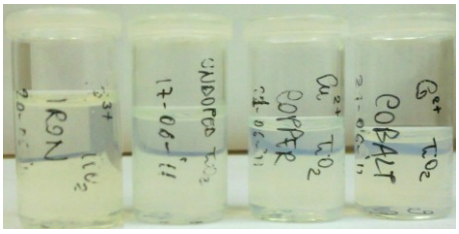

Fig. 6.14 Undoped and doped TiO_2 suspensions for coating

Cleaned glass substrates were coated by the spin-coating method (SCS G3 P-8 Spin Coater, Specialty Coating Systems Inc.; Fig. 6.15) with a spin speed of 3000 rpm for 60 seconds and evaporated at room temperature; deposition of thin films was

repeated twice in order to obtain uniform thickness of TiO_2 the glass surfaces.

Fig. 6.15 SCS G3 P-8 Spin Coater

Glasses were then heated/dried in the air at 120 °C (rate: 2 °C/min) for 60 minutes, and finally, dried samples were annealed in air at 300 °C for 1 hour (rate: 6 °C/min) to obtain the anatase structure and to remove water and some residual organics (Fig. 6.16).

Fig. 6.16 Annealed thin film samples

Optical properties of thin films

Reflectance and transmittance of coated films were measured with a an UV–Vis diode array spectrophotometer equipped with an optical fibre and deuterium and halogen lamps (QE65000 Ocean Optics, Inc.) in the range of 300-900 nm. Same instrumentation was used to calculate band gap energies of undoped and doped samples.

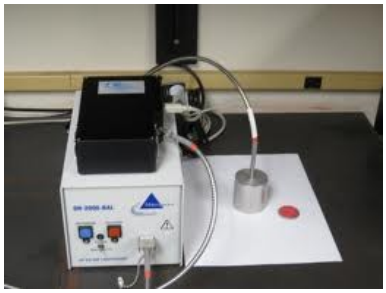

Fig. 6.17 QE65000 Ocean Optics spectrophotometer

Thickness and roughness of the films were determined with a optical profilometer (Taylor Hobson Talysurf CCI; Fig. 6.18). An optical profilometer is a measuring instrument (non-contact method) used to observe the surface's profile, in order to quantify its roughness, with a resolution of nanometre level.

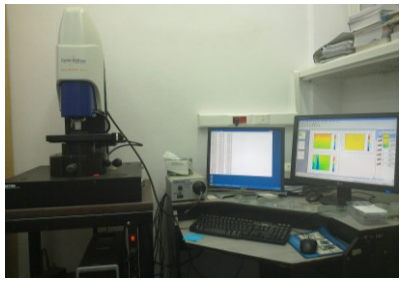

Fig. 6.18 Taylor Hobson Talysurf CCI optical profilometer

Results and Discussion

Generally speaking, in the visible range, doped samples show higher absorption than the undoped TiO_2 (Figure 7.1):

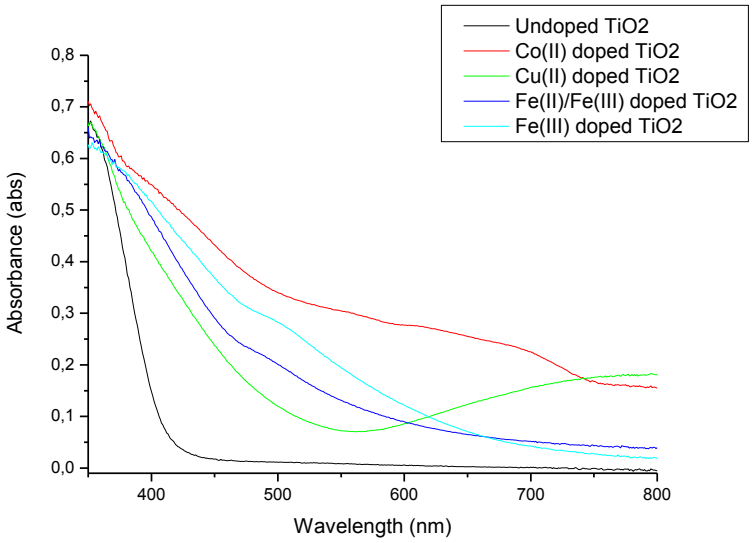

Fig. 7.1 UV-Vis absorbance comparison between undoped and doped TiO_2

The presence of doping ions in the titania structure causes a significant red shift from the near UV region (where bands are centred) into the visible region. Moreover, along the doped samples more complex spectral structures in the visible region are clearly shown, due to both d-d and CT transitions. This behaviour is then responsible for the colour of the doped titania (Fig. 6.5).

Thermal analysis

The melting temperature of a bulk material is independent of the size, however, as the dimensions of a material decrease towards the atomic scale, the melting temperature scales with the material dimensions. The decrease in melting point can be on the order of tens to hundreds of degrees for materials with nanometer dimensions; melting point depression is most evident in nanowires, nanotubes and nanoparticles [1-3]. Changes in melting point occur because nanoscale materials have a much larger surface to volume ratio than bulk materials, drastically altering their thermodynamic and thermal properties: thus the phase transition temperature onset is different due to small size of nanoparticles. Moreover, it is well known that the thermal behaviour of TiO_2 gels depends on their chemical composition and their preparation method and conditions [4].

Figures 7.2-7.6 show the results of thermogravimetric (TG) and differential scanning calorimetry (DSC) of the amorphous nanoparticle gel of undoped and metal ion doped TiO_2 in the range of 20 – 1.000 °C:

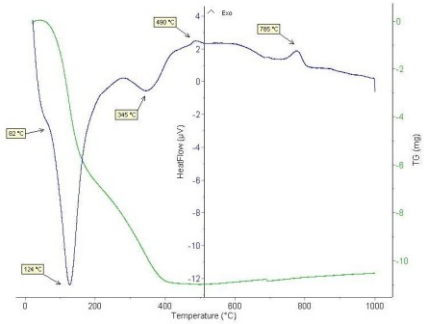

Fig. 7.2 Undoped TiO_2 thermal diagram

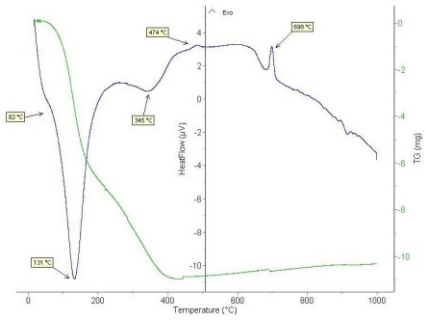

Fig. 7.3 Cu doped TiO_2 thermal diagram

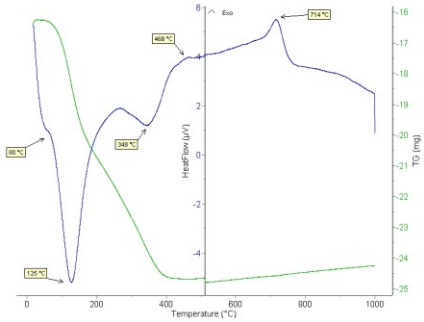

Fig. 7.4 Co doped TiO_2 thermal diagram

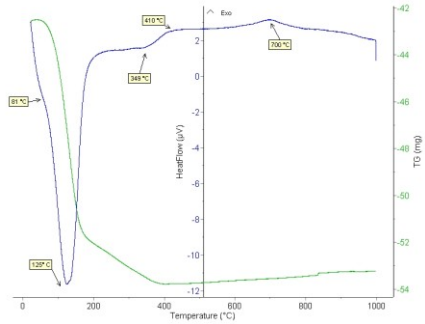

Fig.7.5 Fe^{3+} doped TiO_2 thermal diagram

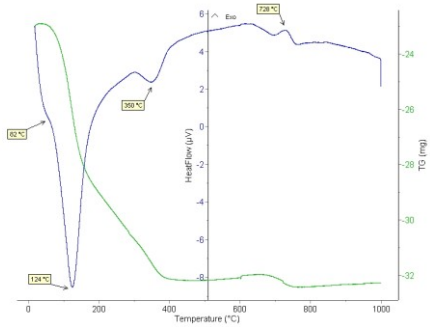

Fig. 7.6 Fe(II/III) doped TiO_2 thermal diagram

Temperatures and numerical results of total weight loss percentage values (16-20 %) are summarized in Table 7.1.

The TG-DSC profiles of TiO_2 gels exhibit different steps (Figures 7.2-7.6).

1) The first endothermic peak (between 80 and 82 °C) is believed to be associated to physical desorption and evaporation of solvent molecules (the boiling point of 2-propanol is 81 °C).

2) The second, an endothermic peak centred at about 125 °C (124-131 °C), corresponds to the loss of adsorbed water (dehydration during the heat treatment).

3) The third endothermic peak centred at about 350 °C (345-350 °C) is associated with the removal of structural hydroxyls, which further promote self-condensation among hydroxytitanate number of bridging oxygen.

4) A clear exothermic peak can be seen at around 460 °C (450-474 °C): it can be reasonably associated with the crystallization process from amorphous TiO_2 to anatase. In the undoped TiO_2 samples, phase transition temperature is higher (490 °C) than doped samples (i.e. 474 °C for copper doped sample): dopants decrease phase transition temperature onset.

5) the exothermic peak seen at 785 °C for undoped samples can be explained as occurring due to the transformation of anatase phase into rutile phase, which is shifted to lower temperature in the case of doped samples (from 698 °C to 728 °C).

It may be noticed that undoped rutile has been reported to begin to form at temperature higher than 700 °C, being the dominant

phase at 800 °C, even if some authors have reported different data [4, 5]. In fact, the anatase to rutile transformation (An-Ru) is known to be affected by crystalline size, dopant type and concentration, as well as the titanium precursor used in the chemical synthesis [4]. Suzuki and Kotera [5] reported that pure micro crystals of TiO_2 transform from anatase to rutile at the temperatures above 750 °C, whereas Cordoba et al. [6] found that in manganese doped nano TiO_2, the phase transformation temperature starts from 650 °C. Heald and Weiss [7] reported that rutile TiO_2 began to form at 900 °C and was the dominant phase at 1000 °C.

In the case of our doped samples, the An-Ru transformation starts at relatively low temperature (from 698 to 728 °C), which further supports our conclusion of doping effects on the lower onset of An-Ru transformation temperature.

In the Table 7.1 a summary of the TG/DSC data is reported for all the synthesized samples.

Table 7.1 Thermal analysis data

Sample	% weight loss	T_1 (°C)	T_2 (°C)	T_3 (°C)	T_4 (°C)	T_5 (°C)
Undoped TiO_2	16,30	82	124	345	490	785
Co^{2+} TiO_2	20,01	80	125	348	468	714
Cu^{2+} TiO_2	18,05	82	131	345	474	698
Fe^{2+} Fe^{3+} TiO_2	19,45	82	124	350	454	728
Fe^{3+} TiO_2	17,96	81	125	349	450	700

XRD

X-ray diffraction analysis was used to identify the crystal phases and to determine the crystallite size by the Scherrer's formula. X-ray diffraction analysis showed the presence of anatase and a very small quantity of rutile in samples annealed at 550 °C (Figure 7.7), while TiO_2 annealed at 800 °C for 3 hours totally transformed into rutile (Figure 7.8).

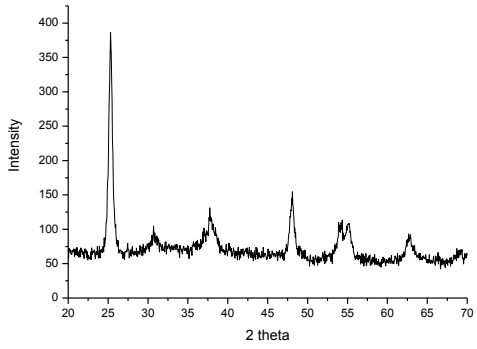

Figure 7.7 XRD pattern of TiO_2 550 (anatase)

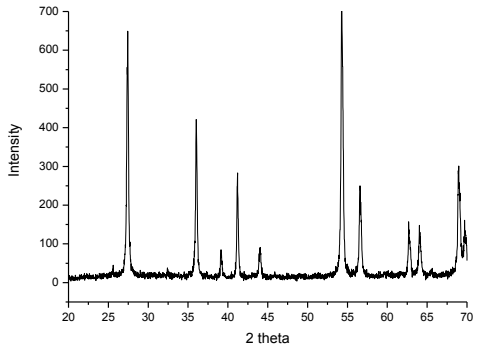

Figure 7.8 XRD pattern of Fe TiO_2 800 (rutile)

The strongest peak at $2\theta = 25.3°$ was assigned to (101) lattice plane of TiO_2 in the anatase form; other anatase characteristic peaks are present at $2\theta = 37.7°$ (004) and $2\theta = 47.9°$ (200).

The strongest peak at $2\theta = 27.4°$ was assigned to (110) lattice plane of TiO_2 in the rutile form; other rutile characteristic peaks are present at $2\theta = 36.1°$ (101) and $2\theta = 54.3°$ (211).

The crystallite nanoparticles size were calculated by the Scherrer's formula:

$$D = K \lambda / (\beta \cos \theta)$$

Where:

D = diameter of nanoparticles (in Å);

K = Scherrer's constant (~ 0.89);

λ = source wavelength (in Å);

β = peak FWHM (full-width at half-maximum in degrees, after subtraction of equipment line broadening);

θ = peak Position (in degrees).

Note that $\beta = b - â$, where b is the experimental FWHM and â is the instrumental broadening (0.06° in our case).

We found for all our samples a size range of 20 – 45 nm, in good agreement with those obtained by SEM images and DLS measurements, as reported in Table 7.2:

Table 7.2 Summary of nanoparticle sizes

Sample	Average diameter size from XRD (nm)	Average diameter size from SEM (nm)	Average diameter size from DLS (nm)
TiO_2 550	31	30	35
Fe TiO_2 550	24	23	29
Fe(II/III) TiO_2 550	23	27	31
Cu TiO_2 550	30	31	36
Co TiO_2 550	31	33	39

According to Kallen et al. [8], the ionic radius, the amount of dopant and the calcination temperature are the most important parameters which strongly affect the ability of the dopant to enter into the TiO_2 crystal lattice to form a stable solid solution. If the ionic radius of the dopant significantly differs from that of Ti^{4+} (0.64 Å), the dopant substitution will result in a crystal lattice distortion (CLD).

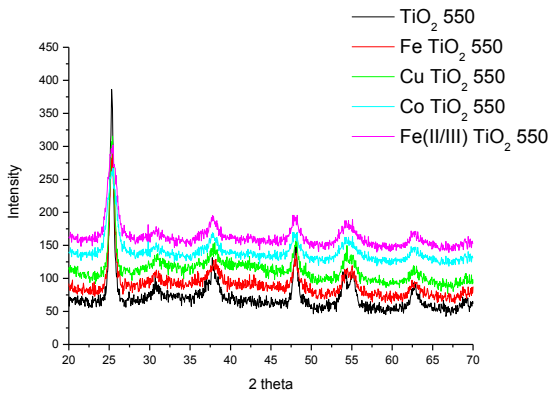

Figure 7.9 Comparison of all XRD patterns

The diffraction patterns of the doped powders were almost

coincident with the undoped TiO_2 sample. Figure 7.9 shows that the XRD peaks of pure, doped and co-doped TiO_2 nanoparticles have no shifts, suggesting no strain on the TiO_2 crystal lattice due to the presence of the dopant: in our samples doping do not affect the crystalline phase.

Raman spectroscopy

Raman spectroscopy a non-destructive spectroscopic technique used to study vibrational, rotational, and other low-frequency modes. The shift in energy provides information about the vibrational modes in the system. It is was used to confirm the crystal phase of the engineered materials. The characteristic titanium dioxide peaks in Raman spectra depend on the crystallization and phase content. In powders annealed at low temperature (550 °C), anatase was found to be the dominate phase (Figure 7.10), while samples treated at 800 °C showed only rutile structure (Figure 7.11):

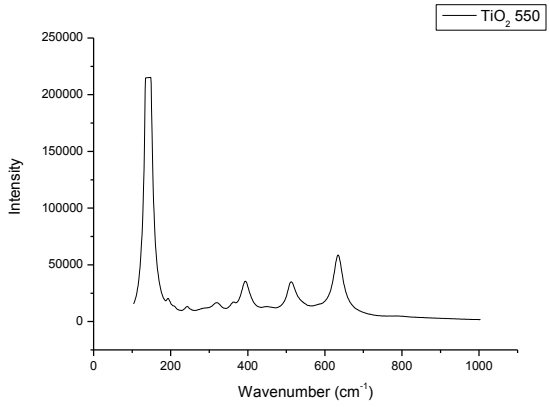

Figure 7.10 Raman spectrum of TiO_2 550 (anatase)

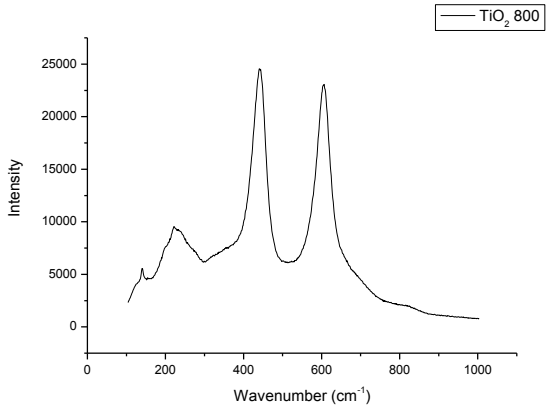

Figure 7.11 Raman spectrum of TiO_2 800 (rutile)

Raman-active fundamental modes of anatase appear at 141.1 cm^{-1} (E_g) and 392.6 cm^{-1} (B_{1g}), which correspond to O–Ti–O bending type vibrations, 513.2 cm^{-1} (doublet of A_{1g} and B_{1g}) and 633.8 cm^{-1} (E_g), that are related to Ti–O stretching type vibrations. Three Raman-active fundamental modes of the rutile polymorphic modification of TiO_2 appear at 222.1 cm^{-1} (O–Ti–O bending type vibrations), 441.5 cm^{-1} (E_g) and 606.8 cm^{-1} (A_{1g}) (Ti–O stretching type vibrations).

Raman investigation proved identical structures for undoped and doped anatase samples (Fig. 7.12):

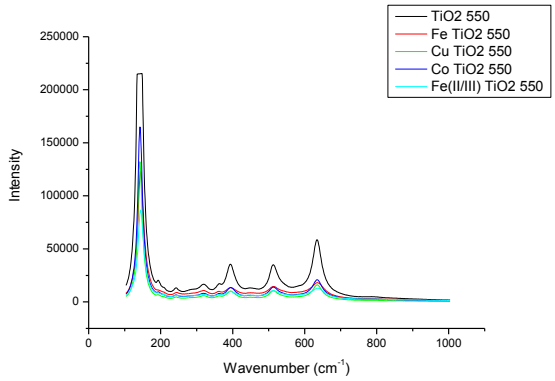

Figure 7.12 Spectra comparison of different TiO_2 550 (anatase)

SEM

Figures 7.13-7.17 show typical scanning electron images of undoped and metal ion doped TiO_2 nanoparticles calcinated at 550 °C for 3 hours. Results indicate that the mean dimensions of pure TiO_2 particles are in the range of 30-40 nm (Figure 7.13), while in the case of doped systems the range seems to be shifted to lower values, around 20-30 nm (Figures 7.14-7.17). Moreover, high magnification images obtained for the all the doped samples indicate an aggregation of sub-nanoparticles, whose size is only few nanometres, resulting in the formation of the particles constituting the materials (particles appeared as aggregates with irregular shapes and sizes).

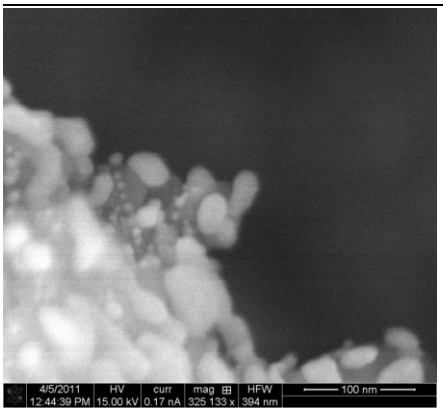

Fig. 7.13 TiO_2 550 SEM image

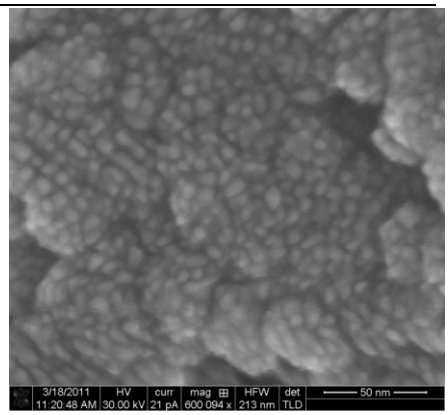

Fig. 7.14 Fe TiO_2 550 SEM image

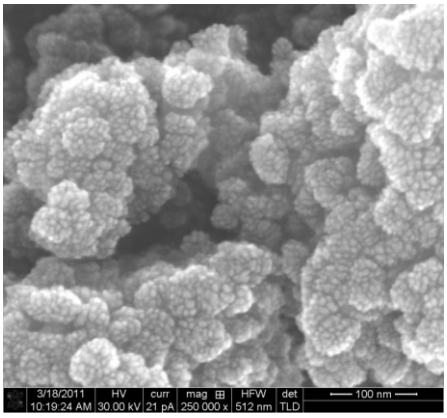

Fig. 7.15 Cu TiO_2 550 SEM image

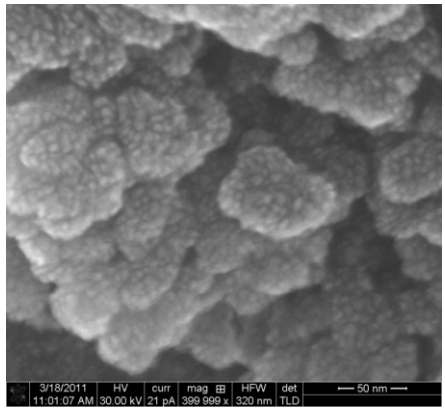

Fig. 7.16 Co TiO_2 550 SEM image

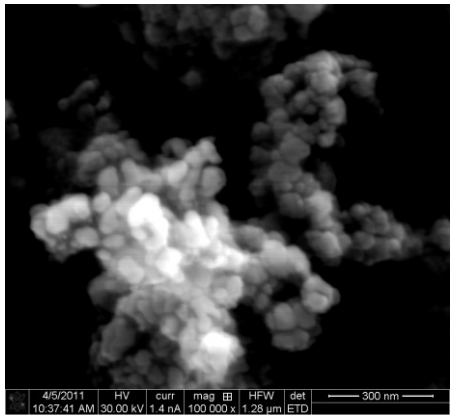

Fig. 7.17 Fe(II/III) TiO_2 550 SEM image

Because of the lower dimensions of the nanoparticles in the case of doped systems, doping ions seem to have an active effect in reducing the nanoparticle aggregation (doping probably inhibits the growth of TiO_2 nanoparticle size). Examination of doped samples reveals a homogenous microstructure in shape and size. Rutile nanoparticles are larger than anatase, and they tend to aggregate as shown in Fig. 7.18 and Fig. 7.19:

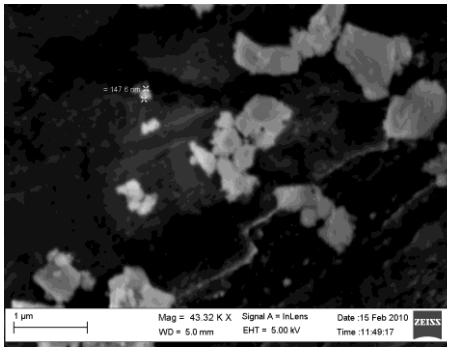

Fig. 7.18 TiO_2 800 SEM image

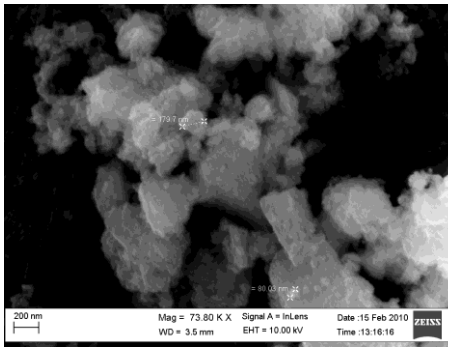

Fig. 7.19 Fe TiO_2 800 SEM image

Sizes of TiO_2 nanoparticles in the colloidal suspensions were measured also by DLS technique, and their values are in good agreement with those obtained with other experimental techniques, as reported in Table 7.2; their percentage distribution in sizes are shown in Figure 7.20:

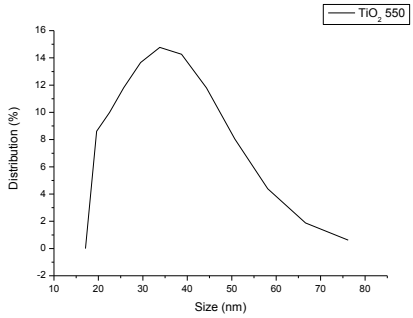

Figure 7.20 Distribution size of TiO_2 550

Higher DLS size values probably indicate an aggregation of titania nanoparticles in aqueous systems (see Table 7.2).

The presence of doping metal ions in our samples were also detected by EDX, as shown in Figures 7.21-7.25:

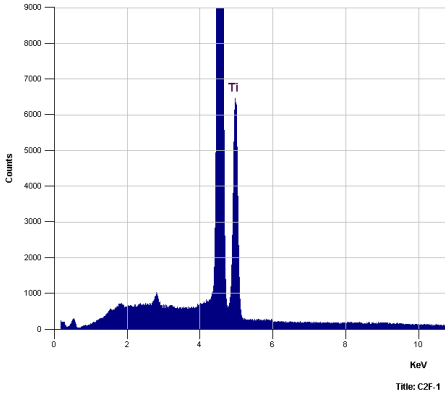

Fig. 7.21 TiO_2 550 EDX spectrum

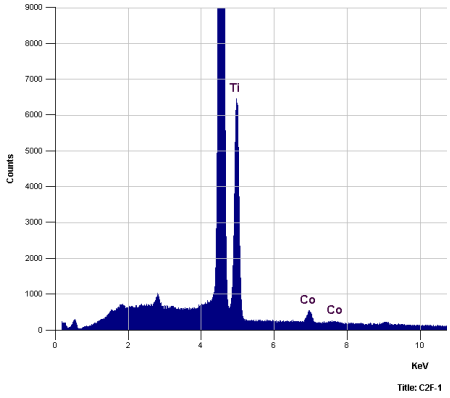

Fig. 7.22 Co TiO_2 550 EDX spectrum

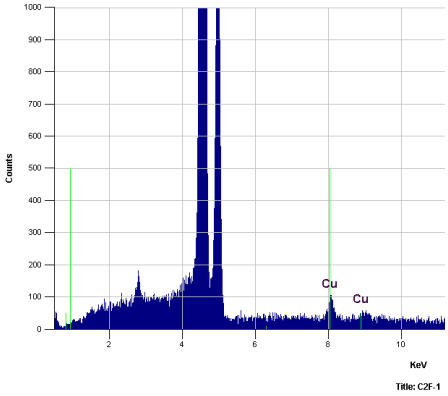

Fig. 7.23 Cu TiO_2 550 EDX spectrum

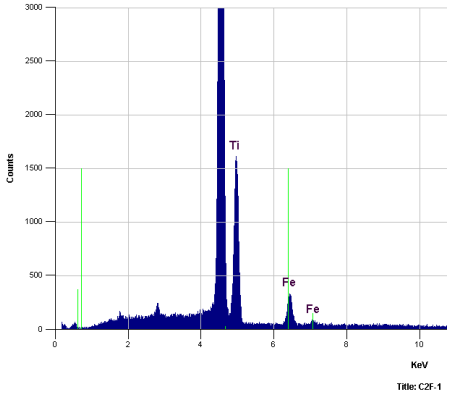

Fig. 7.24 Fe TiO_2 550 EDX spectrum

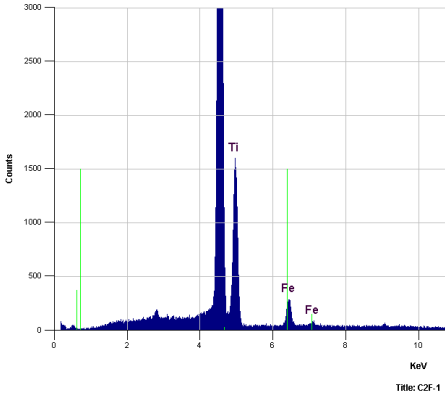

Fig. 7.25 Fe (II/III) TiO_2 550 EDX spectrum

Quantitative results are reported in Table 7.3.

XPS

XPS spectra were run for both undoped and doped titania nanoparticles. In the case of undoped TiO_2, the signals arising from carbon, titanium, and oxygen were clearly detected (Figure 7.26):

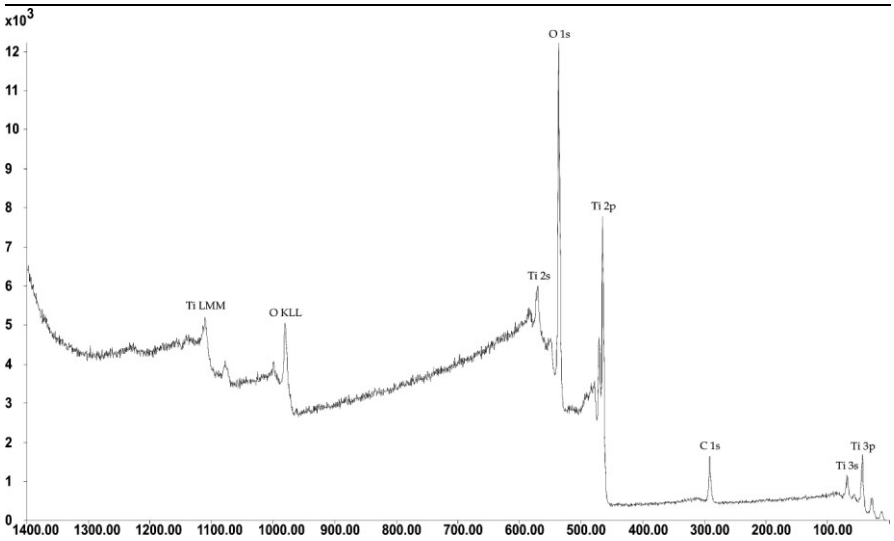

Figure 7.26 XPS survey of TiO_2 550

The carbon 1s ionization signals, shown in the Figure 7.27, are split into two components:

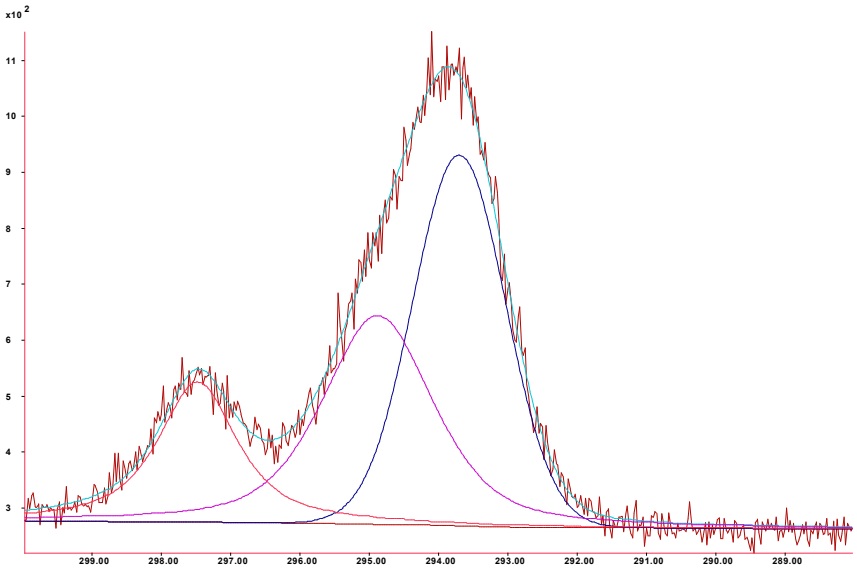

Figure 7.27 XPS carbon peak of TiO_2 550

the ionization centred at 285.00 eV is related to the adventitious carbon and also to the thermal decomposition of the organic impurities, during the "firing" process; the ionization at 288.78 eV, even low in intensity, can be attributed to carbonate species at the nanoparticles surface showing a reactivity of the nanoparticles towards the atmospheric CO_2. A shoulder centred at 286.18 eV is related to an intermediate ionization state of the carbon.

In the case of titanium 2p ionizations (Figure 7.28), the binding energy (BE) values of the two bands are in good accordance with the values reported in literature [9, 10]. Also the separation between the $2p_{3/2}$ and $2p_{1/2}$ components (5.70 eV) agrees with reported data.

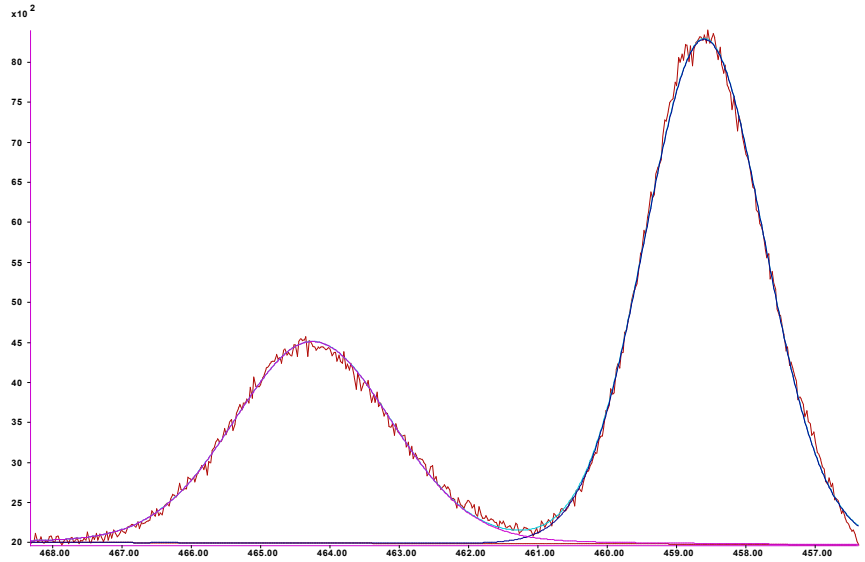

Fig. 7.28 XPS titanium peaks of TiO_2 550

The oxygen band, reported in the Figure 7.29, related to the 1s ionization, shows a complex structure. The most intense signal, centred at 530.38 eV is related to the bridging oxygen atoms constituting the lattice network of the anatase; the signals lying at higher BEs (531.30 and 532.43 eV respectively) could be attributed to -OH and H_2O species indicating that surface of nanoparticles is partially hydroxylated and hydrated. This observation is confirmed in all our samples by the atomic concentration ratio between oxygen and titanium: the ratio is about 2.2, greater than the theoretical value of 2.0.

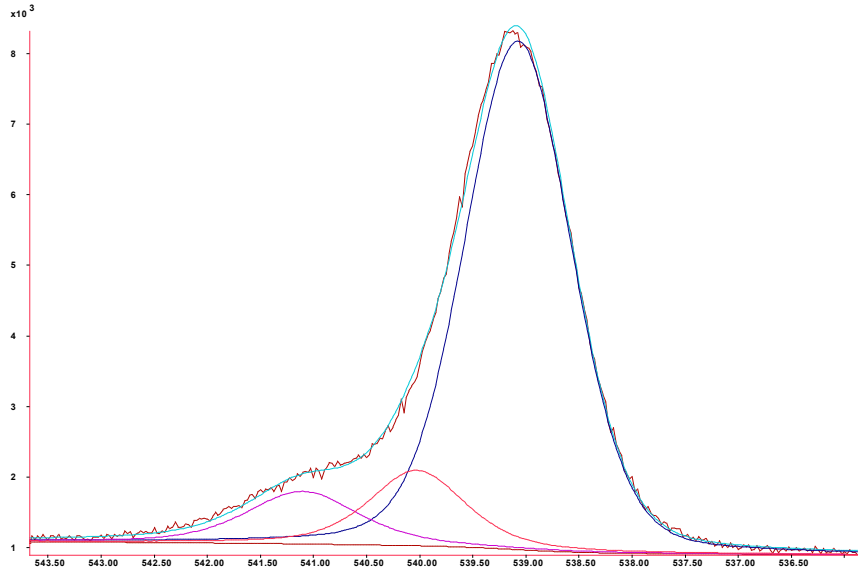

Fig. 7.29 XPS oxygen peak of TiO_2 550

In the case of doped titania, the atomic percentages of metal ions, calculated from XPS data and shown in the Table 7.3, are greater than the nominal one (1.0 %). This is probably due to a

possible enrichment of doping metal ions on the nanoparticle surface. More accurate results were obtained from EDX analysis, as shown in Table 7.3:

Table 7.3 Dopant metal ion concentrations

Atomic concentration from:	TiO_2 550	Co TiO_2 550	Fe TiO_2 550	Fe(II/III) TiO_2 550	Cu TiO_2 550
EDX	-	1.2	2.6	2.7	1.1
XPS	-	1.9	3.5	3.6	1.7

In the case of Co(II) doped titania, the core-level lines Co 2p can clearly be seen; Figure 7.30 shows the XPS spectrum in the binding energy region between 775 and 805 eV.

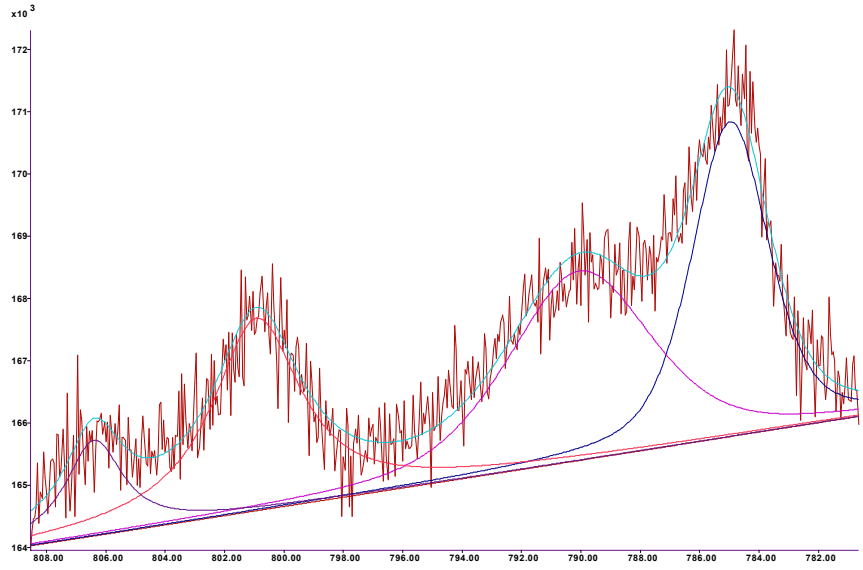

Fig. 7.30 XPS cobalt peaks of Co TiO_2 550

The peaks at binding energies 781.00 eV and 797.05 eV are attributed to spin–orbit splitting of the Co 2p photoelectron lines. In our samples, a strong satellite structure at 5.23 eV on the higher binding energy side of the main peaks was also observed.

Studies have previously been carried out on a number of cobalt complexes and compounds [11-13]. In all these studies, the analysis of Co 2p X-ray photoelectron spectra was made difficult by the fact that cobalt can exist in different coordination geometries and different spin states for the same oxidation state. Intense satellite structures were observed for Co 2p spectra, about 5–6 eV above the Co $2p_{1/2}$ and Co $2p_{3/2}$ transitions in the case of high-spin Co^{2+} (S = 3/2) compounds, whereas these satellites were seen to be very weak and located about 10 eV above the core-level lines for compounds containing low-spin diamagnetic Co^{3+} (S = 0) [14]. The satellite intensities were greater in the high-spin Co^{2+} (S = 3/2) than in the low-spin Co^{2+} (S = 1/2). This effect was investigated by Briggs and Gibson who reported the binding energy values of various cobalt complexes, and observed that the Co $2p_{1/2}$ – Co $2p_{3/2}$ spin–orbit splitting increases with the number of unpaired electrons. This increase in the $2p_{1/2}$ – $2p_{3/2}$ separation was also observed in nickel(II) complexes [11]. Multiplet splitting in the core level electron binding energy (BE) of paramagnetic species such as Co(II) is, in fact, characteristic of atoms with unpaired orbital spin density where inter-shell exchange interactions operate within the ionic state [15]. In cobalt complexes the $2p_{1/2}$ – $2p_{3/2}$ separation was found to be 15.0 eV for diamagnetic Co^{3+}, 15.4 eV for low-spin Co^{2+}, and 16.0 eV for high-spin Co^{2+} [13, 14]. These studies make possible to

determine the coordination geometry of cobalt as well as the oxidation state and the spin state with great efficiency [15]. In the case of our Co(II) doped titania, the strong intensity of satellite structures as well as the value of 16.05 eV of the spin orbit coupling between the $2p_{3/2}$ and $2p_{1/2}$ bands, strongly suggest that the cobalt (II) is in high spin configuration.

In the cases of copper and iron doped nanoparticles (Figures 7.31-7.33), XPS spectra didn't give similar interesting results.

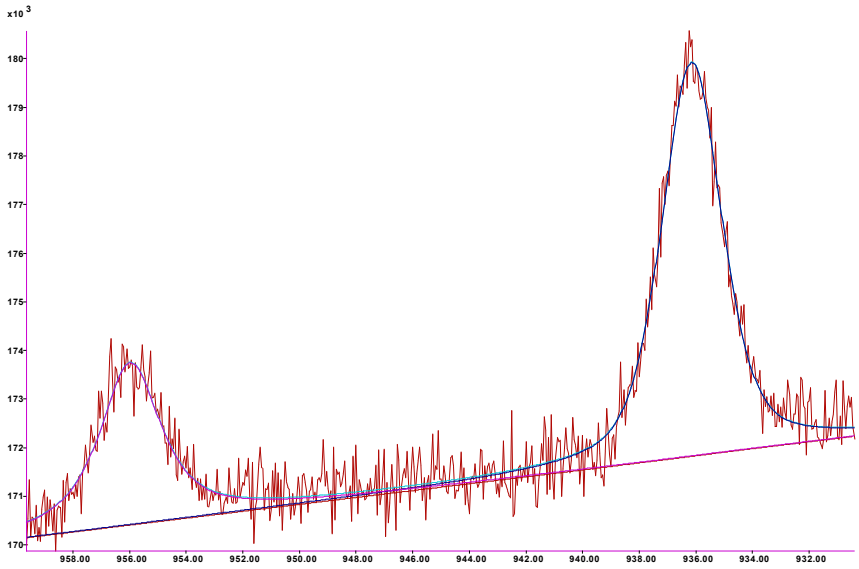

Fig. 7.31 XPS copper peaks of Cu TiO_2 550

In fact, owing to the low concentration of the metal doping ions (as the case of Fe(II/III) and Fe(III) where the signal/noise ratio was too poor) and to the typical behaviour of Cu(II) to reduce to Cu(I) under the X ray bombardment, we were only able to determine

the surface atomic concentration of the dopant species (see Table 7.3).

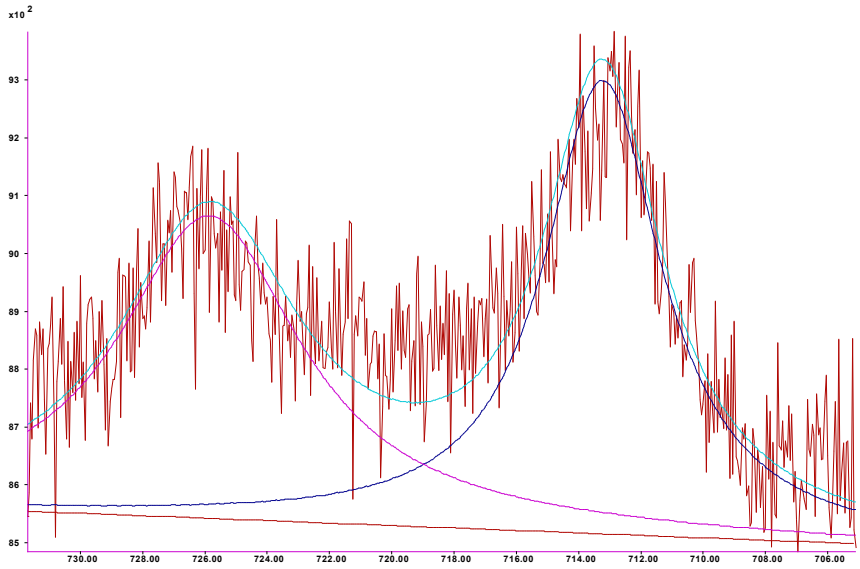

Fig. 7.32 XPS iron peaks of Fe TiO_2 550

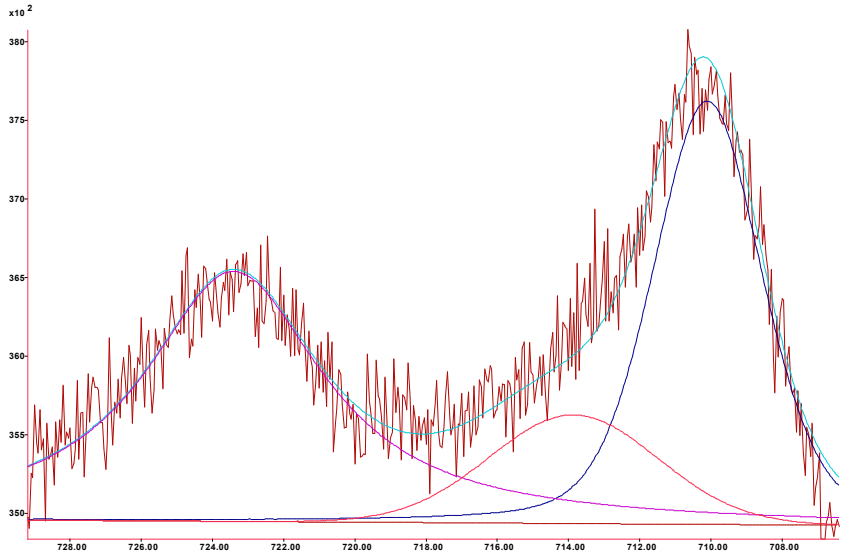

Fig. 7.33 XPS iron peaks of Fe(II/III) TiO_2 550

Table 7.4 summaries all XPS binding energies data in eV:

Table 7.4 Binding energies in eV of C, Ti, O and metal ions

	TiO_2 550	Co TiO_2 550	Fe TiO_2 550	Fe(II/III) TiO_2 550	Cu TiO_2 550
C, 1s aliphatic	285.00	285.00	285.00	285.00	285.00
C, 1s carboxylic	288.78	288.35	288.73	288.50	288.05
Ti, $2p_{3/2}$	459.00	458.65	459.05	458.60	458.73
Ti, $2p_{1/2}$	464.70	464.43	464.58	464.25	464.43
ΔTi 2p	5.70	5.78	5.53	5.65	5.70
O, 1s (lattice TiO_2)	530.38	529.95	530.25	530.08	529.88
O, 1s (OH)	531.30	531.25	531.35	531.30	531.33
O, 1s (H_2O)	532.43	532.41	532.49	532.50	532.55
M, $2p_{3/2}$	-	781.00	711.73	710.73	932.20
M, $2p_{3/2}$, sat	-	786.23	-	-	-
M, $2p_{1/2}$	-	797.05	725.03	724.03	952.03
M, $2p_{1/2}$, sat	-	802.40	-	-	-
ΔE ($2p_{1/2}$ - $2p_{3/2}$)	-	16.05	13.30	13.30	19.83

Optical properties of thin films

The onset of the material absorption corresponds to the band gap of the material, which can be express as:

$$E_g = h\,c / \lambda$$

Where:

E_g = band gap energy (eV)

h = Planck's constant (eV·s)

c = light speed (m s^{-1})

λ = wavelength (nm)

Band–gap energy of the all synthesized powders was determined spectroscopically. Theoretical treatments and details can be found in the literatures [16-18].

The values of energy band gap are usually estimated by extrapolation of the linear part of the optical density vs. wavelength, as shown in Fig. 7.34 for undoped titania annealed at 550 °C:

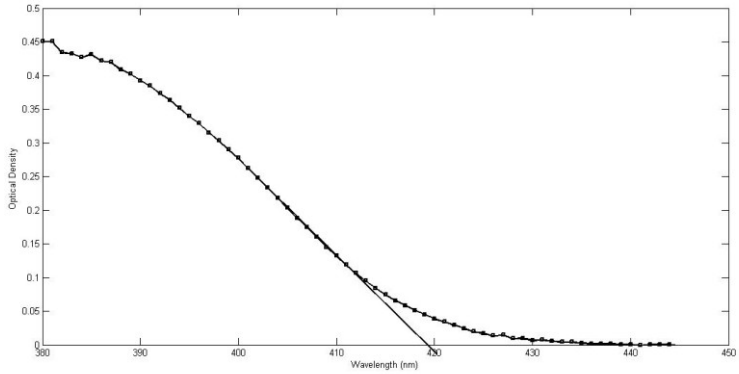

Fig. 7.34 band gap energy plot

The resulting red-shift of the onset of the absorption is related to an optical size effect of the particle size. Full band gap values and associated energies are shown in Table 7.5.

Table 7.5 Sample Band Gap energies

Material	Band Gap (nm)	Band Gap (eV)
Degussa P25	410	3.03
TiO_2 550	418	2.97
Fe TiO_2 550	590	2.10
Co TiO_2 550	575	2.16
Cu TiO_2 550	570	2.18
Fe(II/III) TiO_2 550	535	2.32
Fe TiO_2 800	775	1.60

Optical properties of TiO_2 thin films on corning glasses prepared trough sol-gel/spin coating methods were measured by Ocean Optics QE65000 UV-Vis spectrophotometer.

Optical reflectance and transmittance spectrophotometry are typically employed for measuring the optical properties of deposited thin films as well as their thicknesses. The theory of the method is well developed and excellent explanations can be found in the literature [19, 20].

Figures 7.35-7.42 show the UV-Vis-NIR reflectance and transmittance spectra before and after of thin film depositions, and their comparisons.

High transmittance and low reflectance values of the fabricated undoped and doped nano-titania thin films in all the examined range from UV (300 nm) to NIR (900 nm) reveal good transparent glasses: this indicates that TiO_2 films can be used as a window materials in those indoor applications such as gallery and museum exhibitions.

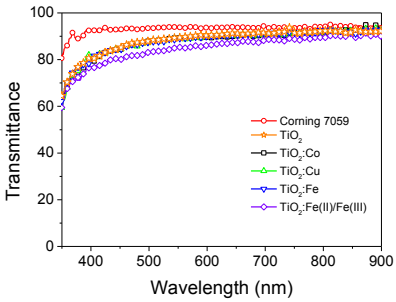

Fig. 7.35 Transmittance comparison

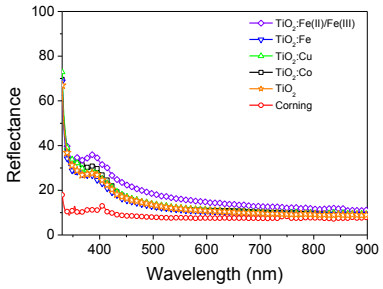

Fig. 7.36 Reflectance comparison

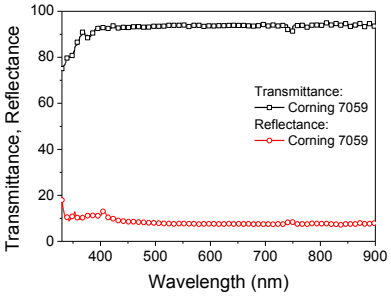

Fig. 7.37 Corning transmittance and reflectance

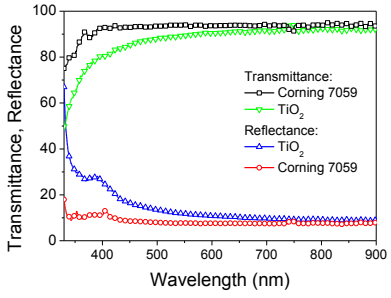

Fig. 7.38 Transmittance and reflectance comparison (undoped TiO_2)

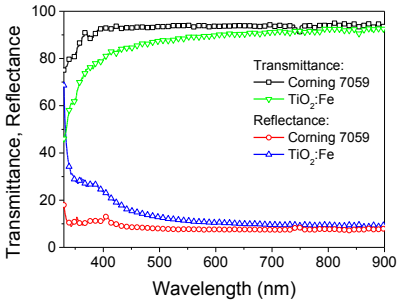

Fig. 7.39 Transmittance and reflectance comparison (Fe doped TiO_2)

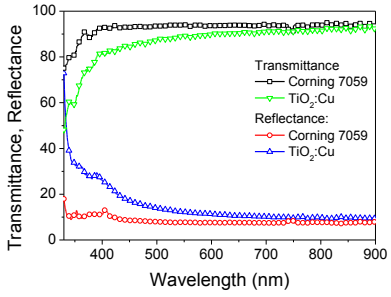

Fig. 7.40 Transmittance and reflectance comparison (Cu doped TiO_2)

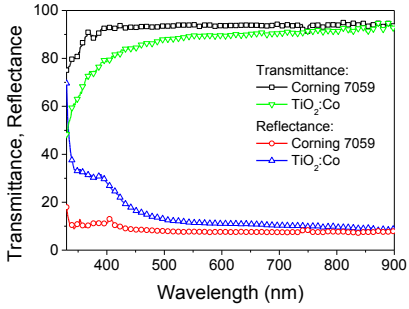

Fig. 7.41 Transmittance and reflectance comparison (Co doped TiO_2)

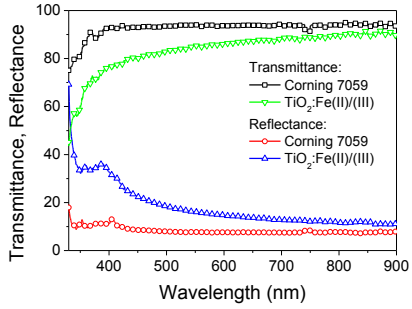

Fig. 7.42 Transmittance and reflectance comparison (Cu doped TiO_2)

From optical measurements we calculate – through the "envelop method" [21-24] – a thickness lower than 100 nm, for all our samples.

The thickness of coating films were observed and measured by FIB-SEM:

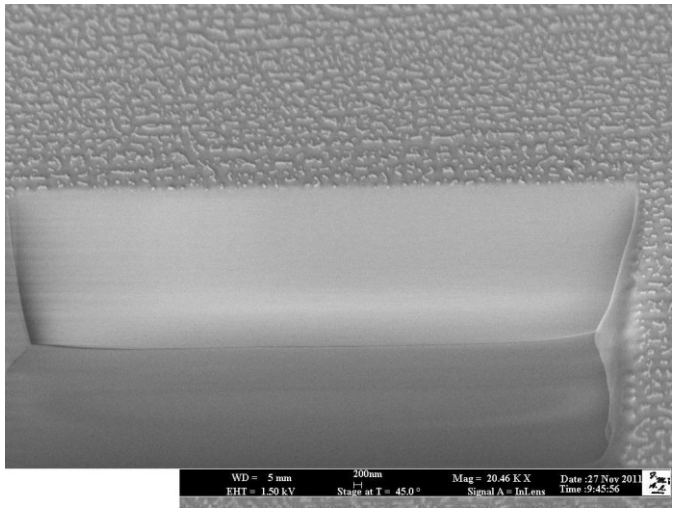

Fig. 7.43 Cut of cobalt doped thin film surface by FIB

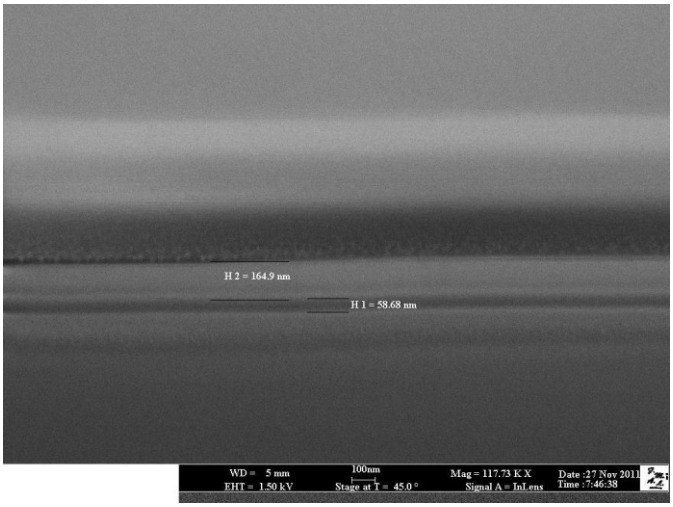

Fig. 7.44 Thin film thickness of cobalt doped sample

We found an average thickness of 60 nm, for all our samples, as shown in Fig. 7.44, which is in good agreement with those values obtained from optical profilometer measurements (Fig. 7.45).

We also found no thickness differences in all our thin films before and after three different photocatalytic experiments, which indicates that thin films possess very good adherence with the glass (Fig. 7.45), and excellent mechanical and chemical durability.

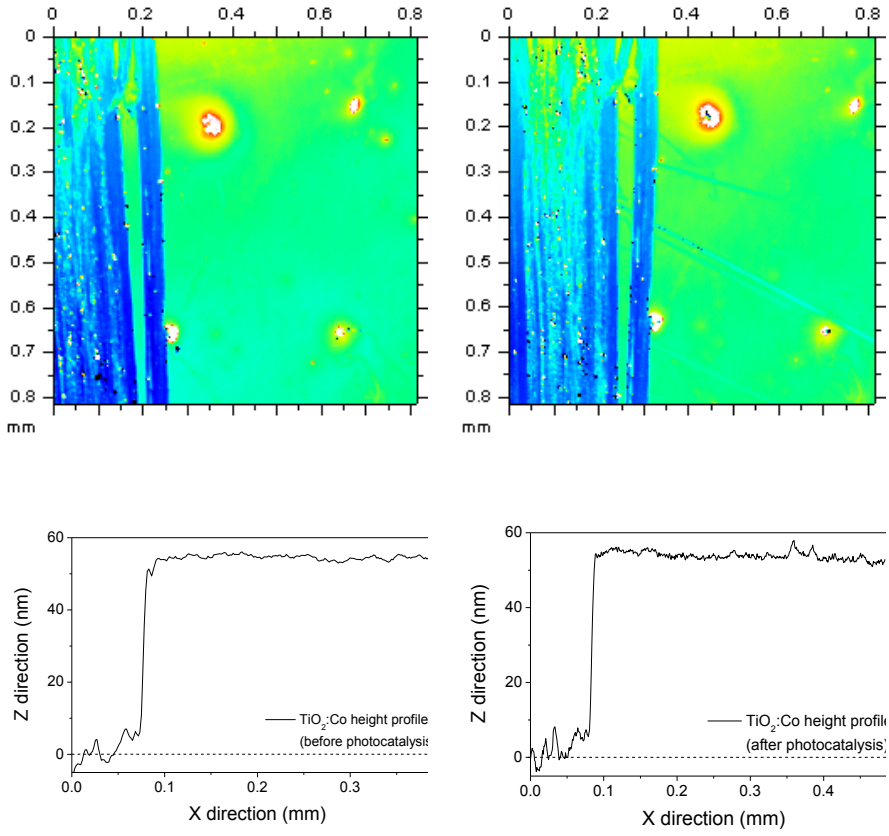

Fig. 7.45 Comparison of thin film surfaces before (left) and after (right) experiments

References

[1] A. Jiang, N. Awasthi, A. N. Kolmogorov, W. Setyawan, A. Borjesson, K. Bolton, A. R. Harutyunyan and S. Curtarolo, Phys. Rev. B, 75, 2007.

[2] J. Sun and S. L, Simon, Thermochimica Acta 463, 32, 2007.

[3] A. F. Lopeandia and J. Rodriguez-Viejo, Thermochimica Acta 461, 82, 2007.

[4] Xinyong Li, Xie Quan, Charles Kutal, Scripta Materialia, 50, 499–505, 2004.

[5] Suzuki, A.; Kotera, Y., Bulletin of the Chemical Society of Japan, 35, 1353-7, 1962.

[6] R. Arroyo, G. Cordoba, J. Padilla, V.H. Lara, Materials Letters, 54, 397– 402, 2002.

[7] Heald, Emerson F.; Weiss, Clair W., American Mineralogist 57(1-2), 10-23, 1972.

[8] W. Kallel, S. Bouattour, A.W. Kolsi, Journal of Non-Crystalline Solids, 352, 3970–3978, 2006.

[9] Wagner C.D., Riggs W.M., Davis L.E., Moulder J.F., Muilenberg G.E., "Handbook of X-Ray Photoelectron Spectroscopy", Perkin-Elmer Corporation, Physical Electronics Division, Eden Prairie, 1979.

[10] Gonbeau D., Guimon C., Pfister-Guillouzo G., Levasseur A., Meunier G., and Dormoy R., Surf. Sci., 254, 81, 1991.

[11] Frost, D. C.; McDowell, C. A.; Woolsey, I. S., Chemical Physics Letters, 17(3), 320-3, 1972.

[12] Frost, D. C.; McDowell, C. A.; Woolsey, I. S., Chemical

Physics Letters, 27(6), 1473-89, 1974.

[13] Briggs, D.; Gibson, V. A., Chemical Physics Letters, 25(4), 493-6, 1974.

[14] Mekki, A.; Holland, D.; Ziq, Kh.; McConville, C. F., Journal of Non-Crystalline Solids, 220, 267-279, 1997.

[15] Basch, H., Chemical Physics Letters, 20(3), 233-7, 1973.

[16] Takahashi, Kiyoshi; Yoshikawa, Akihiko; Sandhu, Adarsh (Eds.), Wide Bandgap Semiconductors, 2007, Springer.

[17] Tasbihi M., PhD thesis, Nova Gorica, (Slovenia), 2010.

[18] Michałów K. A., PhD thesis, Krakow, (Poland), 2009.

[19] O.S. Heavens, "Optical Properties of Thin Solid Films", Butterworths Scientific Publications, London, 1955.

[20] H.A. Macleod, Thin-Film Optical Filters, Adam Hilger Ltd, Bristol, 1986.

[21] Manifacier J. C., Gasiot J. and Fillard J. P., J. Phys. E: Sci. Instrum., 9, 1002–4, 1976.

[22] Swanepoel R, J. Phys. E: Sci. Instrum., 16, 1214–22, 1983.

[23] Essential MacLeod, Thin Film Center Inc., Tucson, AZ, USA, http://www.thinfilmcenter.com/

[24] FilmStar, FTG Software Associates, Princeton, NJ, USA, http://www.ftgsoftware.com/design.htm

Photocatalytic Activities on Gases

Introduction

The photocatalytic activity of the synthesized titania nanopowders was evaluated by the photocatalytic degradation of the common pollutants nitrogen dioxide, NO_2, under UV and visible light irradiation in artificially simulated air.

This substance was chosen for its ubiquity in any air environments, from houses to industrial sites, and its concentration is growing up due to the anthropic impact. NO_x compounds also contribute to the degradation processes of cultural heritage, especially for their acidic and oxidative properties.

A comparison between anatase nano-powders and thin films is also presented in this work.

Theoretical background

Nitrogen oxides (NO_x) refer to the group of different forms of nitrogen oxides including NO, NO_2, N_2O and are formed in many combustion processes. NO_x are produced in industrial processes and fossil fuel power generation; more significantly to urban areas they are also commonly produced in vehicle emissions, commonly in the form of NO which are then oxidized to NO_2, resulting in high concentration at the ground level. For example, studies in North America show 60 ppb NO_x at the ground level in comparison to 26 ppb in the residential outdoors [1]. With the combination of VOCs

and sunlight it is possible for NO_x to produce photochemical haze, which also forms ground level ozone, like in Los Angeles, California, due to the weather conditions. NO_x gases will also react with water to from acid rain, which can result in itself in building damage, however, it catalyses the sulphur degradation of buildings by a factor of 5. In humans, high levels of NO_x gases can cause inflammation of the airways with long exposures affecting resulting in loss of lung function causing respiratory system damage. NO_2 has been found to increase the allergen response in sensitive individuals. In the environment deposition of NO_x salts contribute to acidification of the soils and eutrophication in aqueous environments, leading to biodiversity loss. NO_x also have a negative effect on plants resulting in leaf and needle damage.

Therefore, depollution from nitrogen oxides is a goal for our Society that still needs considerable improvement, as can be frequently considered by exaggerated air pollution in specific regions with a high density of factories and/or urban population and car traffic. The "de-NO_x" process, i.e. the removal of nitrogen oxides, is possible using nanoparticle catalysis.

Experimental

Simulated air was supplied from "Air Products" and was of analytical grade, with a NO_2 initial concentration of 10 ppm:

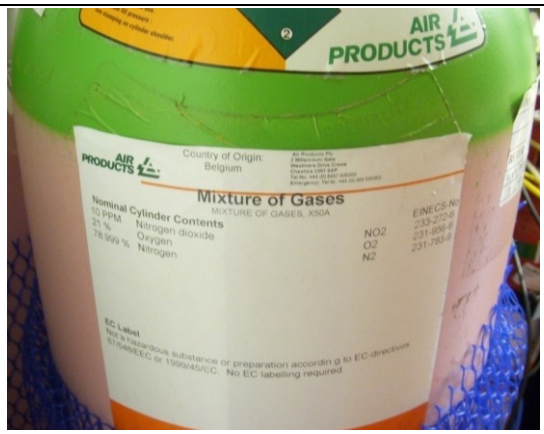

Fig. 8.1 "artificial" atmosphere

The UV-Vis light source implemented in this study was a 40 W light-emitting diode (LED), experimentally determined to emit at 390-410 nm (specifically developed by W. N. Wang, University of Bath, UK). It was located at fixed distance of 10 cm from the top of reaction vessel:

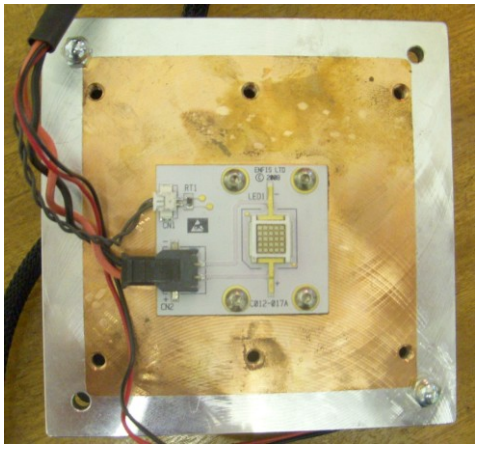

Figure 8.2 UV-Vis diode lamp

According to the band gap energies, the light wavelength was short

enough for TiO_2 activation and electron-hole pair formation.

In order to provide a moist environment in the experiments, the stainless steel reaction cell was filled in with a wet gas. The wet gas was generated by bubbling simulated air through deionised water and passed through the reaction cell at a constant rate of 100 cm^3 min^{-1} for 20 minutes, before being sealed.

Prior to UV illumination, the gas composition of the cell was monitored over a 20 minute period to check any leaks and to determine the initial baseline value.

Figure 8.3 Reaction vessel

The effects of the light and the photocatalyst on NO_2 decomposition were tested with a Residual Gas Analyzer (e-Vision mass spectrometer, MKS Instruments).

A Residual Gas Analyzer (RGA) is a small mass spectrometer, typically designed for process control and contamination monitoring in vacuum systems.

Impurities can be measured down to 10^{-14} Torr levels, possessing sub-ppm detectability in the absence of background interferences. Vacuum systems are pumped down to lower than 10^{-5} Torr. RGAs operate by creating a beam of ions from samples of the gas which is being analyzed. The resulting mixture of ions is then separated into individual species through their charge-to-mass ratios. Typical RGA has three major parts, namely an ionizer, a mass analyzer, and an ion detector.

First, the gas is moved through an ion source, which turns molecules into ions. Then, the ions are sorted out according to mass by the mass analyzer, which does so by employing electric and magnetic fields. Lastly, the detector calculates the mass-to-charge ratio. The final display of data is referred to as a mass scan or a mass spectrum.

Ionizer (Radial Open Ion Source, cylindrical and axially symmetrical ionizer)

The molecules of the gas being analyzed are turned into ions by an ionizer through electron impact ionization, i.e., an electron beam (70 eV in our instrument) is used to strike the gas atoms in order to ionize them. This ionizing electron beam is generated by a

twin hot emission tungsten filament and extracted by means of an electric field. This hot filament is easily destroyed by reactive gases like oxygen, which is why RGA's operate at pressures of less than 10^{-4} Torr.

Because open ion source RGAs can only handle a maximum pressure of 10^{-4} Torr, and base pressure tends to fall below this value, they can usually be attached directly to the vacuum chamber. They measure the gas pressures present without changing the gas composition or altering the vacuum environment.

In our equipment, the maximum operating pressure that the unit can reach is 9.7×10^{-5} Torr with a minimal detectable level of 1.9×10^{-11} Torr (a maximum detection limit of 0.26 ppm).

Mass Analyzers

Mass Analyzers used in RGAs usually employ the RF quadrupole. The RF quadrupole has four cylindrical rods that are provided with combinations of AC and DC voltages of varying frequency. Only ions that possess the right mass-to-charge ratio can reach the ion collector for a given applied frequency. Usually the mass range goes from 1 to 100 amu, with a mass stability for the unit better than ± 0.1 amu, over a period of 8 hours at stable ambient temperatures.

Ion Detector

A Faraday cup may be used as a RGA detector for detecting ions at less sensitive ranges, while ion detection at higher sensitivity

would require electron multipliers. In our instrument, a Faraday detection system is used.

Fig. 8.4 e-Vision Residual Gas Analyzer

Fig. 8.5 Vacuum pump

Simplified scheme of the experimental set up is reported in Fig. 8.6:

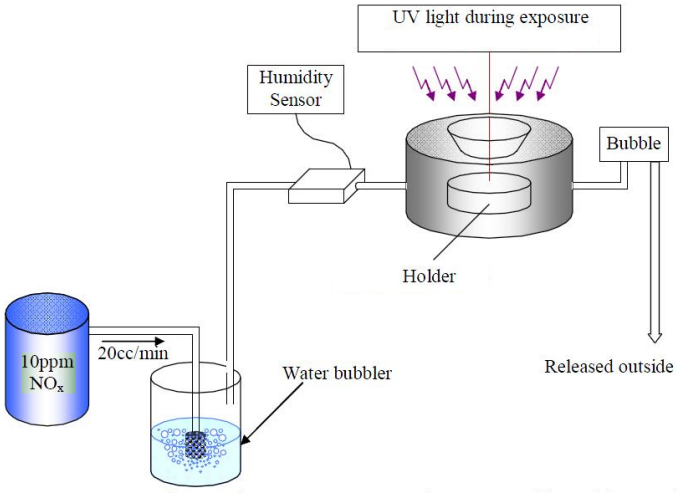

Fig. 8.6 Scheme of experimental set up

In order to identify any changes in system gas composition over the time, the following data processing was performed. The RGA data was collected continuously, scanning over a range of 0 to 50 amu with a step size of 0.3 amu. The raw signal, recording partial pressure as a function of mass, was converted to the fractional amount of mass within the system. The average gas composition determined over the initial 20 minute sampling period without UV, was subtracted as a background from the remaining data to highlight temporal changes in the gas composition. A typical example can be seen in Figure 8.7 showing the partial pressure versus the mass composition:

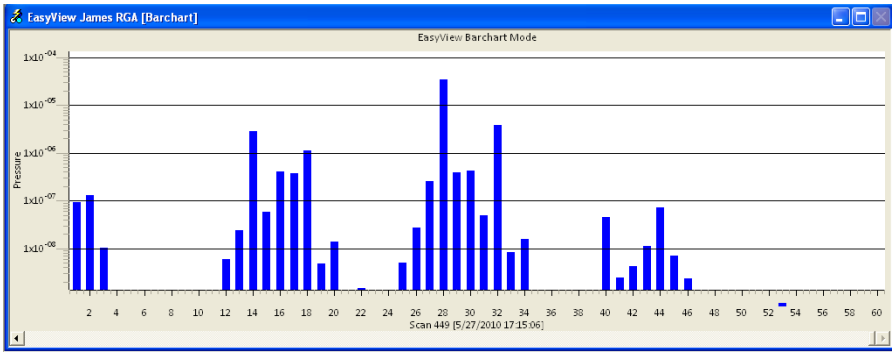

Fig. 8.7 Gas composition (partial pressure versus mass)

Mounting of powder samples was achieved by gently compacting 50 mg of titania into a glass holder (6 cm^2). Exposure was performed in the reaction chamber previously described with a 10ppm of NO_x in the air.

The experiment was conducted at room temperature (20 ± 2 ºC). The reaction vessel was made with a glass window of 3 mm

thickness, which allowed more than 90 % transmission of radiation at working wavelength that provides photons with energy higher than the band gap of the photocatalyst.

Repetition tests were made to ensure reproducibility.

Results and discussions

Due to possible future patenting, the mechanisms and kinetics are not explained in detail as would usually be required.

Photocatalytic experiments show a large reduction in the amount of NO_x within the system over the 2 hours of illumination. In all cases there was no observed change in the gas compositions over the control samples, i.e. with no illumination.

Powders doped with Co, Fe(III) and Fe(II/III) show an 80 % removal of NO_x within the 2 hours of UV illumination greater than the standard Degussa P25 TiO_2 that recorded a 30 % reduction over the same time period.

In all cases, the powders appear to be highly reactive under UV illumination, showing a large decrease in NO_2 (46), NO (40), N_2O (44) and corresponding in most cases increases in O (16), O_2 (32) and N (14), N_2 (28). On the contrary, in the cases of Fe doped systems, an increase in O_2 and little change in the N_2 levels were observed.

This is likely due to a slightly different reaction pathway. In all cases it is proposed that the breakdown is under gone via these proposed reactions [1-4]:

$$NO + HO_2^{\bullet} \rightarrow NO_2 + HO^{\bullet}$$
$$NO_2 + HO^{\bullet} \rightarrow HNO_3$$

Within the Fe doped nanoparticles it is hypothesized that the reaction stops here, with the surface stabilization of this end product. This can also be seen in the visual darkening of the samples over the illumination time period.

However in all other cases the HNO_3 is likely to decompose to N_2 and O_2 with the remaining OH being further activated and consumed in further photocatalysis. This is shown in the following decomposition reactions, as previously reported by some authors [1-4]:

$$2HNO_3 \rightarrow H_2O + N_2O_5$$
$$2N_2O_5 \rightarrow 2N_2O_4 + O_2$$

Fe(III) doped particles also showed high (60 %) removal of NO_x under daylight illumination, this was achieved by using a wide visual spectrum lamp.

The results presented here show exciting potential for the application of the doped nano-particles for the remediation of pollutant gases.

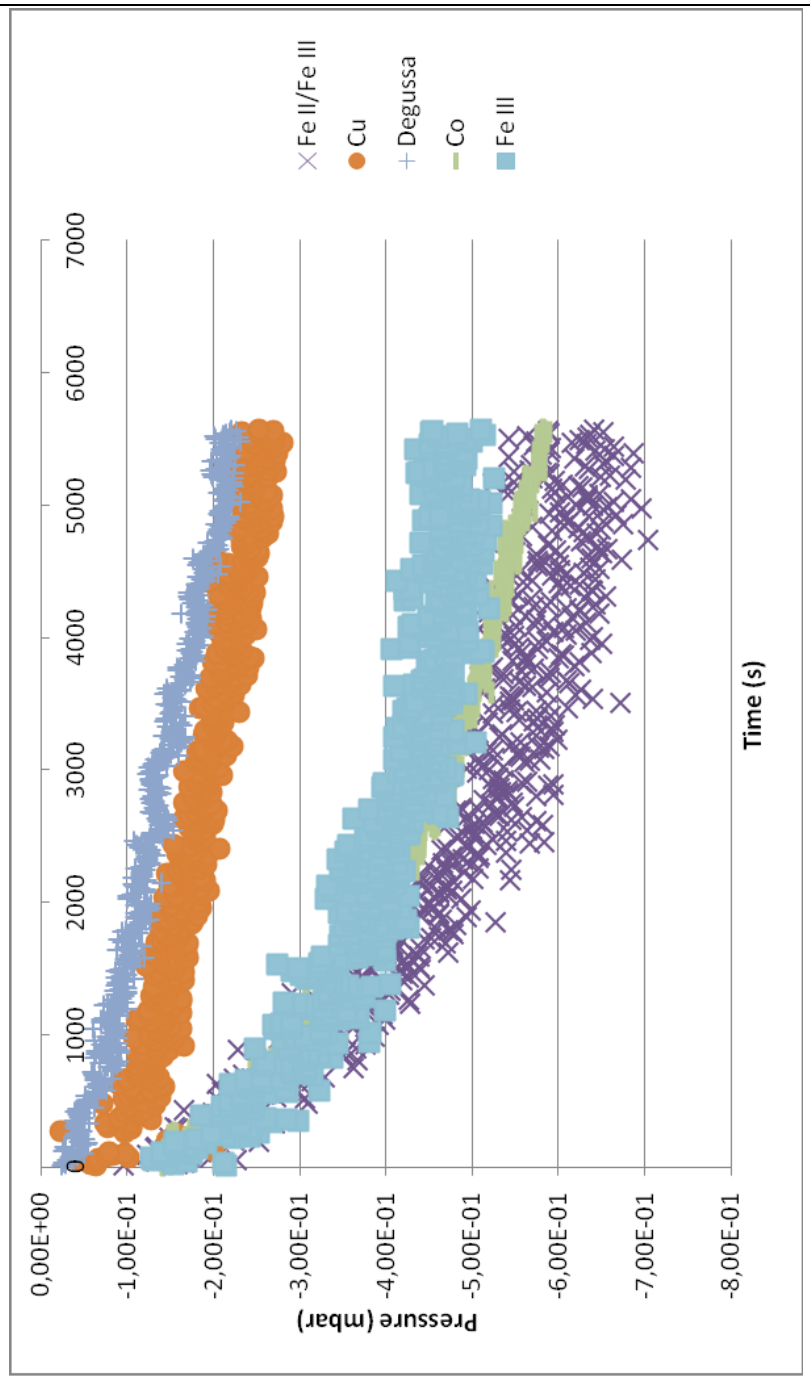

Fig. 8.8 NO_2 decomposition (mass 46)

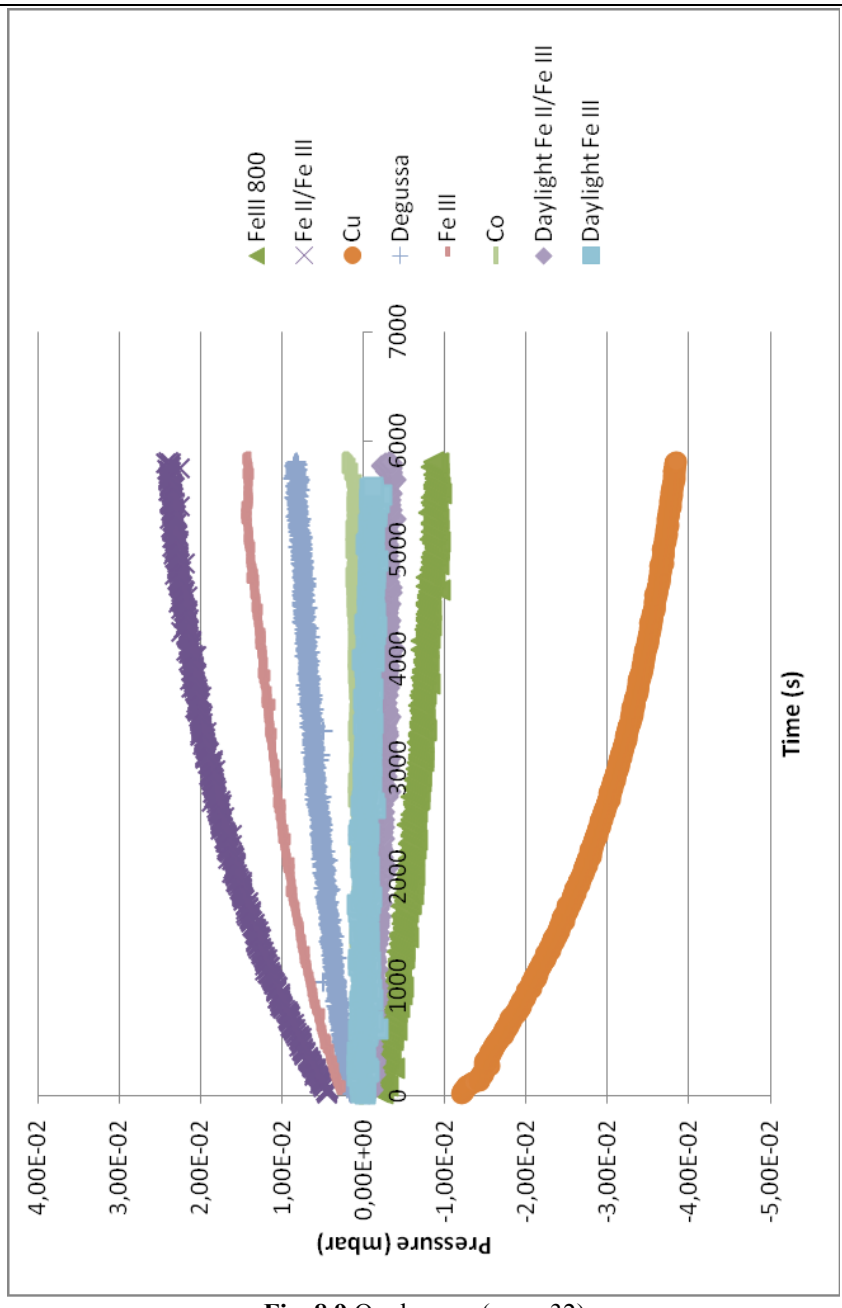

Fig. 8.9 O_2 changes (mass 32)

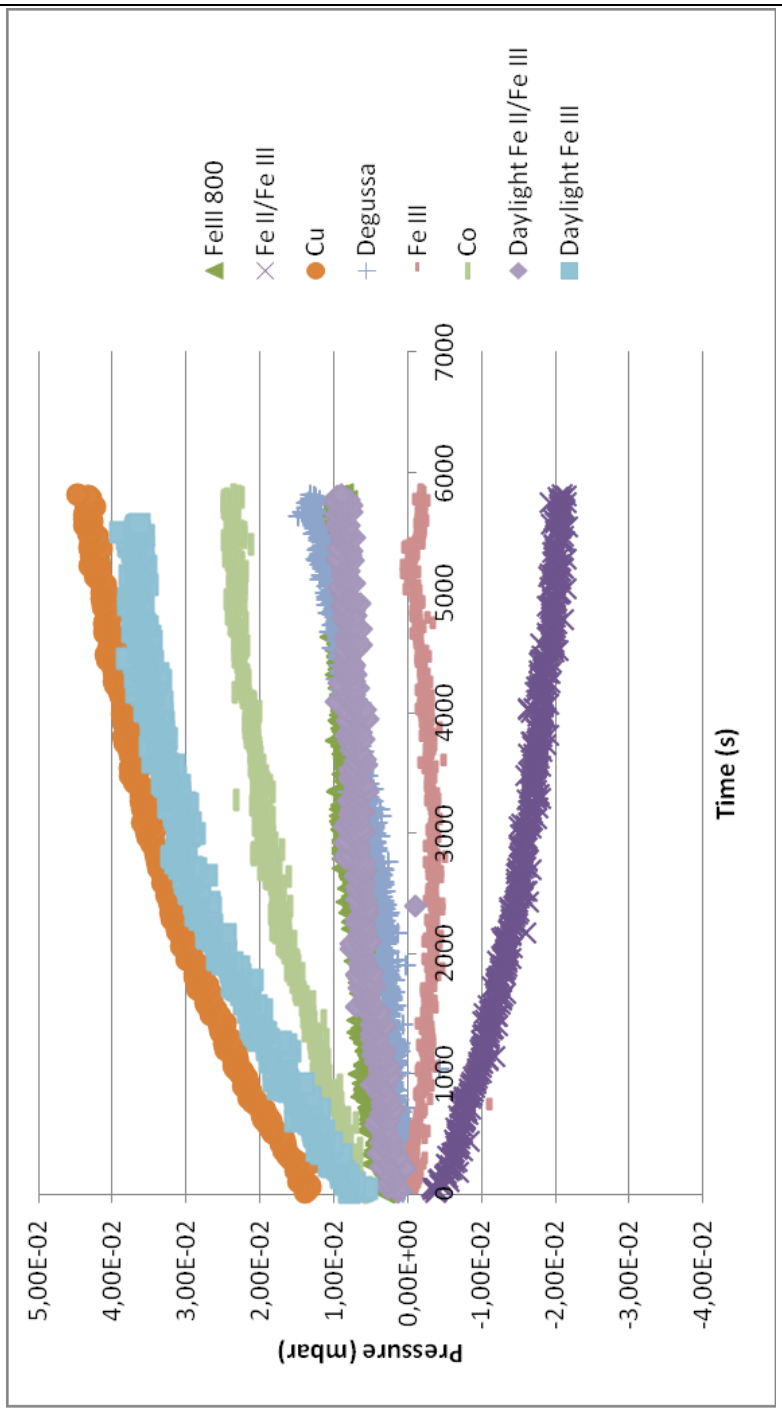

Fig. 8.10 N_2 changes (mass 28)

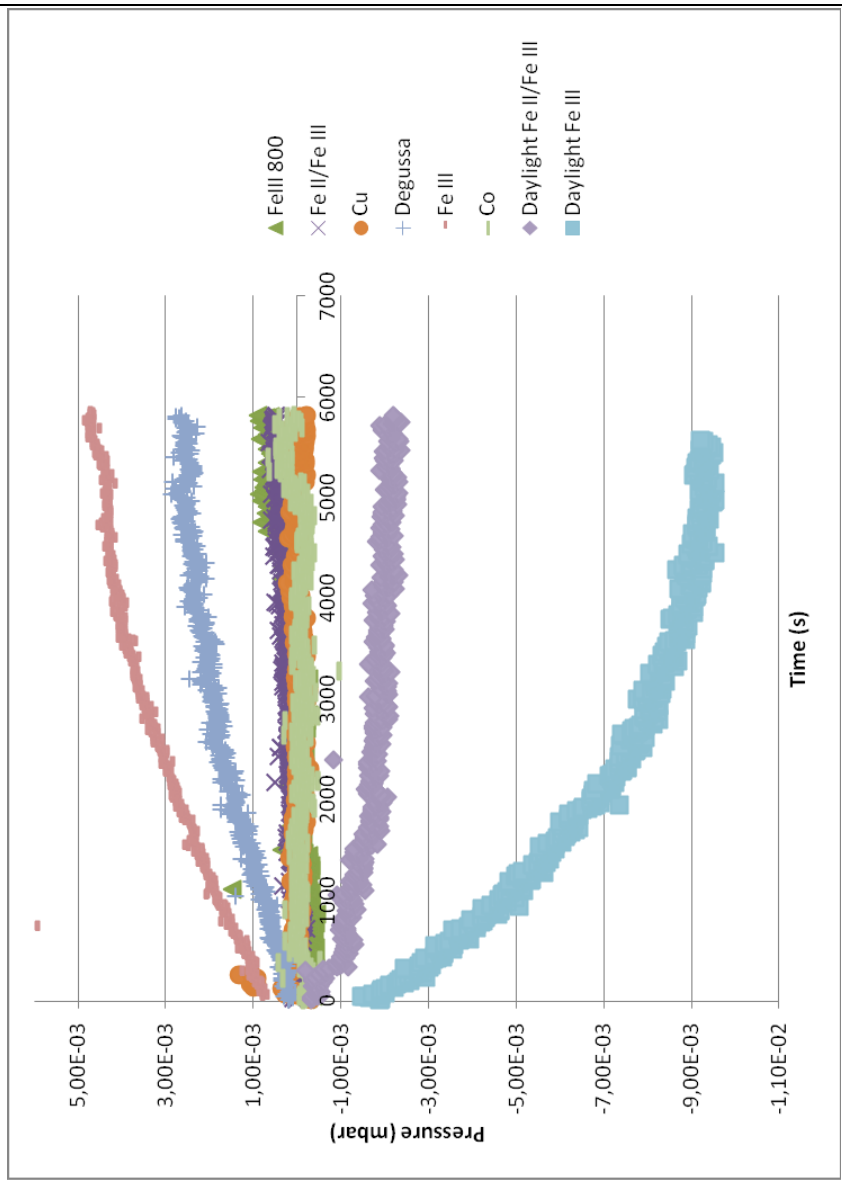

Fig. 8.11 H_2O changes (mass 18)

References

[1] Jones, C., PhD Thesis, Bristol (UK), 2009.

[2] Dalton, J. S., Env. Pollut. vol. 120, pp. 415-422, 2002.

[3] Bowering, N., Walker, G. S., Harrison, P. G., Applied Cat. B: Environmental, vol. 62, pp. 208-216, 2006.

[4] Hashimoto, K., J. Photochem. Photobio. A: vol. 136, pp. 103-109, 2000.

Photocatalytic Activities on Aqueous Systems

Introduction

The synthesized and characterized undoped and doped anatase nanoparticles were used as prepared samples in powder form as well as in thin film devices for the photocatalytic degradation of the well known dye and acid-base pH indicator Methyl Orange, MO (p-dimethylamino-azobenzenesulfonate sodium):

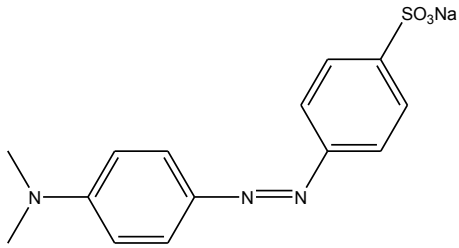

Figure 9.1 MO chemical structure

This substance was chosen for its chemical stability to resist in the environment for years [1, 2] and for the simple instrumental detectability.

The photocatalytic activity of the synthesized nano-titania was evaluated by the MO decomposition under UV and visible light irradiation in aqueous media; the progress of photodegradation was followed by UV-VIS absorption measurements.

The abatement efficiency for the organic compound was compared with that obtained with commercial TiO_2 P25 Degussa. A

comparison between anatase nano-powders and thin films is also presented in this work.

Theoretical background

Waste waters generated by the textile industries are considered as a remarkable sources of great amounts of non fixed dyes and especially of azo-dyes; around 15 % of the total world production of dyes is lost during the dyeing process and released in textile effluents [1]. The release of those colored compounds in the ecosystem is a dramatic source of aesthetic pollution and of perturbations in the aquatic life. Unfortunately for the environment, they are very stable molecules and many efforts have been carried out for their decomposition. It is well known that some azo-dyes and degradation products such as aromatic amines are highly toxic and carcinogenic: for instance, dinitroaniline orange and ortho-nitroaniline orange have been found also to be mutagenic [2].

Due to the stability of modern dyes, conventional biological and chemical treatment methods for industrial wastewater are ineffective, what often results in an intensively colored discharge from the treatment facilities; more, classical environmental cleaning up methods usually take into account the use of other chemicals: on one hand they help the environment destroying those chemicals, but on the other hand they often become new pollutants.

Among the new oxidation methods called “Advanced Oxidation Processes” (AOP), heterogeneous photocatalysis has appeared to be an emerging destructive technology, with many

advantages as described in the previous chapters.

Experimental

The UV and visible light was respectively generated by 6 commercial lamps, which were located at fixed distance of 20 cm from the top of the water solution (18 W Philips lamps, model TLD18W/965, 6500 K, with intensity of UV and Vis radiation at the level of the suspension surface of 167 W/m^2 and 183 W/m^2, respectively):

Figure 9.2 Philips D65 lamp

According to the band gap energies, the light wavelength was short enough for TiO_2 activation and electron-hole pair formation.

Lamps were properly chosen among commercial products for the similarity to solar light emission (D65) [3]:

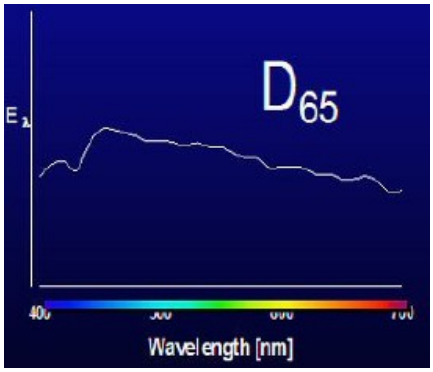

Figure 9.3 Emitting spectrum of a D65 lamp

This kind of light was also suggested to be used in museums and galleries, where no special needs are required.

Experiments were carried out in self-made apparatus, covered by aluminium foils to ensure no light lose:

Figure 9.4 Experimental apparatus

MO solutions with a concentration of 10 ppm were prepared by

dissolving the appropriate quantity of pure MO in distilled water.

200 mL of MO solution were introduced in an 250-mL cylindrical jacket Pyrex glass of 6 cm inner and 9 cm outer in diameter and 10 cm in height, opened to air. To avoid the heating of the solution, the reaction temperature was controlled by circulation of water through the jacket at a constant temperature (15 °C).

Figure 9.5 Reaction vessel with MO only

Proper amounts of undoped and doped TiO_2 nanopowders were added to MO solutions to reach a TiO_2 concentration of 50 ppm in the aqueous colloidal suspension.

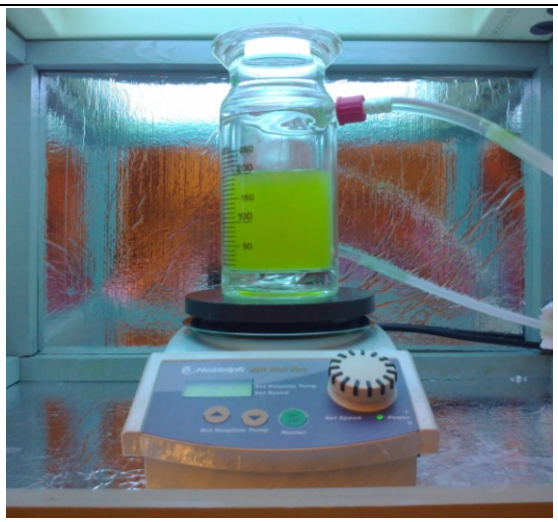

Figure 9.6 Reaction vessel with MO and photocatalyst

All experiments were done under agitation with a magnetic stirrer operating at 500 rpm in order to provide an appropriate mixing of the suspension. No external oxygen supply was used.
After 30 minutes of premixing at constant temperature, lights were switched on to initiate the reaction.

To determine the change of the MO concentrations, samples of TiO_2 aqueous suspensions were withdrawn regularly every 60 minutes for 5 hours from the reactor by using a pipette and centrifuged immediately for separation of the suspended solids:

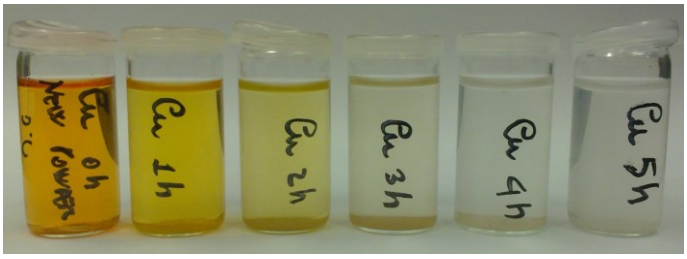

Fig. 9.7 Photodegradated samples during the time

After the centrifugation, the final clean transparent supernatant solution was poured into a quartz cuvette and analyzed by Ocean Optics UV-Vis spectrophotometer, in the range of 300-700 nm.

MO concentration was calculated by means of a calibration curve; these calibration plots based on Beer–Lambert's law were established relating the absorbance to the concentration. Each plot was determined at the maximum of absorbance: a linear relationship between the absorbance and concentration of the MO solution exists under the same condition in our experiments. Therefore, the degree of MO decolourization indicated its photodegradation. Repetition tests were made to ensure reproducibility.

Results and discussions

When UV-Vis light irradiated the suspensions containing titania photocatalysts and MO, a decolouration phenomenon occurred. This suggests that the MO decomposed in the presence of TiO_2 photocatalysts under UV-Vis irradiation; after hours, total oxidation of the dye, with a complete mineralization of carbon into CO_2 was achieved (no absorbance was found in those samples):

$$2C_{14}H_{14}N_3O_3S^- + 43O_2 \rightarrow 28CO_2 + 10H_2O + 6NO_3^- + 2SO_4^{2-} + 8H^+$$

To exclude the possibility that the decolouration was caused by the UV-Vis light itself, some experiments were carried out where only MO solution in the absence of TiO_2 was irradiated by light.
The result indicated that the differences in the UV-Vis spectra before and after irradiation for five hours were negligible, indicating that UV-Vis light does not decompose MO in the absence of TiO_2 nanopowders.

After investigating also that no detectable MO degradation occurred with titania and without UV-Vis irradiation, the photocatalytic disappearance of MO dye was performed, according to the procedure indicated in the experimental section.
The UV-Vis absorbance spectra of MO (10 ppm) before and after irradiation with iron doped TiO_2 (50 ppm), are shown in Fig. 9.8:

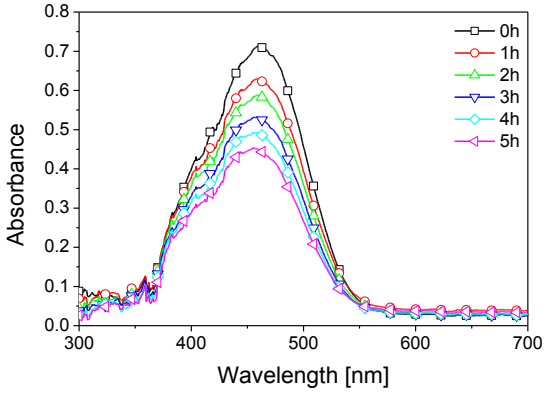

Fig. 9.8 Absorbance spectra of iron doped TiO_2

The degradation curves of the MO by undoped and doped TiO_2 are well fit by a mono-exponential curve, suggesting that a pseudo-first-order reaction model can be taken into account for

describing the kinetic behaviour, as shown in Fig. 9.9 for iron doped sample:

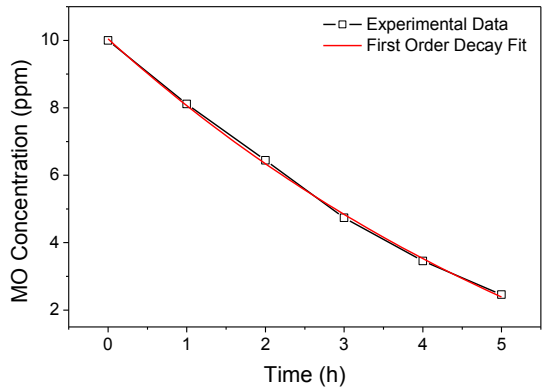

Fig. 9.9 MO decomposition curve (iron doped TiO_2)

The coefficient of determination R^2 is a measure of how close and well the regression curve represents the experimental data; for our experiments fit exponential curves were calculated and coefficients of determination reported in Table 9.1:

Table 9.1 Correlation constants for the fit exponential curves (powders)

Sample	**R^2**
Degussa	0.9989
Iron(II/III)	0.9986
Cobalt	0.9947
Copper	0.9971
Iron	0.9991

Figure 9.10 shows also that reactions followed an apparent first-order decay, verified by the linear relation of ln C/C_0 versus time in hours (iron doped sample):

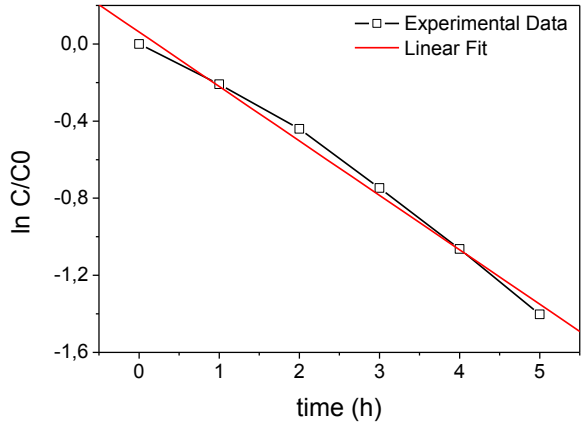

Fig. 9.10 MO decomposition curve in logarithmic scale

We also studied the degree of dispersion in water for the prepared nanoparticles. Titania annealed at 300 °C and 550 °C show different behaviour. After a care examinations of all parameters, we realized that the dispersion of doped samples strongly depends on the annealing temperature:

Fig. 9.11 Sample comparison of water dispersion (annealed at 550 and 300 °C)

XRD patterns of samples annealed at 300 °C show anatase phase only; Fig. 9.12 displays the XRD pattern of undoped sample:

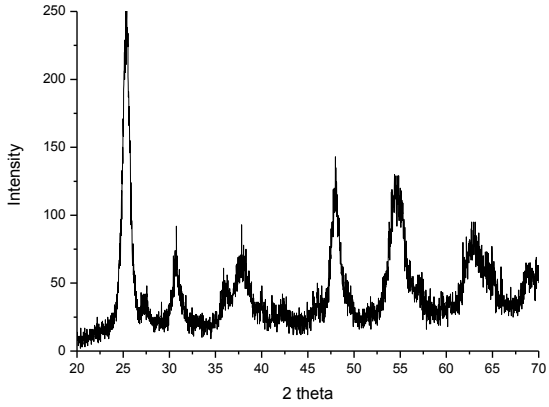

Figure 9.12 XRD pattern of TiO_2 300

Compared to Fig. 7.7 (TiO_2 550), samples annealed at 300 °C show XRD broader peaks: the broader the peak the smaller the nanoparticle. Calculations by Scherrer's formula give nanoparticle sizes of 10-15 nm for all the samples, which is also confirmed by SEM images (Fig. 9.13):

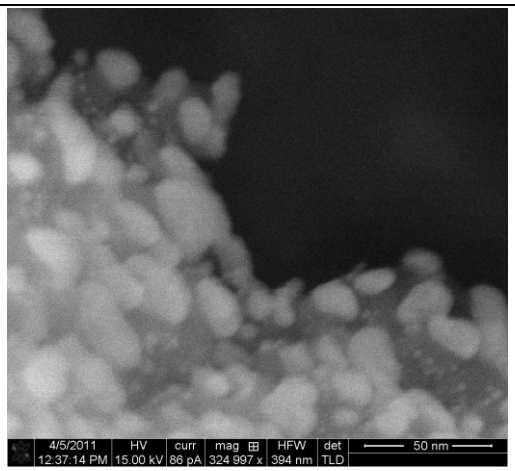

Fig. 9.13 TiO_2 300 SEM image

All the samples annealed at 550 °C show the same characteristics of those annealed at 300 °C, but they possess a lower degree of dispersion in water. This, in turn, strongly appears to influence the photoactivity of the nanoparticles.

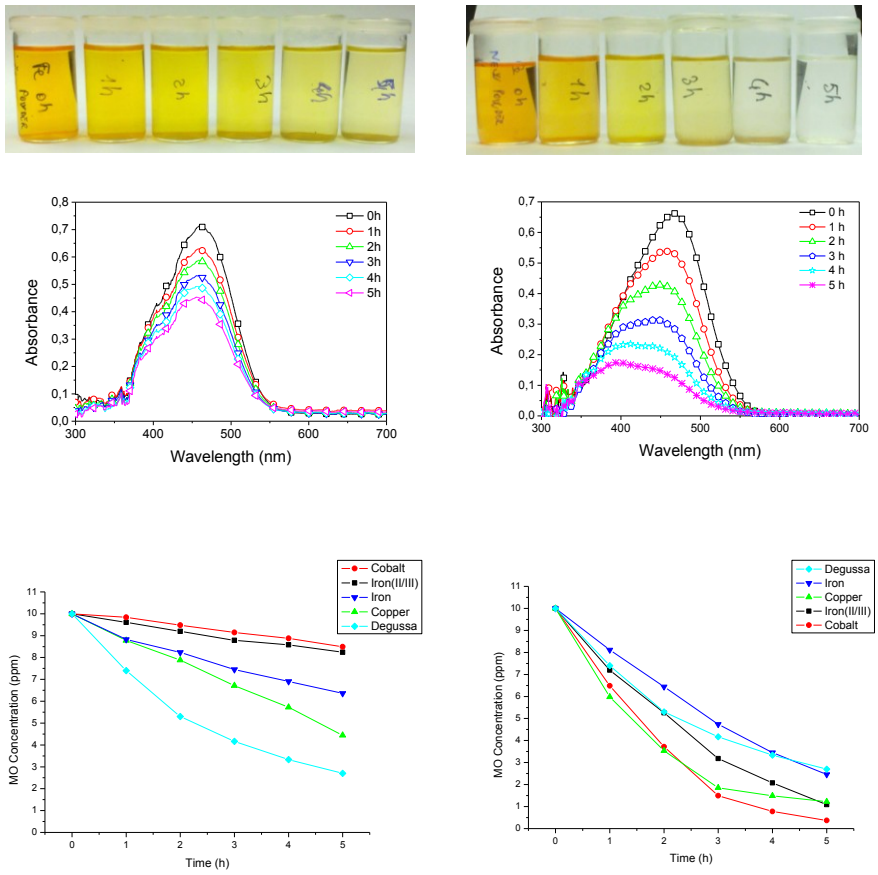

Fig. 9.14 Effect of the annealing temperature on the dispersion degree. On the left: Comparison between undoped and doped nanoparticles annealed at 550 °C. On the right comparison between undoped and doped nanoparticles annealed at 300 °C

The presence of OH groups at the external surface of nanoparticles, the smaller sizes, and a lower nano-powder aggregation and agglomeration, typical of samples annealed at lower temperatures give better results.

Similar experiments were carried out in the case of undoped and doped titania thin films. As shown in Fig. 9.15, a 3 x 1 cm^2 TiO_2 thin film was put in the same reactor in the same conditions:

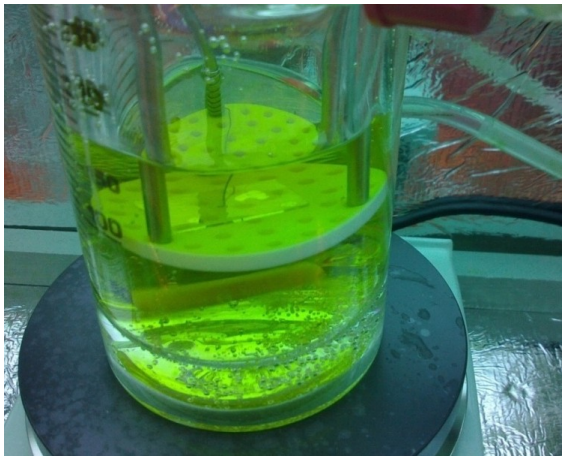

Fig. 9.15 Thin film in the reaction vessel

Fig. 9.16 shows absorbance change in the time for Fe doped sample:

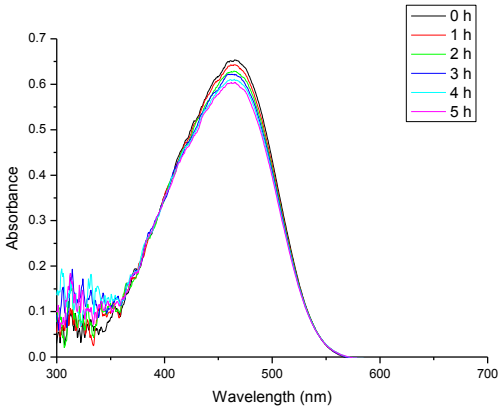

Fig. 9.16 Absorbance spectra of iron doped TiO_2 thin film

MO photodecomposition with thin film is much lower compared to

the one obtained with the nanopowder. This is due to the small surface involved in the reaction.

Table 9.2 reports coefficient of determination R^2 for thin film experiments, while Fig. 9.17 shows a total comparison of undoped and doped nanotitania thin films:

Table 9.2 Correlation constants for the fit exponential curves (thin films)

Sample	**R^2**
Degussa	0.9981
Iron(II/III)	0.9993
Cobalt	0.9713
Copper	0.9941
Iron	0.9976

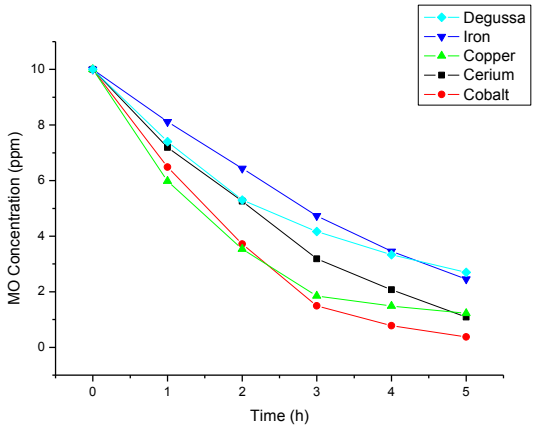

Fig. 9.17 Decomposition curves of thin films

References

[1] H. Zollinger (Ed.), "Color Chemistry. Synthesis, Properties and Applications of Organic Dyes and Pigments", 2nd Revised Edition, VCH, 1991.

[2] M.A. Brown, S.C. De Vito, Crit. Rev. Environ. Sci. Technol., vol. 23, 1993, pp. 249–324.

[3] http://en.wikipedia.org/wiki/Illuminant_D65

Conclusions

The main purpose of this study was to synthesise and characterize nanoscale TiO_2-based photocatalysts with enhanced photocatalytic activity in ultraviolet and visible light. The contribution of the nanocrystalline catalysts to spectroscopic and structural characterizations is reported, and the efforts made to fabricate, characterize and manipulate these inorganic structures at the nanoscale are described, especially environmental applications devoted to the protection of cultural heritage.

Titanium dioxide anatase nanocrystals with photocatalytic activity were prepared from titanium tetraisopropoxide hydrolysis by using the low–temperature sol–gel method, and applied as a thin film coating by the spin-coating synthetic procedure on glass substrates, to simulate the photocatalyst effects on showcase windows. TiO_2 thin films produced by the sol-gel method present properties such as:

- high transparency in the visible region of the spectrum;
- excellent mechanical and chemical durability;
- uniformity in thickness (thin films of about 60 nm were obtained by coating twice).

TiO_2 thin films are highly transparent and have low reflectance in the visible range: our thin films can be used to coat the protective glass used in museums, galleries, exhibitions, etc.

Moreover, the sol-gel method and spin coating deposition are economical and industrial applications can be produced easily. Furthermore, to increase the photocatalytic activity of TiO_2 powder, the nanoparticles were doped using Fe^{2+}, Fe^{3+}, Co^{2+}, Cu^{2+} at 1 % atomic concentration.

All the nanoparticles obtained were spherically shaped, non-aggregated and highly crystalline; the mean anatase particle size was between 10-15 nm when annealed at the lower temperature (300 °C) and around 25-30 nm when calcinated at 550 °C. The doped TiO_2 samples absorb radiations in the UV and in the VIS region of the solar spectrum.

Techniques such as thermal analyses, XRD, SEM, DLS, XPS, UV-Vis and Raman spectroscopy were used to characterize the materials from a morphological, optical and structural point of view. Degussa TiO_2 P25 nanopowder was used as a reference.

This study demonstrates that efficient photocatalysis can be produced with nanosized oxide catalysts. TiO_2 nanoparticles were tested in a controlled atmosphere and aqueous suspension.

We compared the photocatalytic efficiency of undoped and doped TiO_2 immobilized onto substrates with catalysts in suspended form. NO_x were totally degraded in the two hour experiments. Thus our doped photocatalysts proved to be a valuable treatment for purifying air.

Photocatalytic activity evaluation was based on methyl orange (MO) degradation in UV-A and Vis light. After 5 hours of adsorption and UV light, the concentration of organic pollutant in the wastewaters decreased by ~ 100 %. Samples annealed at lower

temperatures (300 °C) show better photoactivity compared to those calcinated at 550 °C. There was higher photoactivity of doped nanoparticles compared to the Degussa reference, and a pseudo first-order kinetics was found. Moreover, photocatalysis based on anatase nanoparticles also proves to be a valuable treatment for purifying polluted water. Rutile samples did not show any photocatalytic activities, either in gas or aqueous phases.

Photocatalysis is a very promising method for dealing with most problems connected with increasing environmental pollution, and titanium dioxide, in its anatase crystallographic phase, which is one of the most researched photocatalytic materials is perfectly compatible with everyday human activities.